DIRECT CONVERSION OF METHANE TO METHANOL OVER IRON-EXCHANGED ZEOLITES

A THESIS SUBMITTED TO
THE GRADUATE SCHOOL OF NATURAL AND APPLIED SCIENCES
OF
MIDDLE EAST TECHNICAL UNIVERSITY

BY

İKLİM GÖKÇE

IN PARTIAL FULFILLMENT OF THE REQUIREMENTS
FOR
THE DEGREE OF MASTER OF SCIENCE
IN
CHEMICAL ENGINEERING

AUGUST 2022

Approval of the thesis:

DIRECT CONVERSION OF METHANE TO METHANOL OVER IRON-EXCHANGED ZEOLITES

submitted by **İKLİM GÖKÇE** in partial fulfillment of the requirements for the degree of **Master of Science in Chemical Engineering, Middle East Technical University** by,

Prof. Dr. Halil Kalıpçılar
Dean, Graduate School of **Natural and Applied Sciences**

Prof. Dr. Pınar Çalık
Head of the Department, **Chemical Engineering**

Assoc. Prof. Dr. Bahar İpek Torun
Supervisor, **Chemical Engineering, METU**

Examining Committee Members:

Prof. Dr. Deniz Üner
Chemical Engineering, METU

Assoc. Prof. Dr. Bahar İpek Torun
Chemical Engineering, METU

Prof. Dr. Burcu Akata Kurç
Micro and Nanotechnology, METU

Assist. Prof. Dr. Gökhan Çelik
Chemical Engineering, METU

Assist. Prof. Dr. Murat Oluş Özbek
Chemical Engineering, GTU

Date: 08.08.2022

I hereby declare that all information in this document has been obtained and presented in accordance with academic rules and ethical conduct. I also declare that, as required by these rules and conduct, I have fully cited and referenced all material and results that are not original to this work.

Name Last name : İklim Gökçe

Signature :

ABSTRACT

DIRECT CONVERSION OF METHANE TO METHANOL OVER IRON-EXCHANGED ZEOLITES

Gökçe, İklim
Master of Science, Chemical Engineering
Supervisor : Assoc. Prof. Dr. Bahar İpek Torun

August 2022, 162 pages

Methane is the primary component of natural gas and the abundance of methane is increased with increased shale gas production. The extracted methane should be converted to more valuable, liquid products on site such as methanol, which is highly versatile and an important feedstock for many chemicals. Unlike the industrial conversion of methane to methanol, which is via an indirect and highly energy intensive route, alternative routes of direct conversion of methane to methanol at milder conditions are searched for. Iron loaded zeolites are promising catalysts for catalytic conversion of methane to methanol under milder conditions and should further be investigated.

In this study, iron-exchanged zeolites having different frameworks such as MOR, SSZ-13 and SSZ-39 are investigated for catalytic conversion of methane to methanol. MOR, which is a large pore zeolite showed the highest methanol formation rate and selectivity. On the other hand, small pore zeolites (SSZ-13 and SSZ-39) deactivated quickly due to coke formation and even though mesopore addition improved activity for SSZ-39, Fe-MesoMOR showed better activity than

Fe-MesoSSZ-39. The effect of iron content on methanol selectivity is optimized over Fe-MOR.

Mesopore addition to MOR significantly promoted the methanol selectivity, especially at lower water vapor in feed, and enhanced catalyst lifetime due to shortened diffusion pathway. At the optimized reaction conditions which are 300 °C, 30% CH_4, 10% N_2O and 24% H_2O, Fe-MesoMOR produced 330 μmol/g/h methanol with 47% selectivity. Increasing the water vapor in feed increased methanol selectivity by suppressing secondary reactions and by promoting methanol desorption from the surface and stabilized the methanol production rate.

Fe-MesoMOR is compared at the optimized conditions in this study with the best performed Fe-FER and mostly studied Fe-ZSM-5 in literature. Fe-FER exhibited a better performance than Fe-MesoMOR in terms of methanol production rate and selectivity at all temperatures, 300, 320 and 340 °C. The highest methanol formation rate of 958 μmol/g/h with 41% methanol selectivity is achieved over Fe-MesoMOR at 340 °C. The characterization of active sites is carried out using DR UV–Vis spectra of N_2O and CH_4 treated Fe-zeolites at 300 °C.

Keywords: Methane to Methanol, Catalysis, Mesoporous Zeolites, Fe-MesoMOR

ÖZ

METANIN DEMİR YÜKLENMİŞ ZEOLİTLER ÜZERİNDE DOĞRUDAN METANOLE DÖNÜŞTÜRÜLMESİ

Gökçe, İklim
Yüksek Lisans, Kimya Mühendisliği
Tez Yöneticisi: Assoc. Prof. Dr. Bahar İpek Torun

Ağustos 2022, 162 sayfa

Metan, doğalgazın birincil bileşenidir ve artan kaya gazı üretime ile metan bolluğu artmaktadır. Çıkarılan metan sahada, çok kullanışlı ve birçok kimyasal için önemli bir hammadde olan metanol gibi daha değerli, sıvı ürünlere dönüştürülmelidir. Metanın metanole dolaylı ve yüksek enerji gerektiren endüstriyel dönüşümünden farklı olarak, daha ılıman koşullarda metanın doğrudan metanole dönüştürülmesi için alternatif yollar aranır. Demir yüklü zeolitler, metanın metanole daha hafif koşullarda katalitik dönüşümü için umut verici katalizörlerdir ve daha fazla araştırılmalıdır.

Bu çalışmada, MOR, SSZ-13 ve SSZ-39 gibi farklı yapılara sahip demir yüklü zeolitlerin metanın metanole katalitik dönüşümü araştırılmış ve büyük gözenekli bir zeolit olan MOR, en yüksek metanol oluşumu hızı ve seçiciliği göstermiştir. Öte yandan, küçük gözenekli zeolitler (SSZ-13 ve SSZ-39), kok oluşumu nedeniyle hızlı bir şekilde deaktive olmuş ve mezopor ilavesi SSZ-39 için aktiviteyi iyileştirmiş olsa da, Fe-MesoMOR, Fe-MesoSSZ-39'dan daha iyi aktivite göstermiştir. Ayrıca, Fe-MOR üzerinde demir miktarının metanol seçiciliği araştırılmıştır.

MOR yapısına sahip zeolite mezogözenek ilavesi özellikle düşük su buharında, kısaltılmış difüzyon yolundan dolayı metanol seçiciliğini önemli ölçüde artırdı ve katalizör ömrünü uzattı. 300 °C ve %30 CH_4, %10 N_2O and %24 H_2O olarak optimize edilmiş reaksiyon koşullarında Fe-MesoMOR, %47 seçicilik ile 330 μmol/g/h metanol üretti. Beslenen su buharının arttırılması, ikincil reaksiyonları baskılayarak ve yüzeyden metanol desorpsiyonunu teşvik ederek metanol seçiciliğini arttırdı ve metanol üretimini stabilize etti.

Bu çalışmada optimize edilmiş koşullarda Fe-MesoMOR, literatürde en iyi performans gösteren Fe-FER ve en çok çalışılan Fe-ZSM-5 ile karşılaştırılmıştır. Fe-FER, 300, 320 ve 340 °C'deki bütün sıcaklıklarda metanol üretim hızı ve seçicilik açısından Fe-MesoMOR'a göre daha iyi performans göstermiştir. Fe-MesoMOR üzerinden elde edilen en yüksek metanol oluşum hızı, 958 μmol/g/h metanol ve %41 seçicilik ile 340 °C'dedir. Aktif sitelerin karakterizasyonu, 300 °C'de N_2O ve CH_4 ile işlem yapılmış Fe-zeolitlerin UV–Görünür Bölge spektrumları kullanılarak gerçekleştirilmiştir.

Anahtar Kelimeler: Metandan Metanol Çevrimi, Kataliz, Mezogözenekli zeolit, Fe-MesoMOR

To My Family

ACKNOWLEDGMENTS

I would like to start by expressing my deepest and most sincere gratitude to my supervisor Assoc. Prof. Dr. Bahar İpek Torun for her support, guidance, advice, and encouragements throughout this research. Her valuable criticism helped me improve myself and our work.

I would like to thank the rest of the thesis committee: Prof. Dr. Deniz Üner, Prof. Dr. Burcu Akata Kurç, Assist. Prof. Dr. Gökhan Çelik and Assist. Prof. Dr. Murat Oluş Özbek for their time and valuable comments.

I would also like to express my gratitude for my mother Güler Çetin, father Sermet Gökçe and my grandparents Fatma Çetin and Salih Çetin for their love, support, and encouragements. I feel very lucky to have a loving and supporting family who believes in me.

I would like to thank my dearest friend İrem Sağlam who has been only one phone call away from me for years. Her friendship and encouragements were even more significant during this time. Also, I would like to acknowledge my friends, Dilara Aysungur, Buğra Çakan, Barış Can, Ceyda Kalıpçıoğlu and Beste Tekçe for their love and support even we were in different cities.

I am deeply grateful for my friends Nurkan Sarohan and Sezer Osmanağa whom I shared this journey with. Their encouragement and support as well as our discussions helped me improve myself and our work. But we became more than laboratory members and I am thankful for our friendship. I would also like to thank Sılay Önder for her companionship and endless support. Lastly, I would like to thank Melis Özdemir for advising me to work with my supervisor Assoc. Prof. Dr. Bahar İpek Torun.

I would like to thank to Scientific and Technological Research Council of Turkey (TUBITAK) for financial support under grant number 118M656.

TABLE OF CONTENTS

CHAPTERS

LIST OF TABLES

TABLES

LIST OF FIGURES

FIGURES

LIST OF ABBREVIATIONS

ABBREVIATIONS	
MTM	Methane to Methanol
MTO	Methanol to Olefins
MMO	Methane Monooxygenase Enzyme
SDA	Structure Directing Agent
CTABr	Cetyltrimethylammonium Bromide
ACN	Acetonitrile Solution
IE	Ion-exchange
SSIE	Solid-state ion-exchange
WI	Wet impregnation
XRD	X-Ray Diffraction
SEM	Scanning Electron Microscopy
BJH	Barret-Joyner-Halenda Adsorption Model
EDX	Energy Dispersive X-Ray Spectroscopy
ICP-OES	Inductively Coupled Plasma-Optical Emission Spectroscopy
UV–Vis	Ultraviolet-Visible Spectroscopy
MAS NMR	Magic Angle Spinning-Nucleic Magnetic Resonance
DFT	Density Functional Theory
DME	Dimethyl ether

LIST OF SYMBOLS

SYMBOLS

λ	Wavelength (Å)
T	Temperature, °C
r	Rate, µmol/g/h
x	Conversion, %
S	Selectivity, %
TOF	Turnover Frequency, µmol CH_3OH/mmol Fe/h

CHAPTER 1

INTRODUCTION

Due to limited reserves of petroleum, new energy sources are searched for and shale and tight gases are discovered in large reservoirs around the world. However, due to increased shale gas extraction, inefficient utilization of methane results in flaring of methane. Therefore, extracted methane should be converted to more valuable products on site for easier transportation. Methanol is one of the possible compounds for methane valorization.

1.1 Methane

The increase in crude oil prices caused searching for new raw materials such as natural gas, which consists of mostly methane [1]. Methane is generally used for industrial purposes and home heating as well as electricity generation [2]. Methane is the simplest alkane with highly stable C-H bonds. It is highly abundant in nature and with the increased sources of shale or tight gases, it has become more abundant. Shale and tight gases are considered as the primary contributors to natural gas production in the United States through 2050 and the natural gas production sources projected by U.S. Energy Information Administration is given in Figure 1.1. Shale or tight gases are the natural gas trapped in between shales and rocks. Hydraulic fracturing is required for the extraction of these gases, in which wells are drilled, water based fluids are injected at high pressures to crack the shales hydraulically and extracted gas is transported to process units [3]. However, during all the processes of drilling, extraction, transportation and storage of natural or shale gas, methane is fugitively emitted to the atmosphere gas [4]. Moreover, if extracted gas is not utilized or captured for sale on site, the excess methane is flared, which causes release of greenhouse gases such as CO_2 [5]. Methane is also the second most dominant greenhouse gas after CO_2 and foundless in the atmosphere than CO_2, but the 100 year global warming potential of methane is almost 28 times higher than CO_2 [6], [7]. The higher global warming potential indicates that methane absorbs emitted thermal infrared radiation stronger than carbon dioxide [4]. Thus, extracted methane from shale formations should be converted to more valuable products in small scale, preferrable liquid products for easier transportation.

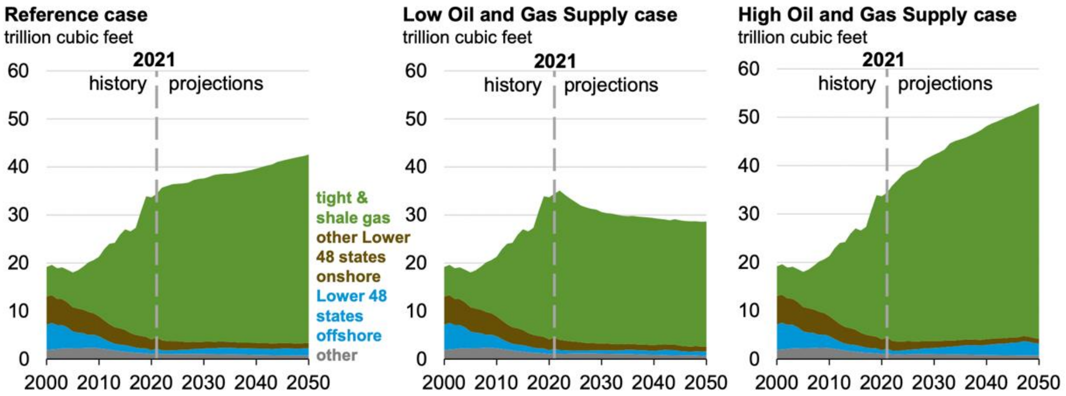

Reference case

Low Oil and Gas Supply case

High Oil and Gas Supply case

Figure 1.1 Sources of dry natural gas production history and projections through 2050 [8]

The possible routes for methane utilization are given in Figure 1.2. Methane can be directly converted to ethane and ethylene by oxidative coupling, aromatic hydrocarbons could be produced via non-oxidative coupling of methane or methanol could be obtained by partial oxidation of methane. On the other hand, when snygas is formed from methane reforming, syngas can later be converted to diesel via Fischer-Tropsch processes (FT) or methanol synthesis using different catalysts.

However, due to high stability of methane, high operating temperatures are required, which results with low product selectivity especially in direct routes. Thus, currently, indirect routes are preferred in large scale production in industry due to higher development of technology [9].

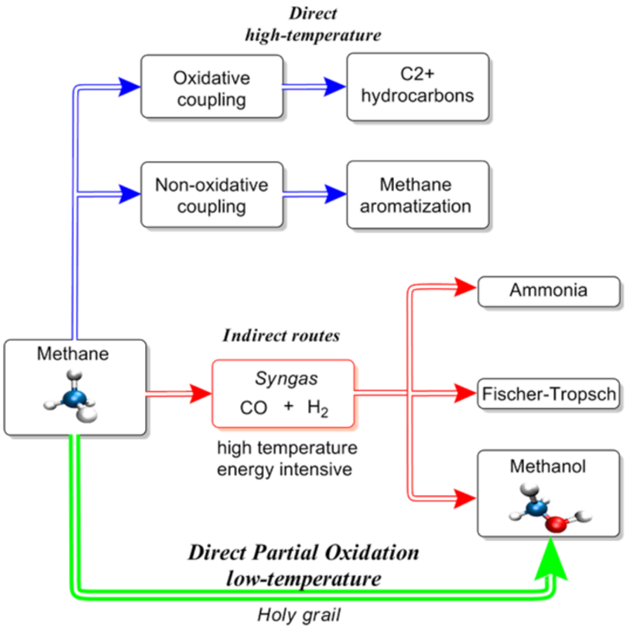

Figure 1.2 Possible routes for methane utilization in chemical industry [9]

1.2 Methanol

Methanol is a good candidate for methane valorization since it is highly versatile and easily transportable. Methanol can be used as an alternative fuel to diesel due to high energy storage or it can be used as a raw material for production of other chemicals [10]. Methanol can directly be used as transportation fuel with volumetric energy density of 15.6 MJ/L [11]. It is also considered as a clean burning fuel due to causing less amount of sulphur or nitrogen oxide emmisions [12]. Methanol can also be used as an industrial feedstock for methanol to olefin (MTO), methanol to gasoline (MTG), dimethyl ether (DME), acetic acid, formaldehyde or methyl tertbutyl ether (MTBE). The possible routes for methanol conversion to other valuable products are given in Figure 1.3. The current methanol production capacity is 110 million tones per year (MTY) and the methanol demand was 80–90 MTY in 2018. However, methanol demand is projected to exceed production capacity of 110 MTY in 2023 [13].

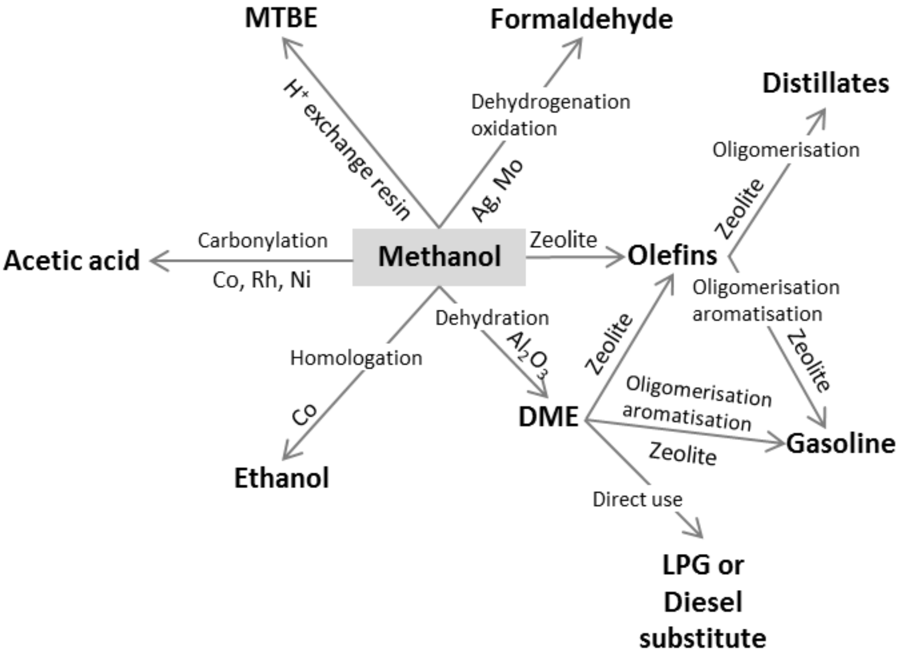

Figure 1.3 Possible routes for methanol conversion and supports used [11]

1.3 Methane to Methanol Conversion

1.3.1 Indirect Route

Methane conversion to methanol occurs through two different routes, which are called indirect and direct methane to methanol (MTM) reaction. Industrial application of methane to methanol takes place through indirect method, also known as syngas route, in which methane is firstly steam reformed to syngas at high temperatures (850–900 ºC) and relatively high pressures (30 bar) over Ni/Al_2O_3 catalyst. In the following step, syngas is converted to methanol at high pressures (50–100 bar) and milder temperatures (250–350 ºC) over $Cu/ZnO/Al_2O_3$ catalyst [14]. The reactions are given in Equations 1.1 and 1.2, respectively. Even though Ni supported catalysts are shown to prevent the undesirable reaction leading to coke formation, catalyst lifetime at these reaction conditions is a drawback [2]. Currently, the only economically viable conversion of methane to value added products is the syngas route [15]. The methanol selectivity obtained using syngas route is generally 99% with yields of 70–74% [15].

$$CH_4 + H_2O \rightarrow 3H_2 + CO \qquad \Delta H_{900\,°C} = 225.7\ kJ/mol \qquad \text{(Eqn. 1.1)}$$

$$CO + 2H_2 \rightarrow CH_3OH \qquad \Delta H_{25\,°C, 50\ bar} = -90.7\ kJ/mol \qquad \text{(Eqn. 1.2)}$$

This process is highly energy intensive due to high operating temperature and pressures and requires high capital costs mostly due to heat transfer equipment, which makes this route only viable in large scale production. Moreover, at high temperature and pressure operating conditions, low methanol selectivity is a drawback as well. The byproducts such as acetone or methyl ethyl ketone might be hard to separate via distillation [13]. Due to this highly costly industrial operation, an alternative process at milder conditions is searched for in small scale to convert methane to methanol on site to prevent methane flaring and for easier transportation.

1.3.2 Direct Methane Conversion to Methanol

In direct MTM reaction, methane is directly converted to methanol without additional steps such as syngas formation in an indirect route. The direct conversion of methane to methanol at milder temperatures are considered as one of the “holy grail” reactions since it is a challenge to activate methane and produce methanol selectively at milder temperatures [9].

1.3.2.1 Soluble Methane Monooxygenase (sMMO) Enzyme

Methane can be directly converted to methanol selectively in nature by methane monooxygenase (MMO) enzymes that can cleave highly stable C-H bond of methane at ambient conditions using O_2 as oxidizing agent [16]. The reaction that takes place is given in Equation 1.3. Nicotinamide adenine dinucleotide (NADH) is used as the energy source.

$$CH_4 + O_2 + NADH + H^+ \rightarrow CH_3OH + H_2O + NAD^+ \qquad \text{(Eqn. 1.3)}$$

Methane monooxygenase enzyme can be found in two forms, which are classified as particulate MMO (pMMO), which contains copper active sites, and soluble MMO (sMMO), which contains iron active sites [17]. Since MMO is an enzyme and enzymes are substrate specific, even though there are other hydrocarbons present, only methane is oxidized, and methanol is produced selectively without overoxidation. It is suggested that active sites in sMMOs are dinuclear Fe^{IV} species and the reaction occurs through hydrogen abstraction mechanism [16].

1.3.2.2 Zeolites as Catalysts

Metal loaded zeolites, mostly iron and copper, are also studied for direct MTM to mimic the nature. Direct MTM is divided into two processes, which are stepwise and continuous processes as shown in Figure 1.4. Stepwise process, also known as chemical looping or three-step process, is composed of three steps. The first step is activation, in which the catalyst is firstly activated at elevated temperatures (250–500 ºC) with an oxidizing agent to create the active sites. Then, methane is fed to activated catalyst and methane reaction takes place at mild temperatures (25–200 ºC). Lastly, formed methanol should be extracted from the surface since methane reaction takes place at low temperatures, an additional extraction process is required. For the methanol extraction step, various solvents are used such as acetonitrile solution or steam [18]. High selectivity of methanol (>95%) can be achieved mostly over copper exchanged zeolites via stepwise processes. However, the difference in temperatures in different steps cause constant cooling and heating processes and takes a long time. Also, the extraction step might cause the dilution of the product, which is also a drawback. On the other hand, in continuous or catalytic process, all the reactants, oxidizing agent (O_2 or N_2O), methane and in some cases water vapor is fed simultaneously to the reactor and reaction takes place in gas phase at temperatures 210–300 ºC with no extraction steps required. However, direct methane conversion to methanol has some challenges.

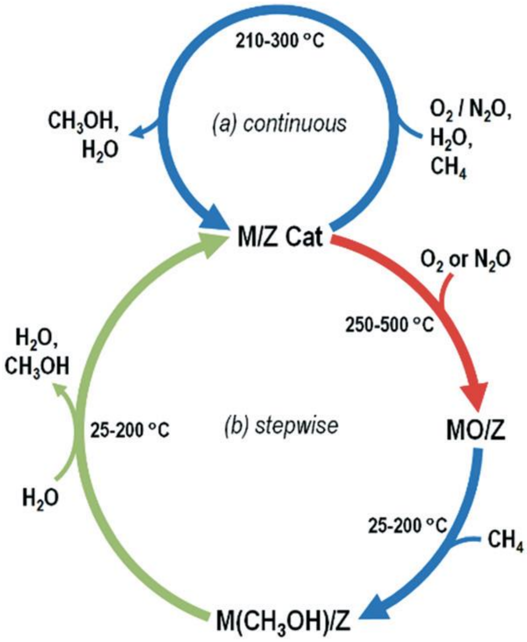

Figure 1.4 Schematic representation of direct conversion of methane to methanol [18]

1.3.3 Challenges in Direct Methane Conversion to Methanol

Direct continuous methane conversion to methanol is an alternative process to industrial application of MTM reaction in terms of eliminating high costs of the process. However, methane is a highly stable molecule with bond dissociation energy of 438.9 kJ/mol, whereas formed intermediates from methane conversion such as methanol has lower bond dissociation energy (402.1 kJ/mol) [19]. Thus, when the reaction conditions can oxidize methane, intermediates can readily be further oxidized to thermodynamically favorable products CO and CO_2, which results with low methanol selectivity [20], [21]. The selection of oxidizing agent is also important in terms of kinetic energy barrier. The activation energy of direct MTM reaction using O_2 is much higher than other oxidants such as N_2O and H_2O_2, which release oxygen atom easily. Thus, higher temperature or pressures are required for direct MTM with O_2 which promotes overoxidation. Also, using N_2O as oxidant might help the selective formation of oxygenates that could not be produced by O_2 [22].

1.3.4 Thermodynamic Analysis

Gaseq software is used for thermodynamic analysis of methane oxidation using N_2O. The equilibrium conversions of methane with respect to temperature in range of 100–500 °C is given in Figure 1.5 and conversion of methane increases with increasing temperature. The detailed Gaseq results at equilibrium without and with 24% H_2O in feed are given in Tables A.1 and A.2, Appendix A, respectively. At 300 °C, conversion of methane is found as 9.6 and 11.4% without and with 24% H_2O in feed.

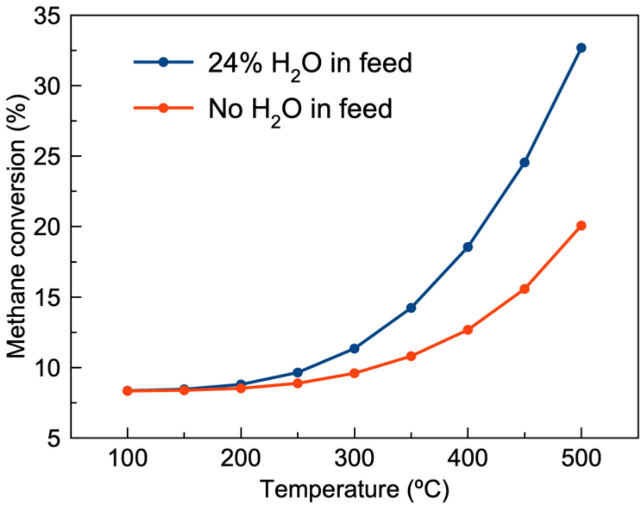

Figure 1.5 Methane conversion with respect to temperature with and without water vapor in feed

Carbon based product distribution is given in Figure 1.6. Equations 1.5 and 1.6 are used to calculate carbon products selectivity. The detailed product distribution is given in Appendix A. However, the amounts of carbon based products other than CO and CO_2 are negligible. Thus, only CO, CO_2 and CH_3OH, desired product, selectivity are given in Figure 1.6.

$$n_{C\,products}(mol) = r_{CH3OH} + r_{CO} + r_{CO2} + 2 * (\sum r_{C2}) + 3 * (\sum r_{C3}) \qquad \text{(Eqn. 1.4)}$$

$$S_i\,(\%) = \frac{n_i}{n_{C\,products}} * 100\% \qquad \text{(Eqn. 1.5)}$$

As can be seen from Figure 1.6, with and without water vapor in feed, thermodynamically favorable products are CO and CO_2. At high temperatures (>300 °C), CO becomes most favorable product. Higher methanol selectivity is obtained when water vapor is included in feed. In order to prevent overoxidation and produce methanol selectively, zeolites are used catalysts.

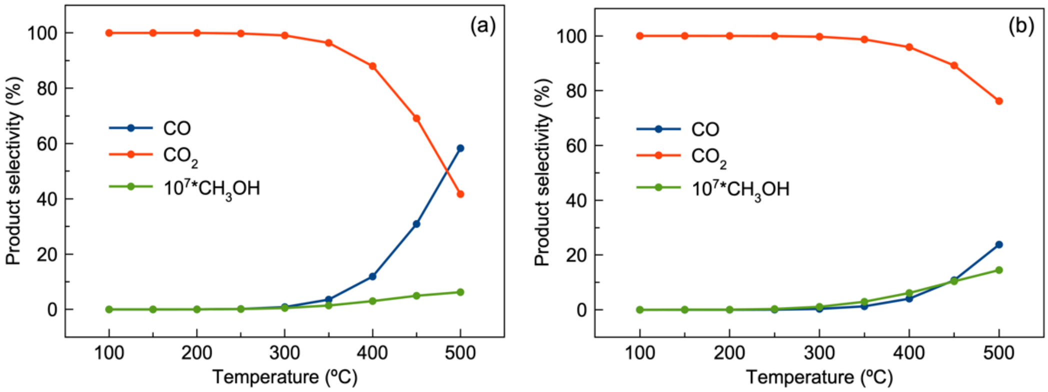

Figure 1.6 Product distribution (a) without and (b) with 24% H_2O in feed

1.4 Zeolites

Zeolites are highly crystalline microporous materials which are composed of primary building units of TO_4 tetrahedra where T is either Si^{4+} or Al^{3+} connected by four oxygen atoms (O^{2-}) [23]. The tetrahedral structures of SiO_4 and AlO_4 are shown in Figure 1.7. Due to three-dimensional structure of SiO_4 tetrahedra, channels and cages are formed in the cavities. Physiosorbed H_2O molecules are found in the open cavities [24].

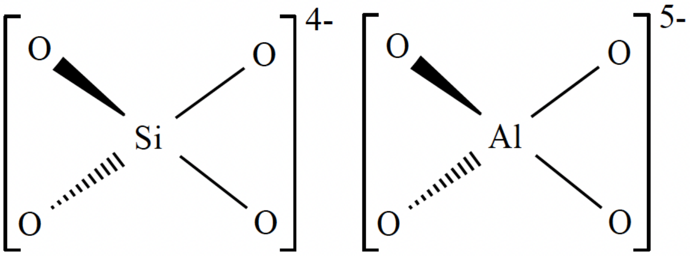

Figure 1.7 Tetrahedral structures of SiO_4 and AlO_4 [23]

The general structural formula of zeolites is expressed as $M_{2/n} \cdot Al_2O_3 \cdot ySiO_2 \cdot zH_2O$ where n is the cation valence, y demonstrates the Si/Al ratio of the zeolite and z represents the amount of water in the cavities [25].

Two Al tetrahedra cannot bound to each other and there must be at least one Si tetrahedra binding two Al tetrahedra according to Lowenstein rule [26]. The presence of Al^{3+} in the framework causes negative charge in the framework $(AlO_{4/2})^-$ and should be balanced by cations, which provides zeolite ion-exchange property [27]. Al content of a zeolite which is usually expressed as Si/Al ratio is important for the application field.

Zeolite frameworks are denoted by three letter codes given by Commission of the International Zeolite Association (IZA) and according to IZA, there are 255 framework type codes are assigned up to date [28].

Zeolites are also called as “molecular sieves” since the micropores do not allow the passage of molecules with larger diameter than zeolites pores [23]. This property of zeolites is important for shape selectivity in reactions. On the other hand, the small micropores of zeolites (<2 nm) causes diffusion limitations of reactants or products and to enhance mass transfer, hierarchical zeolites are investigated [29].

1.4.1 Si/Al Ratio

Si/Al ratio is an important parameter for zeolites since Al content affects the cation-exchange capacity and Si content affects the thermal stability. Thus, as Si/Al ratio is increased, zeolites exhibit lower ion-exchange capacity but higher thermal stability. These properties influence the applications of zeolites. For example, low Si/Al ratio zeolites have high ion-exchange capacity, which makes it a desirable material for detergent applications. Si rich zeolites are used in the field of catalysis due to their unique properties such as high surface area, large pore volume, crystallinity, ion exchange capacity, strong acidity, high thermal stability, and tunable pore sizes in synthetic zeolites [23].

1.4.2 Brønsted acidity

There are two type of acid sites present on zeolites which are Brønsted and Lewis acid sites. The Brønsted acid sites are formed by the bridging of hydroxyl groups with the framework Si and Al where extra-framework cations mostly act as Lewis acid sites [30]. These two types of acid sites are given in Figure 1.8.

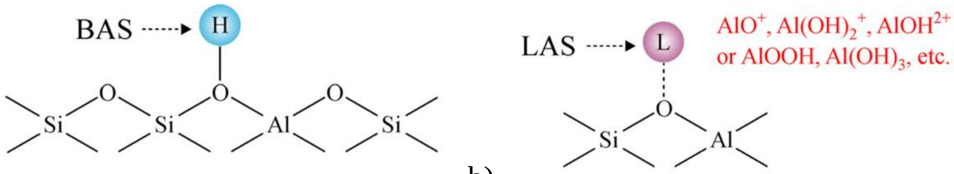

a) b)

Figure 1.8 a) Brønsted acid sites and b) Lewis acid sites on zeolites [30]

The acidity of a zeolite is an important parameter, and it can be controlled with Si/Al ratio. As the Si/Al ratio of a zeolite is increased, the Al content is decreased which is directly proportional to Brønsted acidity. The Brønsted acidity of two zeolites with different frameworks can vary even though they have similar or same Si/Al ratio. The acidity and Lewis or Brønsted acid sites formation of Fe-zeolite is dependent on iron loading method, zeolite framework and treatment after iron loading step. For example, heat treatment at high temperature could cause a decrease in Brønsted acidity.

The number and strength of the acid sites can be interpreted using Ammonia Temperature Programmed Desorption (NH_3-TPD) analysis but to specify the acid sites as Brønsted and Lewis acid sites pyridine FTIR spectroscopy is needed. The molecular diameter of pyridine is larger than ammonia, thus pyridine can not enter the small pore zeolites such as SSZ-13 and SSZ-39, which could result with observing lower acidity using pyridine FTIR in comparison to NH_3-TPD [31]. The bands obtained around 1545 and 1445 cm^{-1} upon pyridine adsorption are assigned to Brønsted and Lewis acid sites, respectively [32]–[34].

1.4.3 Synthesis of Zeolites

Zeolites are found in nature as minerals, or they can be synthesized hydrothermally in the presence of a solvent and heat treatment for specific uses. The natural zeolites are generally used for wastewater treatments, whereas synthetic zeolites are preferred in detergent industry or as adsorbents or catalysts due to higher purity [1], [35]. Zeolites are hydrothermally synthesized in an autoclave at high temperature. In a typical synthesis Si and Al sources as well as structure directing agent (SDA) are added to the solvent, mostly water is used, in alkaline medium and the gel is aged for some time for nucleation to start. After the nucleation is started, the gel is transferred to autoclaves and heated to crystallization temperature for some time for crystal growth. After the synthesis, the gel is either centrifuged or vacuum filtered to obtain the zeolites. The resulting zeolites are calcined at high temperatures to remove the organics.

1.5 Hierarchical Zeolites

As mentioned before, microporous structure of zeolites might cause mass transfer limitations for reactions involving large molecules and thus, meso- or macroporous materials are investigated. International Union of Pure and Applied Chemistry (IUPAC) classifies porous materials into three categories according to pore size such as micropores (<2 nm), mesopores (2–50 nm) and macropores (>50 nm) [36]. Hierarchical zeolites are zeolites containing both meso- and micropores and highly desirable since longer catalyst lifetime can be achieved and mass transfer limitations can be eliminated due to shortened diffusion pathway [37]. Mesoporous materials can be synthesized but the amorphous structure of mesoporous materials cause limited applications at high temperature reactions due to low thermal stability [38]. Thus, methods to incorporate mesopores in addition to micropores to zeolites with crystalline structure are investigated. Mesopores can be added to zeolites using either bottom-up or top-down approaches, which can also be referred as in- or post-synthesis methods. The formation of mesopores can be characterized by N_2 adsorption/desorption experiments.

1.5.1 Bottom-up Methods

In bottom-up strategies, mesopores are formed during zeolite crystallization process and bottom-up strategies are divided into three categories as hard templating, soft templating, and non-templating methods. In bottom-up strategies, mesoporogen is added to synthesis gel as another structure directing agent to form mesopores in addition to micropores. In hard templating method, solid state mesoporogen such as carbon nanotubes and nanoparticles [39], aerogels [40] or calcium carbonate [41] can be used. For soft templating method, generally surfactants such as cetyltrimethylammonium bromide (CTABr) are used to form mesopores [42]. Surfactant is added to synthesis gel after the nucleation is started. The intracrystalline mesopores are created when the template is removed by calcination after the synthesis. On the other hand, in non-templating method, no template is used and nanosized crystals are created by optimization of reaction conditions with intercrystalline mesopores [37].

1.5.2 Top-down Methods

In top-down methods, synthesized or conventionally obtained zeolite is exposed to post-synthetic methods to add mesopores. Dealumination and desilication processes are the extractions of framework Si or Al atoms to create intracrystalline mesoporosity. Since Si or Al is extracted from the framework, Si/Al ratio of the zeolite changes, which affects the acidity, thermal stability, and ion-exchange capacity of the zeolites.

Dealumination can be performed by steam treatment at 500–600 °C followed by acid washing or directly in acidic environment at elevated temperatures [43]. Washing is an important process after dealumination to remove all the Al extracted, otherwise extra-framework Al could be formed on zeolite surface. Dealumination can also be used to increase Si/Al ratio in applications where high thermal stability and high acid strength are important [44]. As an example, ultrastable zeolite Y (USY) is obtained from dealuminated form of zeolite Y (FAU) and USY is used as a catalyst in catalytic cracking reactions [45].

Desilication is the extraction of Si atoms from the framework in alkaline medium at elevated temperatures, which forms intracrystalline mesopores [43]. The treatment time, treatment temperature, concentration and type of base added are important parameters for desilication. If the conditions are harsh, Al could also be extracted from the framework and could not be removed from the zeolite pores in basic conditions and form extra-framework Al [43]. Si/Al ratio of treated zeolite is also important. For example, the optimal initial Si/Al ratio for desilication is determined as 25 to 50 for ZSM-5 [46]. When Si/Al ratio is in lower range, the high density of framework Al prevent the extraction of Si atoms and when Si/Al ratio is higher, uncontrolled silicon dissolution occurs, which cause formation of large pores [47].

1.6 Zeolites Used in This Study

In this study, the zeolites used are iron loaded micro- and mesoporous SSZ-13, SSZ-39 and Mordenite as well as microporous ZSM-5 and Ferrierite which have CHA, AEI, MOR, MFI, and FER framework structures, respectively.

1.6.1 SSZ-13 (CHA)

SSZ-13 has CHA (Chabazite) framework structure with unit cell dimensions of a=b=13.675 Å and c=14.767 Å and the framework density of CHA is 15.1 T atoms (Si or Al) per 1000 $Å^3$ [48]. SSZ-13 is a small pore zeolite composed of 8 MR (Membered Ring) channels (3.8 × 3.8 Å) and it has three-dimensional pore system [49]. The CHA framework structure is given in Figure 1.9. SSZ-13 consists of 8, 6 and 4 MR channels where main channel is 8 MR, and 6 MRs are connected by 4

MRs. Due to large cavities and small pore size, SSZ-13 is a widely used catalyst for selective catalytic reduction of NO_x with NH_3 [50], CO_2 adsorption [51], [52] and Methanol to Olefin (MTO) reactions [53], [54]. Hierarchical SSZ-13 is also investigated for MTO reaction [55], [56].

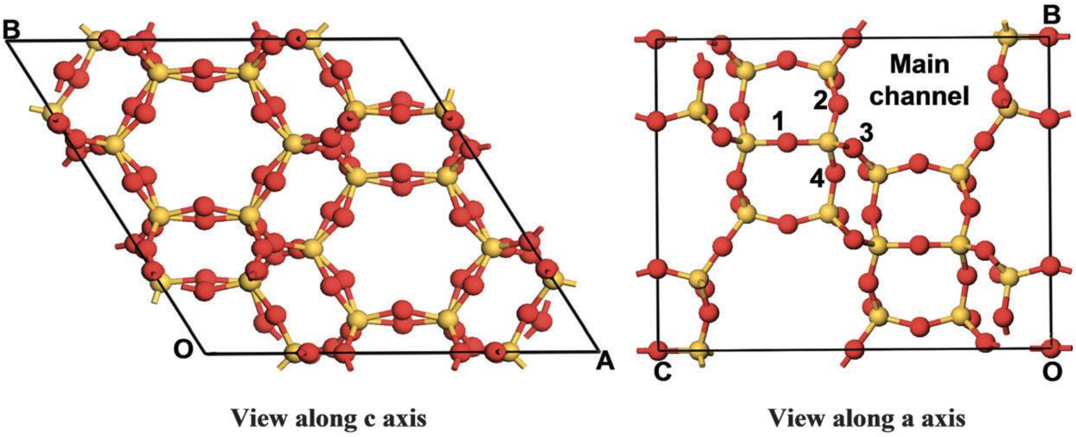

View along c axis View along a axis

Figure 1.9 Framework structure of CHA. Red represents Si atoms and yellow represents O atoms [49]

1.6.2 SSZ-39 (AEI)

SSZ-39 is a small pore zeolite having AEI framework structure. It is firstly discovered by Zones et al. in 1997 and patented in 1997 [57]. SSZ-39 has three-dimensional pore system with unit cell dimensions of a=13.677 Å, b=12.607 Å and c=18.497 Å and with framework density of 15.1 T atoms per 1000 $Å^3$ [28]. The AEI framework is given in Figure 1.10, and it is composed of 4, 6 and 8 MR channels (3.8 × 3.8 Å) [58]. Similar to SSZ-13, SSZ-39 is also investigated for NH_3-SCR [59]–[61] and MTO reactions [62]. Synthesis of hierarchical SSZ-39 is investigated to enhance mass transfer and mesoporous SSZ-39 is studied in MTO reactions applications as well [63].

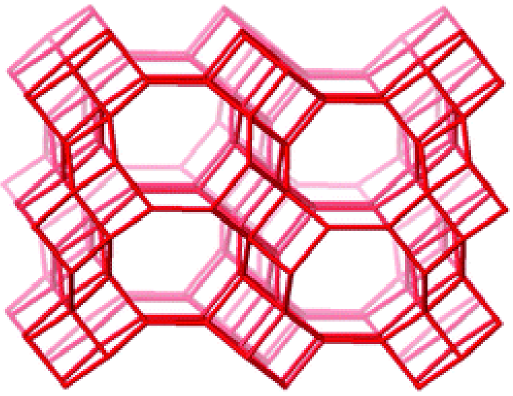

Figure 1.10 Framework structure of AEI [58]

1.6.3 Mordenite (MOR)

Mordenite belongs to MOR framework. MOR has unit cell dimensions of a=18.256 Å, b=20.534 Å and c=7.542 Å and the framework density of MOR is 17.2 T atoms (Si or Al) per 1000 $Å^3$ [28], [64]. MOR is a large pore zeolite consisting of straight 12 MR channels (7.0 × 6.5 Å) with parallel 8 MR channels (5.7 × 2.6 Å) as can be seen in Figure 1.11. These 12 and 8 MR channels are interconnected by side pockets of 8 MR channels (3.4 × 4.8 Å). Since side pockets are staggered with 8MR channels, diffusion is blocked from that direction and diffusion only occurs in one-dimension through the 12 MR channels [65]. The highest probability of positions of extra-framework cations are in β positions in 8 MR side channels and α positions in the 6 MR in the main channel, which are shown in Figure 1.9 with A and E, respectively [66]. Due to large pore size of MOR, it is used in several applications such as isomerization [67], [68] and carbonylation [69], [70]. The Brønsted acid sites in 12 MR are suggested to cause coke formation in dimethyl ether carbonylation, thus catalyst fouling [69], [70]. Hierarchical MOR is also used in catalytic cracking [71], [72], isomerization [73], carbonylation [74]–[76] and biomass conversion [77] applications.

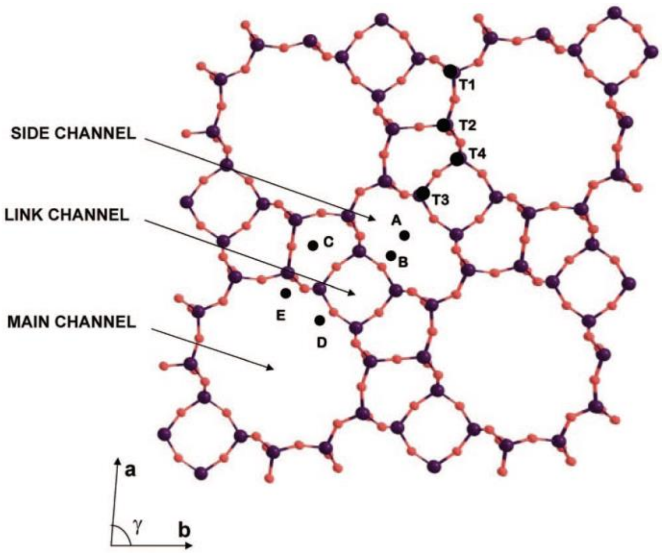

Figure 1.11 Framework structure of MOR [66]

1.6.4 ZSM-5 (MFI)

ZSM-5 (Zeolite Socony Mobile-5) exhibits MFI (Mordenite Framework Inverted) framework structure, and it is composed of straight 10 MR channels (5.1 × 5.5 Å) connected by sinusoidal 10 MR channels (5.3 × 5.6 Å) [78]. The unit cell dimensions of MFI framework are a=20.090 Å, b=19.738 Å and c=13.142 Å and the framework density of MFI is 18.4 T atoms per 1000 $Å^3$ [28]. ZSM-5 is a medium pore zeolite with two-dimensional channel system. The framework structure of MFI is given in Figure 1.12-a. The possible cation sites are shown in Figure 1.12-b, α-sites are in the 6 MR walls of the straight channel, β-sites are at the intersection of the straight and sinusoidal channels and γ-sites are the sites in 5 or 6 MRs in the sinusoidal channels [79], [80]. ZSM-5 has three-dimensional pore system. ZSM-5 is a widely studied zeolite since first synthesized in 1972 for MTO reaction [78], [81], [82] and petrochemical processes [83]–[86] due to its unique properties such as high thermal stability and tunable physicochemical properties, i.e., acidity, crystal size and morphology.

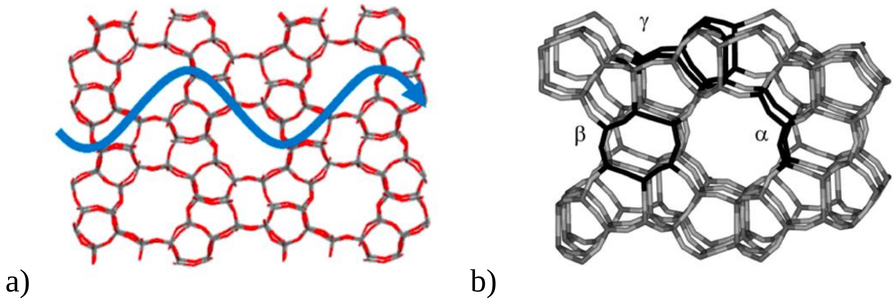

Figure 1.12 a) Framework structure of MFI. Blue arrow shows the sinusoidal channel through 10 MR [65] and b) Cation sites on MFI framework [80]

1.6.5 Ferrierite (FER)

Ferrierite exhibits FER framework structure which is given in Figure 1.13. The unit cell dimensions of FER framework are a=19.156 Å, b=14.127 Å and c=7.489 Å and framework density of FER is 17.6 T atoms per 1000 Å^3 [28], [87]. FER is composed of small and medium pores with 10 MR main channels (4.3 × 5.5 Å) and parallel 8 MR channels (3.5 × 4.8 Å) and two-dimensional pore system [87], [88]. The most probable positions of extra-framework cations in FER framework structure are indicated in Figure below with A and B which represent which are β-site in 6 MR side channel and α-site in 10 MR main channel [66]. FER is shown remarkable activity on the skeletal isomerization of 1-butene into isobutene [88] and production of light olefins via naphtha cracking [89].

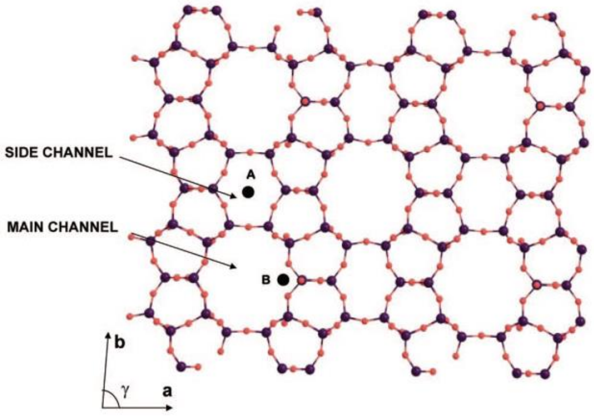

Figure 1.13 Framework structure of FER [66]

CHAPTER 2

LITERATURE REVIEW

The effect of metal used over MOR is investigated and the highest activity is observed over Fe-MOR followed by Ru-MOR and Cu-MOR, Cu-MOR showing higher methanol selectivity than Ru-MOR [90]. Copper or iron-exchanged zeolites are more often studied due to the similarity to copper or iron active sites on soluble or particulate methane monooxygenase enzymes that can activate methane at ambient conditions and selectively produce methanol. The most commonly suggested active sites for iron and copper loaded ZSM-5 formed upon N_2O decomposition are $[FeO]^{2+}$ and $[Cu_2(\mu\text{-}O)]^{2+}$ for Fe- and Cu-ZSM-5. Using Density Functional Theory (DFT) calculations, the methane activation energy over Fe- and Cu-ZSM-5 are calculated as 29 kJ/mol and 62 kJ/mol, respectively [18]. Thus, Fe-zeolites are more active for methane conversion than Cu-zeolites if the suggested sites are formed and Fe-zeolites could operate at lower temperatures due to lower energy barriers than Cu-zeolites.

2.1 Copper-Exchanged Zeolites

Direct stepwise conversion of methane to methanol is widely investigated in literature on copper-exchanged zeolites on a variety of frameworks such as MFI [91]–[93], CHA [94]–[96], AEI[97], MOR [95], [98]–[101], FER[97], [102], MAZ[97]. The summary of some reaction results for Cu-zeolites is given in Table 2.1. Groothaert et al. showed that methanol production with 98% selectivity is possible via stepwise process activation using O_2 at 450 ºC followed by methane reaction at 200 ºC [91]. Wulfers et al. showed Cu exchanged small pore zeolites (SSZ-13 and SSZ-39) are also able to produce methanol over 200 min with higher methanol production per gram and per Cu basis than Cu-MOR and Cu-ZSM-5 [96].

Park et al. carried out a comparative study over Cu- zeolites with different frameworks and found that the active sites that are in 8-membered rings are essential for high activity [97], also supported by theoretical studies [103]. Narsimhan et al. reported the catalytic (continuous) oxidation of methane to methanol feeding CH_4, O_2 and H_2O over different frameworks and concluded caged-based small pore zeolites (SSZ-13) exhibit higher reaction rates than larger pore zeolites (MOR, FER, ZSM-5) [92]. Dinh et al. showed high methanol selectivity can be achieved at high methane and water vapor pressures for continuous methane oxidation using O_2 with high Al and low Cu content Cu-SSZ-13 [104]. Continuous aqueous methane oxidation by H_2O_2 is also reported over Cu-ZSM-5 and Cu-*BEA [105]–[107]. However, catalytic conversion of methane to methanol using N_2O is not studied widely. Ipek and Lobo tested Cu-SSZ-13 for catalytic MTM reaction (feeding CH_4, N_2O and H_2O) and obtained methanol with 27% selectivity at 260 ºC [94]. Memioglu and Ipek were able to produce methanol with 499 µmol/g/h and 34% selectivity over Cu-SSZ-39 at 325 ºC feeding 40.5 kPa CH_4, 15.2 kPa N_2O and 4 kPa H_2O simultaneously [108].

Table 2-1 Methane to methanol reaction results over Cu-zeolites

Cu-zeolite	Si/Al	Cu/Al	Process	Oxidant	Activation temp. (ºC)	Extraction	Reaction temp. (ºC)	Methanol production (μmol/g)	CH_3OH/Cu (mol/mol)	Ref
ZSM-5	12	0.58	Stepwise	O_2	450 ºC	ACN	200	7	-	[91]
ZSM-5	11.5	0.34	Stepwise	O_2	450 ºC	Steam	200	16	0.03	[96]
MOR	5	0.34	Stepwise	O_2	450 ºC	Steam	200	31	0.04	[96]
SSZ-13	12	0.35	Stepwise	O_2	450 ºC	Steam	200	31	0.06	[96]
SSZ-39	10	0.26	Stepwise	O_2	450 ºC	Steam	200	36	0.09	[96]
MOR	5	0.30	Stepwise	O_2	450 ºC	Water	200	21	0.03	[97]
Omega	6	0.29	Stepwise	O_2	450 ºC	Water	200	86	0.09	[97]
ZSM-5	14	0.65	Stepwise	O_2	450 ºC	Water	200	9	0.01	[97]
FER	9	0.38	Stepwise	O_2	450 ºC	Water	200	10	0.02	[97]
SSZ-13	16	0.84	Stepwise	O_2	450 ºC	Water	200	30	0.04	[97]
ZSM-5	13	0.17	Catalytic	O_2	-	-	210	0.51*	0.003	[92]
MOR	11	0.14	Catalytic	O_2	-	-	210	0.30*	0.002	[92]
SSZ-13	14	0.50	Catalytic	O_2	-	-	210	3.5*	0.008	[92]
SSZ-13	23	0.22	Catalytic	O_2	-	-	270	6*	-	[104]
SSZ-13	12	0.18	Catalytic	N_2O	-	-	270	33*	0.36	[94]
MOR	5	0.08	Catalytic	N_2O	-	-	270	10*	0.26	[94]

Table 2.1 Methane to methanol reaction results over Cu-zeolites (Continued)

ZSM-5	10	0.38	Catalytic	N_2O	-	-	270	6*	3.80	[94]
SSZ-39	6	0.22	Catalytic	N_2O	-	-	300	90*	0.19	[108]
SSZ-39	6	0.22	Catalytic	N_2O	-	-	325	499*	1.05	[108]

*: μmol/g/h

2.2 Iron-Exchanged Zeolites

Additional to presence of dimeric iron centers in soluble methane monooxygenase enzyme that can catalyze methane activation using O_2 under ambient conditions, the unique activity of converting methane to C1 oxygenates observed over commercial H^+-ZSM-5 with trace amount of Fe impurity drew attention to iron containing zeolites [109]. The effect of support used for methane partial oxidation is studied over H^+-MOR, Fe-MOR, Fe-Al_2O_3, Fe-SBA-15 and Fe-SiO_2 and the highest activity is observed over Fe-MOR with no methanol formation observed over supports other than MOR [90]. Iron-exchanged zeolites can be oxidized using H_2O_2 and N_2O but not with O_2 [110], [111] due to higher bond dissociation energy of O_2.

2.2.1 Using H_2O_2 as Oxidant

The low temperature continuous partial oxidation of methane to methanol using H_2O_2 as oxidizing agent in aqueous medium is studied widely over Fe-ZSM-5 [105]–[107], [109], [112]–[118]. Additional to Fe-ZSM-5, Fe-MOR is studied and similar but less yield of C1 oxygenates are obtained with considerably less CO_2 formation over Fe-MOR than Fe-ZSM-5 [119]. The literature review of Fe-zeolites oxidized by H_2O_2 are given in Table 2.2.

Hammond et al. showed with the copresence of copper and iron ions with same iron content, higher methanol production of 189 μmol and methanol selectivity of 85% is observed with same methane conversion of 0.7% [109]. On the contrary, addition of Cu^{2+} to Fe-MOR did not promote methanol production significantly and resulted with lowered product yield but increased methanol selectivity from 20% obtained over Fe-MOR to 30% due to suppressed overoxidation [90]. In the reaction mechanism suggested by Hammond et al., methyl hydroperoxide is the first product and methanol are formed from CH_3OOH [107]. In the presence of •OH radicals, methanol can be overoxidized to formic acid and CO_2. However, the inclusion of Cu ions suppressed the •OH radicals which prevented overoxidation of methanol [106] and significantly decreased the formic acid formation from 164 to 0 μmol, thus enhanced the methanol selectivity from 12 to 85% [109]. The possible roles of Cu^{2+} in suppression of •OH radicals are suggested as either Cu acting as hydroxyl radical scavenger or inhibiting the ability of Fe^{3+} ions to produce OH radicals or restraining Fe^{2+} production or quenching OH radicals [106].

As a result of theoretical modelling and Extended X-ray Absorption Fine Structure (EXAFS) analysis, the active is suggested as a diiron complex $Fe_2(\mu_2\text{-}OH)_2(OH)_2(H_2O)_2]^{2+}$ with high spin Fe^{3+} centers for H_2O_2 partial oxidation [109] and the activation energy is found as 61 kJ/mol over Fe-ZSM-5 [107]. The binuclear active site is proposed to be located within the 10 membered rings of MFI framework with two Al^{3+} distances of 5–6 Å [112]. However, in the recent studies mononuclear iron species in extra-framework positions are suggested to be the active iron sites for partial methane oxidation [117], [119].

2.2.1.1 Brønsted acid sites

Fe-silicate-1 and Fe-ZSM-5 with the same iron content are compared by Hammond et al. and Fe-ZSM-5 produced twice of the total products of Fe-silicate-1 (197 and 91 μmol) with similar oxygenate selectivity (93 and 92%) indicating the importance of Al in framework, which is related to the Brønsted acidity [112]. Moreover, the inclusion of Al^{3+} or Ga^{3+} ions in framework is found essential for increasing cation-exchange sites that can stabilize cationic Fe^{3+} species and limit the formation of inactive iron species on the external surface of the zeolites and promote activity (~90 μmol for [Fe]-ZSM-5 and ~200 μmol for [Fe, Al]-ZSM-5 and [Fe, Ga]-ZSM-5) [112]. The effect of Brønsted acidity is also shown by comparing hydrothermally synthesized (M, Fe)-ZSM-5, M being Al, Ga or B, and Na^+ exchanged Al,Fe-ZSM-5 with a fixed Si/M ratio. The activity of these zeolites is found proportional to the Brønsted acidity determined by FTIR spectroscopy of pyridine adsorbed samples, which are given in descending order of Al,Fe-ZSM-5≥Ga,Fe-ZSM-5>>B,Fe-ZSM-

5. As Brønsted acidity decreased, methane conversion, formation rates and TOF oxygenates are decreased, where methanol selectivity is increased [118]. Si/Al ratio and framework also affect the acidity of the sample. The effect of changing Si/Al from 11.5 to 40 is investigated and a considerable decrease is observed on acid strength and concentration determined using NH_3-TPD. The methanol production rate obtained over Fe-ZSM-5 is found ten times of Fe-Beta with similar Si/Al ratio due to higher acidity [106]. The optimized range of Si/Al ratio over ZSM-5 is suggested to be 20–50 in terms of catalytic activity and ion-exchange capacity [115].

2.2.1.2 Aluminum Distribution

Al distribution also plays an important role for formation of iron species and directing Al to be single or pair Al in framework can be controlled by changing SDA used during synthesis. Using only tetra-propylammonium cations (TPA^+) as SDA in synthesis is suggested to form paired Al, where co-addition of Na^+ ions to TPA^+ is suggested to lead to single Al positioning in MFI framework [79], [120]. Two samples of Fe-ZSM-5 with similar Si/Al ratio are synthesized with single or paired Al and it is observed that higher iron-exchange capacity is obtained over Fe-ZSM-5 with paired Al compared to Fe-ZSM-5 with single Al [115]. Moreover, significantly higher amount of inactive iron species, iron oxide and larger iron oxide aggregates, are obtained over Fe-ZSM-5 with single Al compared to paired Al Fe-ZSM-5 regardless of the lower iron content on single Al Fe-ZSM-5 suggesting paired Al stabilizes iron species in extra-framework positions [115].

2.2.1.3 Iron Loading Method

The preparation method of Fe-zeolites and iron precursor, divalent or trivalent, also affect the formation of iron species. Kim et al. compared the iron species distribution of Fe-ZSM-5 prepared by wet impregnation or ion-exchange using UV–Vis spectroscopy. The highest activities are obtained over Fe-ZSM-5 prepared using divalent iron precursor. Trivalent iron precursors cause the formation of inactive iron oxide and larger iron oxide aggregates on the zeolite surface [114]. Then, other preparation methods such as solid-state ion-exchange, chemical vapor impregnation and hydrothermal synthesis are compared to wet impregnation and aqueous ion-exchange. The highest catalytic activity for oxygenates formation is obtained over Fe-ZSM-5 prepared by aqueous ion-exchange method with lowest methanol selectivity where wet impregnated and hydrothermally synthesized Fe-ZSM-5 resulted with low activity and high methanol selectivity. The reason of high activity of aqueous ion-exchanged Fe-ZSM-5 is the highest fraction of extra-framework Fe and lowest fraction of iron oxide and agglomerate species obtained over it compared to other samples. The study of Kim et al. shows the catalytic activity of Fe-ZSM-5 strongly depends on iron species formed during preparation method [116]. Also, the increase in iron content is shown to decrease the turnover frequency of oxygenated products even though the total amount of production is increased. The overoxidation products such as formic acid and CO_2 were formed since formed spectator iron species convert more H_2O_2 but not methane resulting with methanol or other intermediates’ overoxidation and low methanol selectivity [113], [117]. Moreover, the effect of heat treatment on iron species is investigated over hydrothermally synthesized Fe-silicate-1. The migration of framework Fe species to extra-framework as well as an increase in iron oxide clusters and agglomerates is observed as heat treatment temperature is increased from 550 to 900 ºC [113].

Table 2-2 Methane to methanol reaction results using H_2O_2 as oxidant

Catalyst	Si/Al	Fe content (wt.%)	H_2O_2 Conc. (M)	Reaction temp. (°C)	P_{CH4} (bar)	Methanol yield (µmol)	TOF (1/h)	S_{CH3OH} (%)	X_{CH4} (%)	Ref
Fe-ZSM-5	30	2.5	0.50	50	30.5	22.3	-	12	0.7	[109]
Cu-ZSM-5	30	0.0014	0.50	50	30.5	65.3	-	83	0.3	[109]
Cu-Fe-ZSM-5	30	2.5	0.50	50	30.5	188.8	-	85	0.7	[109]
Fe-ZSM-5	30	0.5	0.50	50	30.5	20.0	81^{*}	20	0.31	[113]
Fe-ZSM-5	30	2.5	0.50	50	30.5	31.4	40^{*}	14	0.77	[113]
Fe-ZSM-5	15	2.16	0.50	50	30.5	29.2	-	-	-	[106]
Fe-Beta	12.5	Fe/Al=0.02	0.5	50	30.5	2.9	-	-	-	[106]
Fe-ZSM-5	15	1.5	0.123	50	20	48 µmol/h	0.1^{**}	15	0.4	[105]
Cu-ZSM-5	15	-	0.123	50	20	97.5 µmol/h	21^{**}	89	0.2	[105]
Cu-Fe-ZSM-5	15	1.5	0.123	50	20	121.5 µmol/h	0.3^{**}	92	0.5	[105]
Fe-ZSM-5 (WI with $FeCl_2$)	15	0.46	0.277	50	31	-	16	8	0.74	[114]
Fe-ZSM-5 (IE with $FeSO_4$)	15	1.07	0.277	50	31	-	7.1	7	0.87	[114]
Fe-ZSM-5 (single Al)	26	0.14	0.5	50	30	10.0	$\sim 140^{***}$	3	-	[115]

Table 2.2 Methane to methanol reaction results using H_2O_2 as oxidant (Continued)

Fe-ZSM-5 (pair Al)	23	0.46	0.5	50	30	10.0	~1500***	5	-	[115]
Fe-ZSM-5 (pair Al)	23	1.11	0.5	50	30	20.0	~1000***	7	-	[115]
Fe-ZSM-5	13.5	0.1	0.5	50	30	177.0	66	16	1.1	[117]
Fe-ZSM-5	13.5	2	0.5	50	30	214.0	4	9	2.3	[117]
Ga, Fe-ZSM-5	15	Fe/Al=0.075	0.5	50	30.5	39.5	248***	14	0.95	[118]
Al, Fe-ZSM-5	15	Fe/Al=0.075	0.5	50	30.5	24.6	209***	10	0.8	[118]
B, Fe-ZSM-5	15	Fe/Al=0.075	0.5	50	30.5	8.1	57***	17	0.2	[118]
Na, Fe-ZSM-5	15	Fe/Al=0.075	0.5	50	30.5	1.1	3***	29	0.05	[118]
Fe-MOR	12.5	0.5	0.5	80	30	40.0	-	20	-	[90]
Cu-Fe-MOR	12.5	0.5	0.5	80	30	50.0	-	30	-	[90]
Fe-ZSM-5	23	0.5	0.5	80	30	9.0	747*	2	-	[119]
Fe-MOR	12	0.5	0.5	80	30	28.8	527*	9	-	[119]

*: TOF partial oxygenated species formed/(mol Fe)/h

**: TOF mol methane converted/mol Fe/h

***: TOF all products

2.2.2 Using N_2O as Oxidant

In the early 1990s, Panov group discovered the catalytic activity of H^+-ZSM-5 with trace amount of iron in it, in the form of Fe_2O_3 added during synthesis, and observed highly active surface oxygen species formation upon N_2O decomposition over iron site which is then called “alpha-oxygen (α-O)” [22]. This site is found highly reactive due to radical structure that it can activate methane even at room temperature [22], [121]–[123]. Iron loaded zeolites are tested for both stepwise (Fe-ZSM-5 [121], [123], [124] and Fe-SSZ-13 [125], [126]) and continuous (Fe-ZSM-5 [127]–[131], Fe-FER [129], [131], Fe-Beta [129], [132], Fe-MOR [133]) conversion of methane to methanol.

2.2.2.1 Stepwise Methane To Methanol Process

The results for partial oxidation of methane in stepwise processes are summarized in Table 2.3.

Methane can be activated at room temperature over Fe-ZSM-5 via direct stepwise process and produce methanol selectively but with low methanol yield due to slow kinetics [111], [121], [123]. As the methane reaction temperature is increased to 160 °C, methanol yield is promoted with a slightly lowered methanol selectivity [124]. Bols et al. investigated the effect of the presence of paired and unpaired Al in CHA framework with similar Si/Al ratio on the methanol formation and selectivity by changing synthesis conditions. The degree of paired Al is determined by Co^{2+} exchange capacity. It is shown that the presence of paired Al promoted the stability and formation of active sites, which resulted in higher methanol formation and turnover frequency [125]. Later, the activity of Fe-SSZ-13 is further enhanced almost five times by one-pot synthesis, in which iron is added during the hydrothermal synthesis not by post-synthesis methods such as ion exchange [126]. The aim of one-pot synthesis was to promote the formation of extra-framework iron instead of iron clusters, which are inactive iron sites for methane activation. One-pot synthesis for iron introduction is suggested as a more suitable way for preparing Fe-zeolites with high iron loadings and well dispersed iron sites since iron may not bond with all paired Al in framework in post synthesis methods [126].

Table 2-3 Direct stepwise methane to methanol reaction results using N_2O as oxidant

Catalyst	Treatment	Activation (N_2O)	Reaction temp. (°C)	Extracting solvent	Methanol yield (μmol/g)	Methanol TOF (μmol/mmol Fe)	S_{CH3OH} (%)	Ref
Fe-ZSM-5	Vacuum	240 °C	RT	Acetonitrile	5	-	80	[121]
Fe-ZSM-5	500 °C in vacuum	230 °C	RT	Ethanol	23	-	94	[123]
Fe-ZSM-5	500 °C in vacuum	230 °C	RT	Acetonitrile	70% yield	-	92	[123]
Fe-ZSM-5	900 °C in vacuum	240 °C	160	Acetonitrile	160	-	76	[124]
Fe-SSZ-13 (paired Al)	900 °C with He	160 °C	RT	Steaming	26.8	681	-	[125]
Fe-SSZ-13 (unpaired Al)	900 °C with He	160 °C	RT	Steaming	4	79	-	[125]
Fe-SSZ-13	900 °C with He	180 °C	RT	Steaming	134	270	-	[126]

2.2.2.2 Catalytic Methane to Methanol Process

Continuous partial methane oxidation to methanol using N_2O over Fe-zeolites is firstly reported by Parfenov et al. in 2014 [127]. The summary of catalytic conversion of methane to methanol over iron-exchanged zeolites is given in Table 2.4. Parfenov et al. also tested the catalytic selective methane oxidation to methanol over Fe-ZSM-5 with molecular oxygen at 300 ºC, however no methanol is detected but only overoxidation reaction takes place with CO and CO_2 formation [127].

2.2.2.2.1 Brønsted acid sites

The effect of Brønsted acid sites on catalytic partial oxidation of methane to methanol is investigated using iron loaded Silicate-1, ZSM-5 and Titanium Silicate-1 as catalysts with same MFI framework. ZSM-5 has Al cations in framework unlike Silicate-1 and Titanium Silicate-1 which have Si and Ti ions instead of Al, respectively. As can be seen from Table 2.4, even though iron provides small activity for methane activation and methanol selectivity, the presence of framework Al is essential for framework Al which is related with the Brønsted acidity of the samples [128]. The effect of calcination temperature and environment is also investigated on the methane activation since at high temperatures, framework Al can migrate to extra-framework positions, which would cause a decrease in Brønsted acid concentration and an increase in Lewis acid sites [134]. As the calcination temperature of Fe-ZSM-5 is increased from 550 to 900 °C, signigicant loss in activity is observed in methane and nitrous oxide conversions due to loss of acid sites with migration of framework Al, which is shown by FTIR spectra of pyridine adsorbed Fe-ZSM-5 [128]. Park et al. compared the acidity and methane reactivity over Fe-ZSM-5 and Fe-FER. Fe-FER has shown higher concentration of Brønsted acid sites and α-O sites than Fe-ZSM-5. The reaction results indicate that Fe-ZSM-5 is more selective for unsaturated hydrocarbons, ethylene and propylene, where Fe-FER is more selective for overoxidation products, CO and CO_2 [131].

Zhao and coworkers studied the catalytic conversion of methane to methanol over Fe-ZSM-5, Fe-Beta and Fe-FER and even in the absence of water vapor in feed and at relatively higher reaction temperature, 350 °C, in which MTO pathway is accelerated. 21% methanol selectivity is obtained over Fe-FER [129]. The highest number of Brønsted acid sites is obtained over Fe-FER, which is suggested to be the reason of higher activity in terms of conversion. The highest ethylene selectivity is obtained over Fe-ZSM-5, and the highest overoxidation product selectivity is obtained over Fe-Beta, which resulted in low methanol selectivity. The methanol selectivity is found as 3 and 5%, for Fe-ZSM-5 and Fe-Beta respectively. In-situ FTIR spectra of CH_4 and N_2O adsorbed catalysts are compared, and it is found that formed methoxy groups migrate from iron centers to silanol groups over Fe-FER, where methoxy groups staying on active iron sites are more prone to be overoxidized or go through MTO pathway [129].

2.2.2.2.2 Water Vapor Effect

Water vapor is used for both indirect and direct routes for methane conversion to methanol to prolong catalyst lifetime and promote methanol desorption from the surface. Excess steam is supplied in indirect route of methanol formation from methane via syngas, since highly used Ni based catalysts enhance the carbon formation leading to deactivation of the catalyst [135]. Also, Wood et al. showed no methanol is detected after direct CH_4 reaction with N_2O in the absence of water. However, with H_2O introduction to the feed, formed surface methoxy groups are hydrolyzed even though low methanol selectivity (2%) is obtained [136].

The catalyst fouling caused by coke formation is an important problem to overcome for catalytic MTM. Coke is suggested to be formed by migration of methanol or methoxy groups to nearby Brønsted acid sites [130]. In Brønsted acid sites, MTO pathway is accelerated in which methanol is converted to dimethyl ether, ethylene and eventually coke [127], [128], [130]. Water vapor is suggested to competitively adsorb on Brønsted acid sites and promote methanol desorption from the surface and prevent coke formation, which could promote the methanol selectivity [127], [130]. Parfenov and coworkers observed continuous methanol production on Fe-ZSM-5 via feeding methane, co-feeding N_2O and water vapor at temperatures of 275 ºC and 300 ºC and achieved a methane conversion of 0.75% and a methanol selectivity of 42% (calculated methanol production rate of ~129 μmol/g/h) at 300 ºC and 30% water vapor in the feed. The observed increase in methanol selectivity from 1.9 to 42% by increasing water vapor concentration from 0 to 30% is related to the dramatic decrease in coke amount from 2800 to 58 μmol C/g at 300 ºC [127]. Chow et al. also studied the effect of water vapor in the feed and similarly observed that methanol selectivity increased ten times from 1.4% to 16% with 20% water vapor addition to water free system [130]. Li et al. also studied the presence of water vapor on methanol selectivity over Fe-, Cu- and Fe- *BEA samples and even though slight decrease in CH_4 and N_2O conversions are observed, methanol production rate and selectivity are promoted mostly due to suppression of coke formation [132]. It is proposed that H_2O participates in the reaction through proton-transfer route and direct the reaction to methanol formation and desorption [132], [137].

2.2.2.2.3 Iron Loading Method

Park et al. investigated the formation of active iron species on samples (Fe-ZSM-5 and Fe-FER) using H_2-TPR (Temperature Programmed Reduction) analysis and concluded that samples prepared by impregnation method exhibit higher number of active sites compared to samples prepared by ion-exchange method [131]. The exchange methods, solid-state and aqueous ion-exchange, are compared over Fe-FER prepared by using $FeCl_3.6H_2O$. Higher proportion of loaded iron is in extra-framework positions in Fe-FER prepared by aqueous ion-exchange where Fe-FER prepared by solid-state ion-exchange method exhibit larger amount of Fe_xO_y clusters and bulk iron oxide. At similar methane conversions, the selectivity of oxygenated products is found higher over Fe-FER prepared by solid-state ion-exchange method [138].

2.2.2.2.4 Extra-framework Al

Extra-framework Al added to Fe-ZSM-35 by post synthesis methods such as solid-state ion-exchange method is shown to enhance N_2O decomposition since presence of extra-framework Al helps formation and reduction of binuclear Fe sites [139]. Similarly, extra-framework Al is added to MOR with solid-state exchange method using $Al(NO_3)_3.9H_2O$ by Li et al. It is observed by increasing the amount of extra-framework cations added by post synthesis methods, the formation of active iron sites with the extra-framework Al is stabilized, and the formation of inactive iron species such as iron oxide species is limited. Thus, higher activity in terms of reactants conversions is obtained with higher oxygenates selectivity over Fe-MOR with increased amount of extra-framework Al [133].

2.2.2.2.5 Copresence of Cu and Fe Cations

The synergistic effect of bimetallic of Cu and Fe cations to in BEA promoted both formation rate (259 versus 42 and 101 μmol/g/h) and selectivity of methanol (72 versus 14 and 0.2%) compared to Cu- or Fe-only zeolites, respectively [132]

Table 2-4 Direct catalytic methane to methanol reaction results using N_2O as oxidant

Catalyst	Reaction temp. (ºC)	CH_4 (%)	N_2O (%)	H_2O (%)	Methanol rate (μmol/g/h)	S_{CH3OH} (%)	x_{CH4} (%)	x_{N2O} (%)	Ref
Fe-ZSM-5*	300	20	2	20	0	0	0.02	0.4	[127]
Fe-ZSM-5	300	20	2	0	ca. 28	2	3.6	58	[127]
Fe-ZSM-5	300	20	2	30	ca. 129	42	0.75	21	[127]
Fe-SIL-1	300	20	2	0	0.28	0.3	0.19	2	[128]
Fe-TS-1	300	20	2	0	0	0	0.05	0.4	[128]
Fe-ZSM-5 (calcined at 550 °C)	300	20	2	0	6.4	1.1	1.8	21.5	[128]
Fe-ZSM-5 (calcined at 950 °C)	300	20	2	0	18.7	13.7	0.2	4.4	[128]
Fe-ZSM-5 (impregnation)	280	68	27	0	ca. 127	20.1**	0.19**	2.3	[131]
Fe-ZSM-5 (ion-exchange)	280	68	27	0	ca. 87	15.4**	0.17**	1.52	[131]
Fe-FER (impregnation)	280	68	27	0	ca. 2023	19.6**	3.1**	5.4	[131]

Table 2.4 Direct catalytic methane to methanol reaction results using N_2O as oxidant (Continued)

Fe-FER (IE)	280	68	27	0	ca. 1714	21.4**	2.4**	4.8	[131]
Fe-FER (SSIE)	354	28	7	0	ca. 866	12	3	25	[138]
Fe-FER (IE)	354	28	7	0	ca. 721	10	3	30	[138]
Fe-ZSM-5	300	20	2	0	ca. 13	1	1.5	18	[130]
Fe-ZSM-5	300	20	2	20	ca. 412	16	3	15	[130]
Fe-ZSM-5	350	28	7	0	ca. 50	3	0.7	4	[129]
Fe-Beta	350	28	7	0	ca. 108	5	0.9	7	[129]
Fe-FER	350	28	7	0	ca. 1010	21	2	18	[129]
Fe-MOR (12% Al is in extra-framework)	300	33	33	0	ca. 223	12	0.9	2.5	[133]
Fe-MOR (16% Al is in extra-framework)	300	33	33	0	ca. 491	17	1.4	3.3	[133]
Cu-BEA	270	15	35	10	41.9	18	0.5	0.3	[132]
Fe-BEA	270	15	35	10	100.9	0.3	47	98	[132]
Cu-Fe-BEA	270	15	35	10	259.1	72	0.8	2	[132]

*: O_2 is used as oxidant not N_2O

**: conversions are given in terms of rate (mmol/g/h)

2.2.3 Active Sites for MTM Reaction using N_2O as Oxidant

As mentioned before, the active sites are called alpha-oxygen sites and formed upon N_2O decomposition over iron-exchanged zeolites. The proposed reaction mechanism of alpha-oxygen formation and methane reaction is given in Equations 2.1 and 2.2 [127].

$$N_2O + (Fe^{II})_\alpha \rightarrow (Fe^{III} - O^{\cdot -})_\alpha + N_2 \qquad \text{(Eqn. 2.1)}$$

$$CH_4 + 2(Fe^{III} - O^{\cdot -})_\alpha \rightarrow (Fe^{III} - OCH_3)_\alpha + (Fe^{III} - OH)_\alpha \qquad \text{(Eqn. 2.2)}$$

Since moieties of methane (H and CH_3) are adsorbed on the same α-O site that is bound to iron, the mole ratio of methane to α-O is suggested as 1:2. With the hydrolysis of the products obtained from (Eqn. 2.2), methanol is obtained. For stepwise processes, extracting solvents are used for the hydrolysis. α-O is found stable up to 300 °C but at temperatures higher than 365 °C, O_2 is released at 365 °C [123].

The suggested structures of α-Fe(II) and α-O are given in Figure 2.1. Using DFT studies over Fe-*BEA, α-Fe(II) species are assigned as mononuclear, high-spin species in square planar coordination and α-O species are mononuclear, high-spin species in square pyramidal coordination with a Fe–O bond distance of 1.59 Å. The optimum positions of α-Fe(II) and α-O sites are in β positions of six membered rings (β-6 MRs) with two Al opposite and closest to each other [140].

The number of α-O sites can be increased with high temperature calcination or steam treatment where framework Fe can migrate to extra-framework positions, that are more active, and go through "self-reduction" [111], [141], [142]. Moreover, iron loading method, iron precursor used, and type of zeolite also affect the number of α-O sites [131].

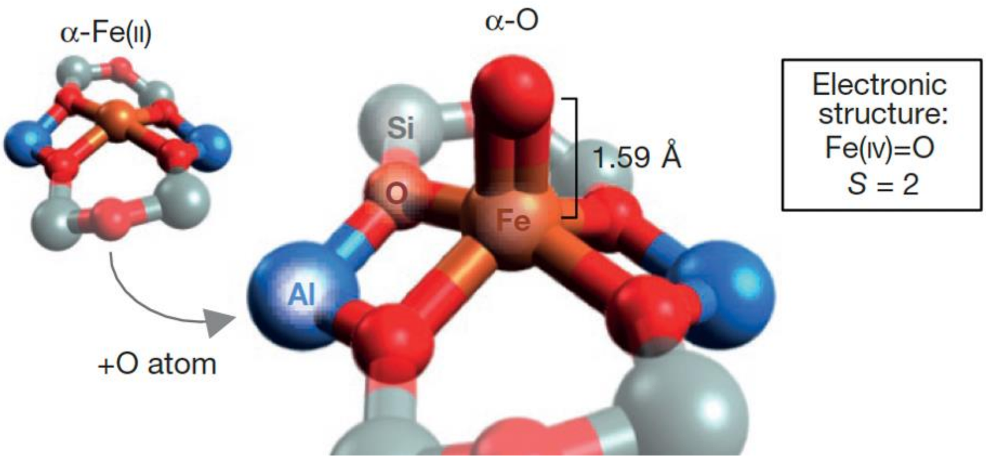

Figure 2.1 Computational elucidation of α-Fe(II) and α-O sites [140]

2.2.3.1 Reaction Mechanism

2.2.3.1.1 N_2O Decomposition

The N_2O decomposition over iron-exchanged zeolites are studied due to formation of highly reactive α-O sites that can activate highly stable methane and benzene molecules [22], [143]. When N_2O is decomposed over a Fe-zeolite, the O is ligand is bound to α-Fe(II) site and N_2 is released to the atmosphere. The DFT calculations for N_2O decomposition over $[Fe]^{2+}$-ZSM-5 showed that the N_2O molecule is firstly adsorbed on the active Fe center with -30.5 kJ/mol energy and N–O bond is cleaved with 57.3 kJ/mol activation energy [18].

The effect of framework on the N_2O decomposition over Fe-FER, Fe-*BEA and Fe-MFI and the superior activity of Fe-FER than Fe-*BEA and Fe-MFI is proposed to be due to the iron arrangement in two adjacent β sites with optimal Fe···Fe distances of 7–7.5 Å [144], [145]. Even though same coordination can occur in Fe-*BEA as well, the accessibility of β-6 MRs from batch faces in Fe-FER causes higher activity of N_2O decomposition than Fe-*BEA and Fe-MFI [144], [145].

2.2.3.1.2 Methane to Methanol Reaction

The possible catalytic route for methane to methanol conversion over a metal loaded and activated zeolite is given in Figure 2.2. The first step is the methane adsorption over the active site and formation of $[MO(CH_4)]^+$-ZSM-5 reactant complex. The TS1 represents the Transition State 1 where one C-H bond of methane is weakened by the active site and cleaved H is bound to oxo atom where methyl radical is bound to metal site. TS2 represents the Transition State 2 where OH and CH_3 moieties are recombined. As the last step, methanol is desorbed from the surface [146].

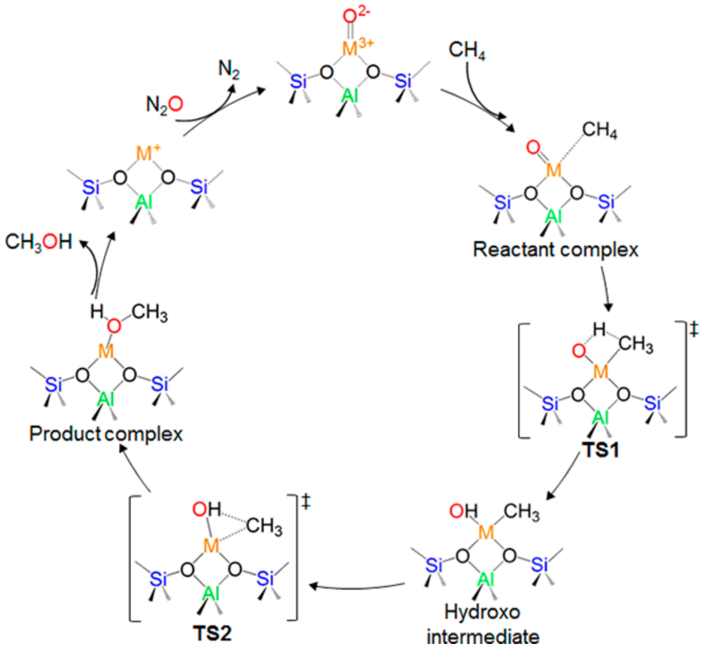

Figure 2.2 Possible reaction mechanism for direct methane to methanol conversion over metal loaded and N_2O activated zeolite [146]

Mahyuddin et al. performed the theoretical energy diagram calculations for direct methane to methanol conversion over $[FeO]^{2+}$-ZSM-5. The activation energy of methane, which is the C-H bond cleavage energy is calculated as 29.3 kJ/mol [18]. In another study, the bond cleavage energy of methane is calculated as 25.1 kJ/mol over $[FeO]^{2+}$-CHA [147], which suggests the confinement does not affect the reactivity of iron centers significantly. The similar activation energies obtained over $[FeO]^{2+}$-MFI and $[FeO]^{2+}$-AEI also supports this result [148]. The activation energy for the recombination of OH and CH_3 moieties is only 13.8 kJ/mol. The highest activation energy of 137 kJ/mol is observed on the desorption of methanol from the surface, which indicates the rate-determining step is the methanol desorption instead of the methane activation. The activation energy of overall reaction if calculated as 34.3 kJ/mol [18]. These results are obtained without taking water vapor into calculations. However, the inclusion water vapor in feed decreased methanol desorption energy from 223 kJ/mol to 126 kJ/mol over $[Cu_2(\mu\text{-}O)]^{2+}$ active site [149].

Methanol is produced on the active sites formed upon N_2O decomposition, Eqn. 2.3, and methanol is further converted to CO and CO_2 on the active sites. Methane can be directly converted to CO_2 on the active sites as given in Eqn. 2.4.

$$CH_4 + N_2O \rightarrow CH_3OH + N_2 \qquad \text{(Eqn. 2.3)}$$

$$CH_4 + 2N_2O \rightarrow CO_2 + 2H_2O + 2N_2 \qquad \text{(Eqn. 2.4)}$$

Also, on Brønsted acid sites, methanol is suggested to go through methanol to olefins mechanism in which methanol is converted to dimethyl ether first, then olefins and eventually coke as given in Equations 2.5 and 2.6 where n can be 2, 3 and 4.

$$2CH_3OH \rightarrow CH_3OCH_3 + H_2O \qquad \text{(Eqn. 2.5)}$$

$$CH_3OCH_3 \rightarrow C_nH_{2n} \rightarrow Coke \qquad \text{(Eqn. 2.6)}$$

$$2H_2CO + H_2O \rightarrow CH_3OH + HCOOH \qquad \text{(Eqn. 2.7)}$$

$$HCOOH \rightarrow CO + H_2O \qquad \text{(Eqn. 2.8)}$$

CO is suggested to be formed either with O_2 released from N_2O decomposition on the active sites or methanol is converted to formaldehyde which is converted to formic acid and CO is formed with formic acid dehydration, Equations 2.7 and 2.8. The proposed reaction mechanism over Fe-ZSM-5 is given in Figure 2.3 where B represents Brønsted acid sites.

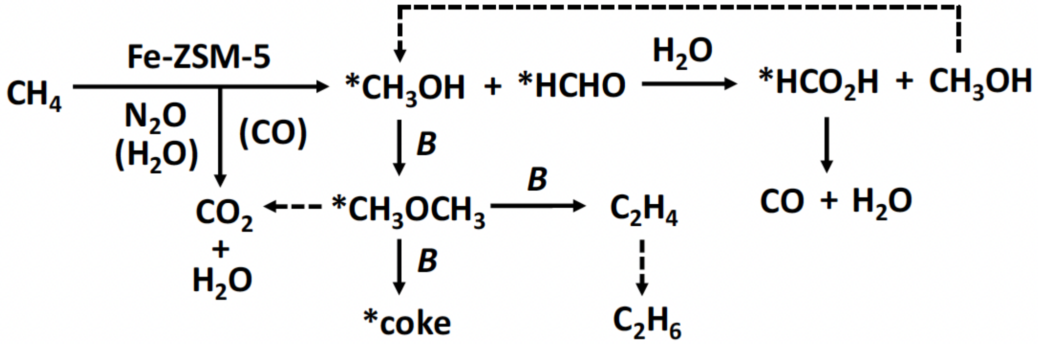

Figure 2.3 Proposed reaction mechanism for methane oxidation with N_2O over Fe-ZSM-5 [130]

2.2.3.2 Active Site Characterization

Diffuse reflectance UV–Visible Spectroscopy is a frequently used characterization technique to interpret the iron species. Most observed peaks are qualified as follows; i) the band between 200–250 nm is attributed to Fe^{3+} species located in the framework, ii) the band between 250–350 nm is attributed to isolated or oligonuclear Fe species in extra-framework positions, iii) the band between 350–450 nm is attributed to larger Fe_xO_y clusters and lastly iv) the bands observed at wavelengths higher than 450 nm are attributed to agglomerated iron oxide species that are found on the external surface of the zeolites [113]. However, the exact nature and composition of extra-framework Fe cannot be identified since broad range of possibilities (isolated, dimer, trimer, or small oligomers) show bands at the same region of 250–350 nm [112]. For further characterization of active sites, other spectroscopic techniques like Mössbauer spectroscopy or theoretical studies should be performed.

Mössbauer spectroscopy is a widely used spectroscopic technique to investigate the coordination and oxidation state of a metal which provide Mössbauer effect such as iron in heterogeneous catalysis [150]. This technique is used to characterize α-Fe(II) and α-O sites for methane conversion to methanol reaction as well [111], [122], [125], [140], [141], [144], [151] but only recently assigned to isomer shift components of 0.89 and 0.30 mm/s and quadrupole splitting of 0.55 and 0.50 m/s, respectively [125], [140].

Snyder et al. identified α-Fe(II) and α-O sites using in-situ DR-UV–Vis spectroscopy over activated Fe-*BEA at high temperature (900 °C for 2 hours) with He followed by reduction with hydrogen at 700 °C for 1 hour [140]. The activated Fe(II)-*BEA sample exhibit an intense peak at 250 nm with three weak bands at 629, 1111 and 2000 nm. After N_2O activation at 250 °C, a shift is observed on the band observed at 629 nm to 592 nm which indicates the formation of α-O sites from α-Fe(II) sites. Lastly, the spectra obtained after methane reaction over N_2O activated Fe(II)-*BEA shows the band at 592 nm is disappeared supporting the band at 592 nm is due to α-O formation and these sites are responsible for methane conversion. In conclusion, by using in-situ DR-UV–Vis spectroscopy, α-Fe(II) and α-O sites can be identified at 629 and 592 nm, respectively. These sites are proposed to be on the β-6 MRs with Al pairs on Fe-*BEA, which is the reason of observing similar spectra on Fe(II)-ZSM-5 and Fe(II)-FER but not on Fe(II)-MOR due to not having 6 MRs. Bols et al. showed that Fe-CHA also exhibit similar active site formation to α-sites on Fe-*BEA, Fe-ZSM-5 and Fe-FER with deviation due to 6 MR binding site geometry [125], [152]. Snyder et al. also performed variable-temperature variable-field magnetic circular dichroism (VTVH-MCD) spectroscopy and the band observed at 662 nm is correlated to the band at 629 nm in DR-UV–Vis spectra and attributed to α-Fe(II) sites [140].

2.3 Objective

The scope of this work is to produce methanol selectively from methane via continuous process using N_2O as oxidant at mild conditions, i.e., atmospheric pressure and at temperatures 270–340 ºC. Iron-exchanged zeolites with different frameworks and pore sizes which are SSZ-13 and SSZ-39 (small pore zeolites), and MOR (large pore zeolite) are investigated. The effect of mesopore addition to MOR, SSZ-13 and SSZ-39 is also studied and optimization of reactant compositions are performed over iron-exchanged mesoporous MOR due to higher selectivity and activity compared to small pore zeolites. Best performed zeolite, iron-exchanged mesoporous MOR is compared with the Fe-zeolites most studied in literature, i.e., FER and ZSM-5 at optimized conditions. Finally, the activation energies for methane and nitrous oxide conversions as well as methanol formation are compared over iron-exchanged FER and ZSM-5 and microporous and mesoporous MOR. The characterization of active sites is performed using Diffuse Reflectance UV–Visible Spectroscopy.

CHAPTER 3

EXPERIMENTAL METHODS

In this thesis, iron-exchanged zeolites with different pore sizes and frameworks are tested for catalytic conversion of methane to methanol. SSZ-13 and SSZ-39 (small pore zeolites), Ferrierite and ZSM-5 (medium pore zeolites) and Mordenite (large pore zeolite) are used. NH_4^+-Mordenite (MOR, Alfa-Aesar, 45877, Si/Al = 10), NH_4^+-Ferrierite (FER, Alfa-Aesar, 45884, Si/Al = 10) and NH_4^+-ZSM-5 (Alfa-Aesar, 45882, Si/Al = 40) are commercially obtained, while SSZ-13 and SSZ-39 are hydrothermally synthesized in the laboratory. In order to add mesopores, both in-synthesis methods and post-synthesis methods are applied to microporous zeolites. Mesoporous Mordenite is prepared using post-synthesis methods (such as dealumination and desilication) from conventional microporous Mordenite. However, mesopore addition to small pore zeolites (SSZ-13 and SSZ-39) using post-synthesis techniques is more difficult than mesopore addition to medium (ZSM-5) or large (MOR) pore zeolites. Small pore sizes (3.8 Å) found in SSZ-13 and SSZ-39 do not allow partial deterioration in the structure such as dealumination. Thus, mesoporogen is added to SSZ-13 and SSZ-39 gel mixtures after one day of nucleation, which is in-synthesis method for mesopore formation.

3.1 Catalysis Synthesis

3.1.1 Microporous SSZ-13 Synthesis

Microporous SSZ-13 is hydrothermally synthesized following a procedure reported by Pham et al. using a gel composition of $1SiO_2:0.035Al_2O_3:0.5TMAdaOH:20H_2O$ [153]. Firstly, 29.969 g of N,N,N-trimethyl-1-adamantanamonium hydroxide (TMAdaOH, Sachem, 20 wt.%) solution, used as structure directing agent, is mixed with 0.597 g aluminum ethoxide (Sigma Aldrich, 97 wt.%), which is used as aluminum source. The mixture is stirred at 25 °C for 15 minutes to dissolve the aluminum ethoxide. Then, 10.850 g of tetraethyl orthosilicate (TEOS, Merck, 98 wt.%) is added to mixture as silicon source and stirred at 25 °C for one more hour. The mixture is than placed into 35 mL Teflon-lined autoclaves and hydrothermal synthesis is carried out at 150 °C for 7 days under static conditions. After the hydrothermal synthesis, crystals are vacuum filtered and washed with 250 mL deionized water per gram of zeolite and dried overnight at 80 °C. The resulting zeolites are firstly heated to 120 °C and kept at 120 °C for 1 hour, then calcined at 580 °C for 6 hours using a flow furnace with 15 cm^3/min dry air flow. A heating rate of 1 °C/min is used. The sample is denoted as H^+-SSZ-13.

3.1.2 Microporous SSZ-39 Synthesis

Hydrothermal synthesis of microporous SSZ-39 is carried out using the gel composition reported by Ipek et al., which is $1SiO_2:0.019Al_2O_3:0.19SDA:0.25Na_2O:22H_2O$ [154]. Structure directing agent (SDA) given in the formula is tetramethyl piperidinium hydroxide (Sachem, Inc., 35.3 wt.%) for this synthesis. 6.690 of tetramethyl piperidinium hydroxide solution is mixed with 17.671 g de-ionized water, 12.840 g sodium silicate solution (Merck, 37 wt.% Na_2SiO_3, 26.5 wt.% SiO_2) and 1.026 g 1 M sodium hydroxide solution. The gel mixture is stirred at room temperature for 15 minutes. After a homogeneous, clear solution is obtained, 1.238 g NH_4^+-USY (Alfa Aesar, Zeolite Y, Si/Al = 6) is added slowly to mixture and stirred for 30 more minutes. Then the gel is transferred to 35 mL Teflon-lined autoclaves and hydrothermal synthesis is performed at 150 °C for 7 days using 45 rpm rotation. The crystals are recovered using vacuum filtration, washing, and drying overnight. The resulting zeolites are heated to 120 °C and kept at 120 °C for 1 hour and calcined at 560 °C for 8 hours using flow furnace to remove water and organics. The heating rate is arranged as 1 °C/min and dry air flowrate is set to 15 cm^3/min. The final product is denoted as Na^+-SSZ-39.

3.1.3 Mesoporous SSZ-13 Synthesis

Mesoporous SSZ-13 is hydrothermally synthesized using a gel formula given by Li et al. $1SiO_2:0.025Al_2O_3:0.1Na_2O:0.2TMAdaOH:44H_2O:0.12CTABr$ [155]. In synthesis, 38.977 g N,N,N-trimethyl-1-adamantanamonium hydroxide solution (TMAdaOH, Sachem, 20 wt.%) is used as structure directing agent and mixed with 0.979 g sodium hydroxide pellets (NaOH, Merck, 99 wt.%) and 114.870 g de-ionized water under stirring. After a clear mixture is obtained, 11.079 g fumed silica (Sigma Aldrich, 99.8 wt.%) is added slowly as silicon source for the synthesis and stirred until the mixture become homogeneous. Then, 0.855 g of sodium aluminate (Sigma Aldrich, 53 wt.% Al_2O_3) is added as the aluminum source. The mixture is stirred at room temperature for 2 hours and then transferred into 35 mL Teflon-lined autoclaves. The autoclaves are maintained at 160 °C for 1 day under static conditions. After that, autoclaves are taken out and 1.646 g cetyltrimethylammonium bromide (Sigma Aldrich, 98 wt.%, CTABr) is added as mesoporogen to the gel mixture using $1SiO_2:0.12CTABr$ ratio. After complete mixing of CTABr with the initial gel, final gel mixture is transferred back to Teflon-lined autoclaves and hydrothermal treatment is carried out for 11 more days at 160 °C in static oven. The crystals are vacuum filtered, washed and dried overnight. The sample is then heated to 120 °C and kept at 120 °C for 1 h following calcination at 580 °C for 10 hours using a 1 °C/min heating rate. The resulting product is denoted as Na^+-MesoSSZ-13.

3.1.4 Mesoporous SSZ-39 Synthesis

Mesoporous SSZ-39 is hydrothermally synthesized following a procedure proposed by Memioglu and Ipek [108]. For the initial gel, microporous SSZ-39 synthesis gel formula is used ($1SiO_2:0.019Al_2O_3:0.19SDA:0.25Na_2O:22H_2O$). Firstly, 6.690 g of structure directing agent tetramethyl piperidinium hydroxide solution (Sachem, Inc., 35.3 wt.%) is added to 17.671 g deionized water. Then, 12.840 g sodium silicate solution (Merck, 37 wt.%) as the silica source and 1.026 g NaOH solution are added to mixture and stirred until a homogeneous solution is obtained. After that, 1.238 g NH_4^+-USY (Alfa Aesar, Zeolite Y, Si/Al=6) is added slowly to the mixture as the silica and alumina source and stirred for 45 minutes. The gel mixture obtained is transferred into 35 mL Teflon-lined autoclaves and the autoclaves are rotated with 45 rpm at 150 °C for 1 day. Then, 3.462 g cetyltrimethylammonium bromide (Sigma Aldrich, 98 wt.%, CTABr) is added as mesoporogen to initial gel using SiO_2/CTABr ratio of 0.12. After a homogeneous solution is obtained, final gel is transferred into Teflon-lined autoclaves and kept at 150 °C for 6 more days using 45 rpm rotation. The sample is recovered using vacuum filtration, washed and dried at 80 °C overnight. The zeolite is then heat treated at 120 °C for 1 hour and calcined at 580 °C for 16 h using 1 °C/min heating rate. The resulting sample is denoted as Na^+-MesoSSZ-39.

3.1.5 Dealumination and Desilication of MOR

Post-synthesis treatment methods are applied to conventional microporous NH_4^+-MOR (Alfa Aesar, 45877, Si/Al = 10) for mesopore addition. Sequential dealumination, desilication and dealumination of H^+-MOR is applied as reported by Leng et al. [156]. For this purpose, NH_4^+-MOR is firstly heat treated at 550 °C for 4 hours to obtain H^+-MOR. Then, H^+-MOR is added to 2 M HNO_3 solution (20 mL solution/g zeolite) and stirred for 2 hours at 100 °C. After dealumination is completed, the zeolite is vacuum filtered and dried, and the resulting zeolite is heat treated at 550 °C for 5 hours. After calcination, desilication is performed using 0.2 M NaOH solution in which 20 mL solution is prepared per gram zeolite. After the desilication procedure, zeolite is recovered using vacuum filtration, washing, and drying. Lastly, resulting zeolite is dealuminated using 0.2 M HNO_3, 20 mL solution/g zeolite, at 50 °C for 1.5 hours. The final product is ammonium exchanged three times and calcined at 550 °C for 5 hours. During all heat treatment steps, 2 °C/min heating rate is used. The final product is denoted as H^+-MesoMOR. In this study, two different batches of MesoMOR are prepared which are denoted as MesoMORold and MesoMORnew.

3.2 Ion-Exchange Procedures

3.2.1 Ammonium-Exchange Procedure

Synthesized microporous and mesoporous zeolites that contain Na^+ ions are ion exchanged using aqueous solution of ammonium nitrate (NH_4NO_3, Sigma Aldrich, 99 wt.%) to obtain NH_4^+-zeolites. Between 1 to 3 grams of synthesized zeolites are stirred at 500 mL of 0.2 M NH_4NO_3 aqueous solution at 80 °C for 3 h. After the exchange, the zeolites are vacuum filtered, washed with de-ionized water and dried at 80 °C overnight. This exchange procedure is repeated three times. The resulting zeolites are firstly heated to 120 °C and kept at 120 °C for 1 hour and then heated to 550 °C and maintained at 550 °C for 5 hours to obtain H^+-form of the zeolites. After the heat treatment, zeolites are denoted as H^+-zeolite as given in Equation 3.1.

$$NH_4^+ - zeolite \overset{\Delta}{\rightarrow} H^+ - zeolite + NH_3 \qquad \text{(Eqn. 3.1)}$$

3.2.2 Iron-Exchange Procedure

Iron sulfate salt is used as iron source for NH_4^+-MOR, H^+-MesoMOR, H^+-SSZ-13, H^+-MesoSSZ-13, NH_4^+-SSZ-39, H^+-MesoSSZ-39, H^+-FER and H^+-ZSM-5. Aqueous iron-exchange to a synthesized small pore zeolite such as SSZ-13 and SSZ-39 is difficult due to limited iron diffusion and high propensity for iron oxide formation [126]. Thus, small pore zeolites should be exchanged with Fe^{2+} salt since ionic diameter of hydrated Fe^{2+} (2.5 Å) is smaller than hydrated Fe^{3+} (9 Å) [157].

For the aqueous ion exchange procedure, 1 gram of NH_4^+/H^+-zeolite is transferred into 100 mL deionized water first. Then the pH of the solution is arranged to 3 by dropwise addition of 1 M HNO_3 solution. The reason for keeping pH low is to prevent excess iron from turning into Fe^{3+} and precipitating. The solution is heated to 80 °C under N_2 flow and then the required amount of $FeSO_4.7H_2O$ (J.T. Baker, 98%) is added. After the salt is added, the solution is stirred under N_2 flow for 15 minutes and then N_2 flow is stopped, and the mixture is sealed. The solution is stirred at 80 °C for 3 hours. The amount of salt added is determined according to target Fe/Al ratio (See Appendix B). For microporous H^+-MOR, the effect of iron content on the direct conversion of methane to methanol is also investigated, thus several exchanges with different starting Fe/Al ratios are carried out. The resulting zeolites are denoted as Fe-MORx (x=starting Fe/Al ratio). For H^+-FER, one time iron-exchange with a starting Fe/Al ratio of 2 was not sufficient to reach the targeted iron amount. Thus, same iron-exchange procedure is repeated two more times with a starting Fe/Al ratio of 2. H^+-ZSM-5 is also iron-exchanged three times. The first exchange is performed using a Fe/Al ratio of 2, then consecutive iron-exchanges are carried out using a starting Fe/Al of 4. After the iron-exchanges are completed, zeolites are vacuum filtered, washed, and dried. The resulting zeolites are heat treated to remove sulfates. Zeolites are firstly kept at 120 °C for 1 hour and then heated to 550 °C and kept at 550 °C for 4 hours. Heating rate of 2 °C/min is used. The exchange conditions are given in Table 3.1.

Table 3-1 The iron-exchange conditions for NH_4^+/H^+-zeolites

Zeolite	Si/Al	Iron Conc. (M)	Starting Fe/Al	Exchange Conditions
NH_4^+-MOR	10	0.03	2	80 °C, 3 hours, pH=3
H^+-MesoMOR	20	0.02	2	80 °C, 3 hours, pH=3
H^+-SSZ-13	11	0.08	6	80 °C, 3 hours, pH=3
H^+-MesoSSZ-13	15	0.04	4	80 °C, 3 hours, pH=3
NH_4^+-SSZ-39	7.5	0.05	2.5	80 °C, 3 hours, pH=3
H^+-MesoSSZ-39	15	0.03	2.5	80 °C, 3 hours, pH=3
H^+-FER	10	0.03	2, 2, 2	80 °C, 3 hours, pH=3 (3 times)
H^+-ZSM-5	40	0.01, 0.02, 0.02	2, 4, 4	80 °C, 3 hours, pH=3 (3 times)

3.3 Characterization Techniques

In order to understand the phases and phase purity, surface area and pore volumes and distributions, elemental compositions, topology, iron species and defect sites of synthesized zeolites; X-ray Diffraction, N_2 adsorption experiments at -196 °C, Inductively Coupled Plasma-Optical Emission Spectrometer, Scanning Electron Microscopy, UV–Visible Spectroscopy and Magic Angle Spinning NMR Spectroscopy are used, respectively.

3.3.1 X-Ray Diffraction (XRD) Analysis

Powder X-Ray Diffraction (XRD) patterns are obtained using Rigaku Ultima-IV X-ray diffractometer in METU Central Laboratory. The scan rate of 1 °/min is used within 2θ range of 2–50 °. Cu Kα cathode tube (λ = 1.5418 Å) is used at 40 kV and 30 mA. XRD analysis is carried out after the calcination of synthesized or ion-exchanged samples. This analysis is used to observe the crystal structure.

3.3.2 Textural Analysis-N_2 Adsorption Tests

For surface and pore characterization, N_2 adsorption at -196 °C is performed using Micromeritics Tristar II 3020 surface area and pore volume analyzer in METU Chemical Engineering Department. The calcined samples are degassed in a vacuum set-up (Micromeritics VacPrep 061) at 300 °C for 6 hours under 150 μmHg vacuum conditions prior to N_2 adsorption experiments. After that, sample holders are filled with N_2 (Oksan, 99.999%) and sealed before transferring the holders to surface area and pore volume analyzer. The samples are further degassed at room temperature for 30 minutes and free volume tests are performed using He (Oksan, 99.999%). The free volume measurements were followed by vacuum treatment at room temperature for 2 more hours. Finally, the N_2 adsorption and desorption experiments are performed between relative pressure (P/P_0) values of 10^{-5} to 0.98 and at constant temperature of -196 °C. The t-plot method is used for micropore volume calculations. Barret-Joyner-Halenda (BJH) Adsorption model is used for pore size distributions. The mesopore volume is obtained by subtracting the t-plot micropore volume from the single point pore volume at $P/P_0=0.98$.

3.3.3 Scanning Electron Microscopy

Scanning Electron Microscopy (SEM) analysis is performed to examine the morphology of the zeolites. The analysis is carried out in Central Laboratory of

METU using QUANTA 400F Field Emission microscope operated at 20 kV. The calcined samples are coated with Pd-Au mixture prior to analysis.

3.3.4 Elemental Analysis

The elemental analysis of samples is performed using Inductively Coupled Plasma-Optical Emission Spectrometer (ICP-OES) in METU Central Laboratory to determine Si, Al, Na, Fe compositions). The instrument used is Perkin Elmer Optime 4300DV. The samples are dissolved in HF/HNO_3 solution to prior to analysis. Energy Dispersive X-ray (EDX) analysis is also used for elemental analysis using QUANTA 400F Field Emission scanning electron microscopy in METU Central Laboratory with 20 kV voltage. At least 5 regions are scanned to be accurate.

3.3.5 UV–Visible Spectroscopy

UV–Visible Spectrometer analysis is performed either by Perkin Elmer Lambda 35 UV–Vis Spectrophotometer in METU Central Laboratory between 200 and 800 nm or by Shimadzu 2600i Spectrometer in METU Chemical Engineering Department between 220 and 1400 nm. This analysis is performed to determine iron species of hydrated and dehydrated (N_2O and CH_4 treated) samples. 0.200–0.300 grams of hydrated Fe-zeolite samples (except Fe-SSZ-13, Fe-MesoSSZ-13, Fe-SSZ-39 and Fe-MesoSSZ-39) are mixed with 4 grams of Barium Sulfate ($BaSO_4$) prior to analysis. The analysis is performed at room temperature. For dehydrated and treated experiments, 3 grams of prepared Fe-zeolite and $BaSO_4$ mixture is used to fill the quartz U-tube. The spectra of Fe-zeolite and $BaSO_4$ mixture is taken to prior to treatments. N_2O treatment is performed using a total of 100 sccm flowrate; 10% N_2O and balance He, at 300 °C for 2 hours. After obtaining the spectra of N_2O treated samples, samples are treated with CH_4 using a total of 100 sccm flowrate; 30% CH_4 and balance He, at 300 °C for 1 hour. Then, spectra are taken for CH_4 treated samples.

3.3.6 Magic Angle Spinning Nuclear Magnetic Resonance

^{29}Si and ^{27}Al MAS NMR spectra analysis are performed on Bruker Superconducting FT NMR Spectrometer Avance TM 300 MHz WB in METU Central Laboratory. The instrument is equipped with a high power UltrashieldTM 300 MHz magnet and 4 mm MAS probe. The calcined samples are hydrated at room temperature prior to analysis.

3.4 Direct Methane to Methanol Reaction Procedure

3.4.1 Reaction Setup

The schematic of reaction setup is given in Figure 3.1. The setup mainly consists of a fixed bed reactor in which methane to methanol reaction takes place in a quartz tubular reactor and a gas chromatograph to analyze the results.

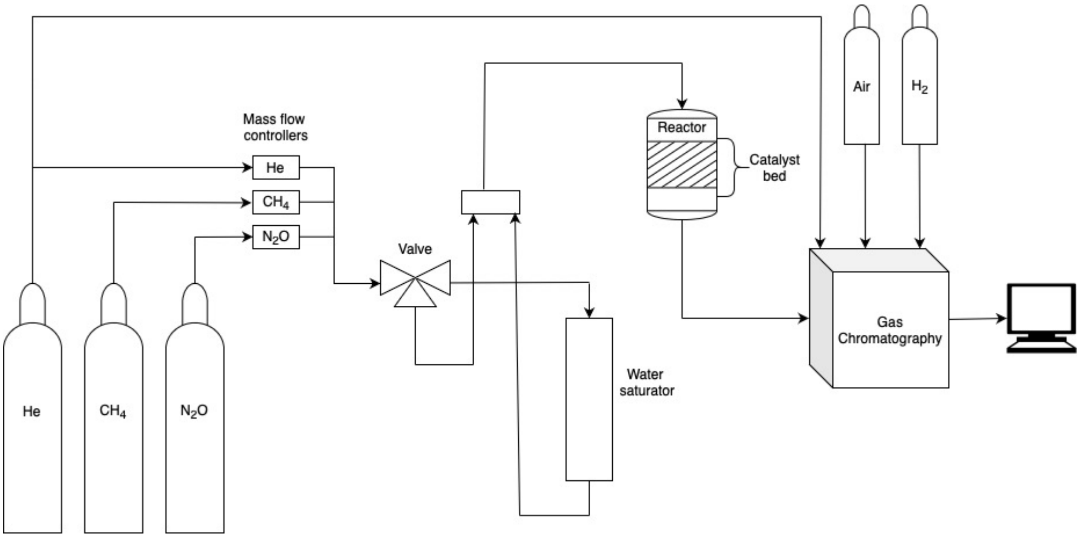

Figure 3.1 Experimental set-up for methane to methanol reaction

The flowrates of reactant gases are set using separate digital mass flow controllers (ALICAT, MC-100SCCM-D/5M). The total flowrate is also checked using a glass bubble flow meter. Three-way valve is placed between flow controllers and a stainless-steel water saturator. If the valve is opened through the water saturator, the gases flow through water saturator, which is filled with 100 mL deionized water and wrapped with a thermocouple and a heating tape. Otherwise, reaction takes place without water vapor. The quartz reactor is connected to stainless steel lines using Ultra Torr-Swagelok connections. The reactor is placed in a tubular vertical oven equipped with an Ordel PC771 temperature controller and a thermocouple placed at the center of the catalyst bed. The effluent gas is directed to Agilent 7820A gas chromatograph (GC) for qualification and quantification of products. The GC is equipped with a Pora-Plot Q column (CP7554, 25 m, 0.53 mm, 20 µm) and CP-Molsieve 5Å column (CP7538, 25 m, 0.53 mm, 50 µm) with a thermal conductivity detector (TCD) and flame ionization detector (FID). Both detectors are used simultaneously to analyze the products. Helium (Hatgaz, 99.999%), hydrogen (Hatgaz, 99.999%) and dry air (Oksan, 99.99%) are fed to GC at 5 bars as carrier inert gas and FID gases. Heating tapes are used to heat the inlet and outlet of the reactor to prevent condensation of water vapor and glass wool tapes are used for insulation. Method parameters for GC is given in Table 3.2.

Table 3-2 Gas chromatography method parameters

Injection sample volume	250 µL
Inlet Temperature	150 °C
TCD Temperature	250 °C
FID Temperature	300 °C
Column Pressure	21.4 psi
Oven Temperature	50 °C for 8 mins, heat to 160 °C using 20 °C/min heating rate, hold at 160 °C for 3 mins

The methanol and water calibrations are conducted by saturating inert He by methanol and water vapor placed in the saturator at 25 and 0 °C whereas calibration of other gases (CH_4, N_2O, N_2, CO, CO_2, CH_3OH, C_2H_6O, C_2H_4, C_2H_6, C_3H_6, C_3H_8,

C_4H_8, C_4H_{10}) are performed using standard gas samples. The retention time and response factors for reactants and products are given in Table 3.3.

Table 3-3 The retention time and response factors for reactants and products

Compound	Retention time (min)	TCD Response Factor (ppm/area)	FID Response Factor (ppm/area)
CH_4	8.32	35.15	2.23
N_2	6.80	8.95	
CH_3OH	13.22		1.46
DME	12.25		0.59
$C_2H_4^*$	4.30		3.57
$C_2H_6^*$	5.48		3.64
C_3H_6	10.00		0.26
C_3H_8	10.60		0.26
i-C_4H_{10}	14.01		0.21
i-C_4H_8	14.17		0.19
n-C_4H_{10}	14.32		0.19
n-C_4H_8	14.45		0.18
CO^*	2.85	74.4	
CO_2^*	4.01	77.5	

*: measured with another method using 5:1 split ratio

3.4.2 Reaction Procedure

The gases used for catalytic conversion of methane to methanol are methane (Hatgaz, 99.995%), nitrous oxide (Hatgaz, 99%) and helium (Hatgaz, 99.999). Also, water saturator is used to feed water vapor to the reactor. The flowrate of gas mixture is changed between 50 to 100 sccm for methane to methanol reaction. The reactants are fed simultaneously to 7 mm inner and 9 mm outer diameter 30 cm long quartz reactor. 0.300±0.005 gram Fe-zeolites that are pelleted at 60 bars for 3 minutes and sieved between 250 to 400 µm are stabilized in the reactor using glass wool. After

15 minutes of reactants flow at room temperature, water saturator valve is opened, and the temperature of water saturator is changed from 25 to 70 °C to obtain vapor pressure range of 3 to 22 kPa. After 15 minutes, reactor temperature is increased to the reaction temperature (270–340 °C) using a heating rate of 5 °C/min and maintained at that temperature (isothermal conditions) during the reaction. The effluent gas stream is analyzed every 21 minutes using the gas chromatograph. Firstly, micro-, and meso-porous zeolites with different frameworks (CHA, AEI, MOR, MAZ) are tested using a 50 sccm total flowrate, comprising 30% CH_4, 30% N_2O, 3% H_2O and balance He. Then, to increase methanol selectivity, further optimization studies are performed on Fe-MesoMORold by changing N_2O concentration in the feed from 10 to 30%, CH_4 concentration from 20 to 40% and water vapor concentration from 3 to 15 kPa. At optimum conditions, activation energy for methane and nitrous oxide conversions as well as methanol formation are calculated using rate data obtained between 270 and 340 °C.

3.4.3 Regeneration of Catalysts

Previously described set-up is used for regeneration of the catalyst and coke determination. The dry air (Hatgaz, 99.99%) flowrate is set to 75 sccm. The oven temperature is set increased to 550 ºC using a 5 ºC/min heating rate and maintained at 550 ºC for 2 hours during regeneration. The effluent CO_2 concentration is analyzed using the gas chromatograph (Agilent 7820A) in every 3 min. The total CO_2 amount is then calculated to be able to quantify the total coke amount. The total coke amount is then normalized with respect to the total reaction time to calculate the coke formation rate. The calculated coke rate is included in methane conversion rate and product selectivity calculations.

The formulas used to calculate product selectivity and turnover frequency of methanol are given in Equations 3.2 and 3.3. The sample calculations where below equations are used are given in Appendix C.

$$r_{CH4}(\mu mol/_{g\ cat*h}) = r_{CH3OH} + r_{CO} + r_{CO2} + 2*(\sum r_{C2}) + 3*(\sum r_{C3}) + 4*(\sum r_{C4}) + r_{Coke} \quad \text{(Eqn. 3.2)}$$

$$S_i(\%) = \frac{r_i}{r_{CH4}} * 100\% \quad \text{(Eqn. 3.3)}$$

$$TOF_{CH3OH}\left(\frac{\mu mol/_{g\ cat*h}}{mmol\ Fe/_{g\ cat}}\right) = \frac{r_{CH3OH}}{Fe\ content} \quad \text{(Eqn. 3.4)}$$

CH_4 and N_2O conversions are obtained using Equations 5 and 6:

$$X_{CH4} = \frac{r_{CH4}}{F_{CH4,fed}} * 100\% \quad \text{(Eqn. 3.5)}$$

$$X_{N2O} = \frac{r_{N2}}{F_{N2O,fed}} * 100\% \quad \text{(Eqn. 3.6)}$$

CHAPTER 4

RESULTS AND DISCUSSION

4.1 Characterization Results

4.1.1 X-Ray Diffraction

X-Ray diffraction patterns of synthesized micro- or meso- porous zeolites before and after ion-exchange procedure are investigated to observe changes in the crystal structure or in the crystal sizes using Cu Kα source (λ=1.5418 Å).

X-Ray diffraction patterns for conventional calcined MOR is compared with prepared mesoporous MOR (MesoMOR) and MesoMOR following iron-exchange (Figure 4.1). MesoMOR is prepared using post synthesis methods including dealumination in acidic medium and desilication in basic medium in two different batches. The zeolites from different batches are denoted as MesoMORold and MesoMORnew. The characteristic peaks of MOR framework are observed to be preserved on H^+-MesoMORold and H^+-MesoMORnew indicating that the crystal structure is preserved. Following the iron-exchange procedure, which is carried out in an acidic medium (pH 3), the MOR crystal sizes are observed to be slightly reduced. However, absence of additional peaks can be inferred as homogeneous Fe-exchange inside the pores of the zeolites.

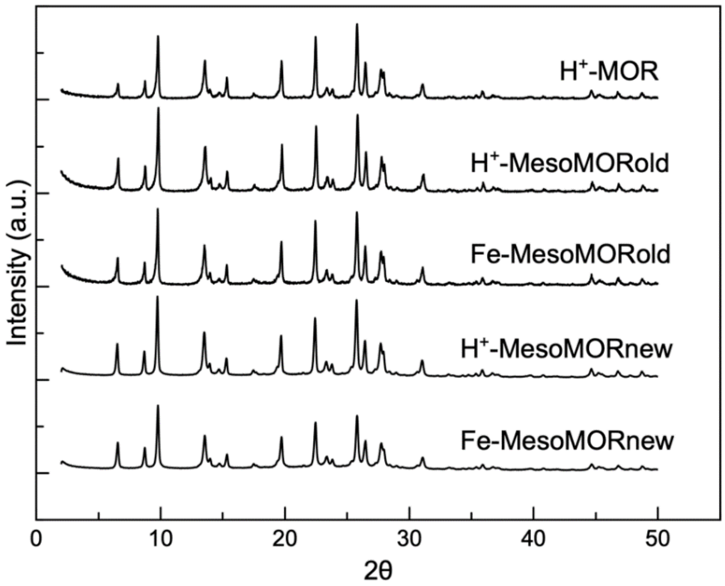

Figure 4.1 XRD patterns of MOR before and after mesopore addition and iron-exchange (λ=1.5418 Å)

XRD patterns for synthesized micro- and meso- porous SSZ-13 are given in Figure 4.2 before and after iron-exchange. The characteristic peaks for CHA framework are observed on H^+-SSZ-13 and H^+-MesoSSZ-13, which indicates successful synthesis of micro- and mesoporous SSZ-13. MesoSSZ-13 was synthesized by adding a mesoporogen, i.e., CTABr, to the synthesis gel. Higher relative intensity of peaks belonging to MesoSSZ-13 indicate larger crystals for MesoSSZ-13. No significant changes in crystal sizes or no additional phases are observed following the Fe-exchange.

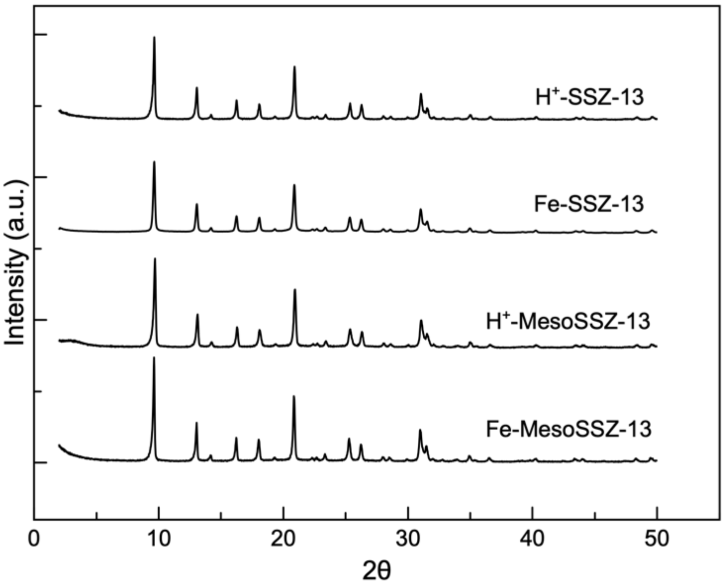

Figure 4.2 XRD patterns of SSZ-13 before and after mesopore addition and iron-exchange (λ=1.5418 Å)

XRD patterns for synthesized SSZ-39 and MesoSSZ-39 are given in Figure 4.3. MesoSSZ-39 was also synthesized using CTABr as mesoporogen in the synthesis gel. The characteristic peaks for AEI framework are observed for microporous H^+-SSZ-39, while additional peaks at 16° and 26° 2θ angles indicate an additional phase that is attributed to ANA (Analcime) framework. Following the Fe-exchange, no significant changes in the crystal sizes are observed for Fe-SSZ-39. However, the acidic medium for Fe-exchange resulted in dissolvement of some of the analcime phase in Fe-MesoSSZ-39.

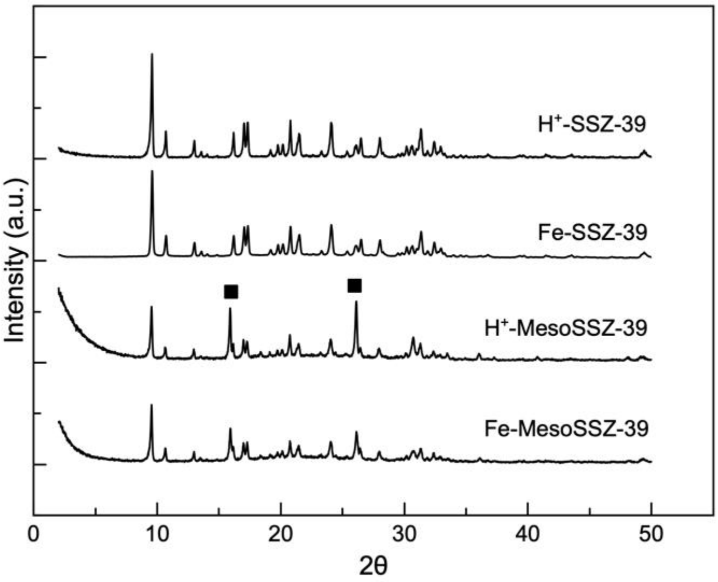

Figure 4.3 XRD patterns of SSZ-39 before and after mesopore addition and iron-exchange (λ=1.5418 Å)

XRD patterns of H$^+$-FER is compared with iron-exchanged FER in Figure 4.4. The obtained peaks are consistent with the characteristic peaks of FER framework and the crystal structure is not destructed during ion-exchange conditions.

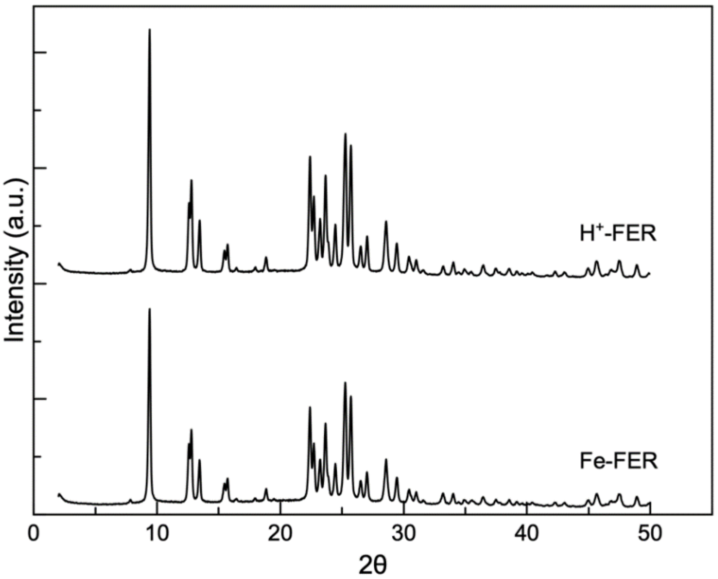

Figure 4.4 XRD patterns of FER before and after iron-exchange (λ=1.5418 Å)

XRD patterns of calcined version of commercially obtained ZSM-5 before and after ion-exchange procedures are given in Figure 4.5. There has been no change observed after the exchange and crystallinity is preserved.

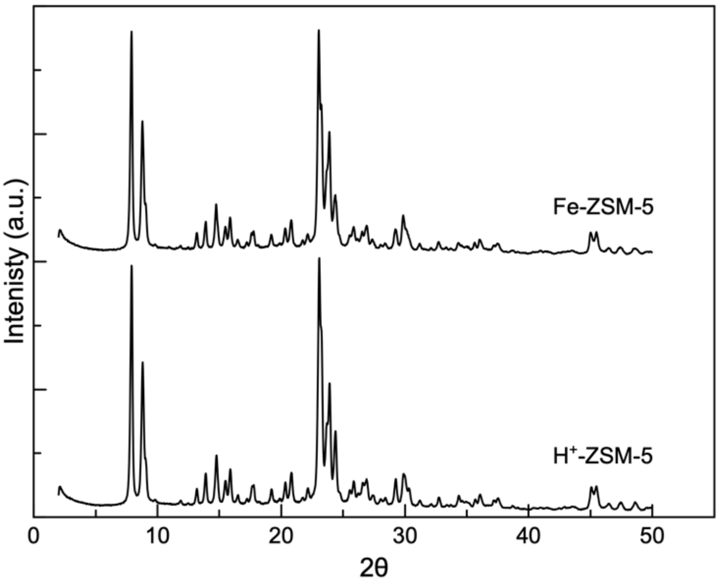

Figure 4.5 XRD patterns of FER before and after iron-exchange (λ=1.5418 Å)

X-Ray diffraction patterns of H^+-MOR and iron-exchanged MOR samples with different Fe content are given in Figure 4.6. It is seen that the acidic exchange conditions did not affect the crystallinity of MOR.

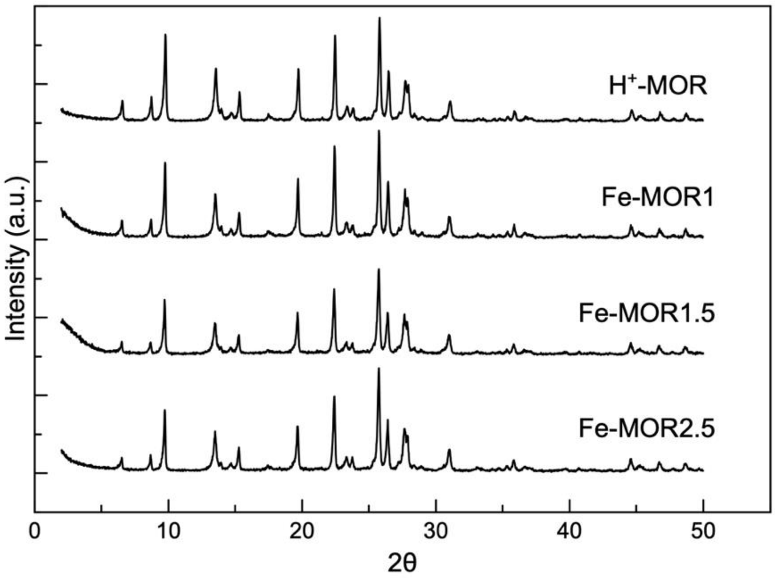

Figure 4.6 XRD patterns of MOR before and after iron-exchange (λ=1.5418 Å)

4.1.2 Elemental Analysis

Elemental analysis of iron-exchanged micro- and meso-porous zeolites are performed using Energy-dispersive X-ray (EDX) or Inductively Coupled Plasma (ICP) spectroscopy. The Si/Al and Fe/Al ratios are summarized in Table 4.1. Using these results, iron content (mmol Fe/g catalyst) is determined, which is used in turnover frequency calculations from reaction results.

Table 4-1 Elemental analysis results of iron-exchanged zeolites

Fe-Zeolite	Si/Al [(a)]	Fe/Al [(a)]	Si/Al [(b)]	Fe/Al [(b)]	mmol Fe/g cat
MOR0.25	9	0.18			0.280
MOR0.5	11	0.22			0.318
MOR0.75	10	0.22			0.319
MOR1	11	0.25			0.336
MOR1.5	11	0.30			0.398
MOR2.5	10	0.32			0.468
MesoMORold	30	0.30			0.161
MesoMORnew	25	0.32			0.203
FER	10	0.18			0.265
ZSM-5	44	0.38			0.137
SSZ-13			11	0.19	0.260
MesoSSZ-13			16	0.18	0.172
SSZ-39			8	0.15	0.290
MesoSSZ-39			14	0.20	0.224

(a): Elemental analysis performed by ICP-OES

(b): Elemental analysis performed by EDX

4.1.3 Scanning Electron Microscopy

Scanning Electron Microscopy (SEM) analysis is performed to investigate the crystal morphology and crystal size estimation. SEM images of iron-exchanged micro- and meso- MOR are given Figure 4.7. Crystals with different sizes and irregular shapes are observed on both micro- and meso- MOR samples. The crystal size decreases from between 1 to 1.5 μm to 0.2 to 1.0 μm range with mesopore addition. The smaller crystals indicated the formation of mesopores.

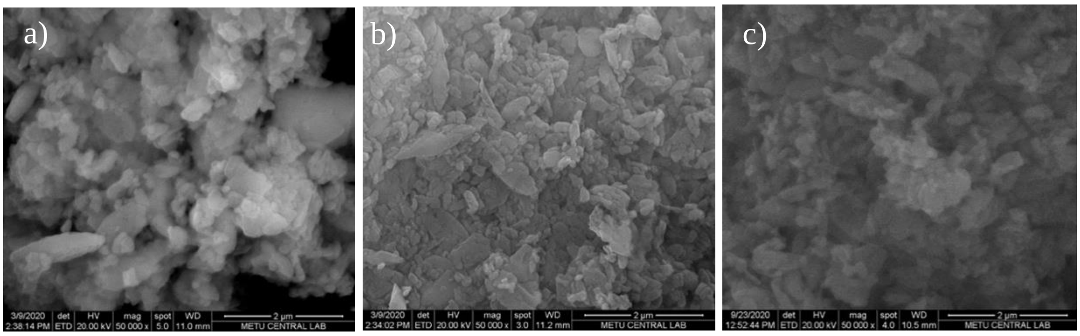

Figure 4.7 SEM images of a) Fe-MOR1.5, b) Fe-MesoMORold and c) Fe-MesoMORnew

Fe-SSZ-13 exhibits crystals with elliptic shapes as can be seen from Figure 4.8-a. However, addition of CTABr during synthesis for mesopore addition changed the morphology and Fe-MesoSSZ-13 have crystals with rhombohedral morphology (Figure 4.8-b). The crystal sizes increased with mesopore addition to range of 250 nm to 4 μm from 1 to 2 μm.

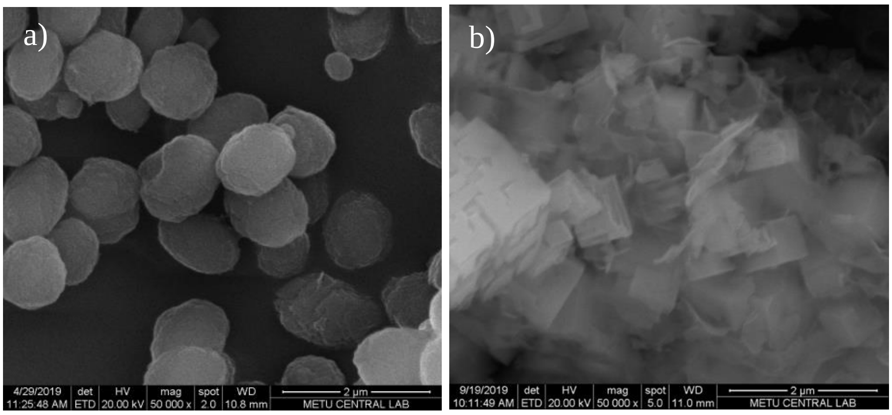

Figure 4.8 SEM images of a) Fe-SSZ-13 and b) Fe-MesoSSZ-13

SEM images of Fe-SSZ-39 and Fe-MesoSSZ-39 are given in Figures 4.9-a and 4.9-b, respectively. It can be seen from Figure 4-9a that Fe-SSZ-39 show typical orthorhombic crystals with 1.5–2 μm sizes whereas both orthorhombic and layered crystals are observed over Fe-MesoSSZ-39 with crystal size of 200 nm to 1μm (Figure 4.9-b). The extra phase obtained during synthesis of Meso-SSZ-39 with CTABr addition led to formation of extra phase of Analcime, shown in Figure 4.9-c, which exhibit spherical crystals with 6-7 μm size.

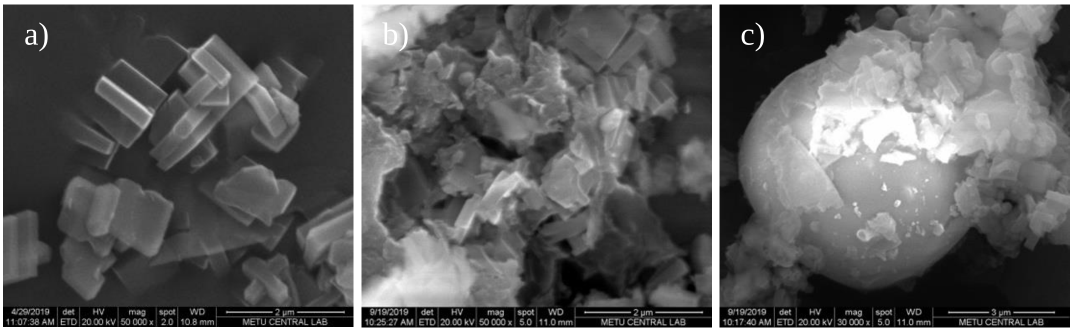

Figure 4.9 SEM images of a) Fe-SSZ-39, b) Fe-MesoSSZ-39 and c) Analcime phase

SEM images of Fe-ZSM-5 and H^+-FER are given in Figure 4.10-a and 4.10-b, respectively. Fe-ZSM-5 which has crystal sizes between 0.5 to 2 μm. H^+-FER exhibits crystals with sizes in range of 0.5 to 1 μm.

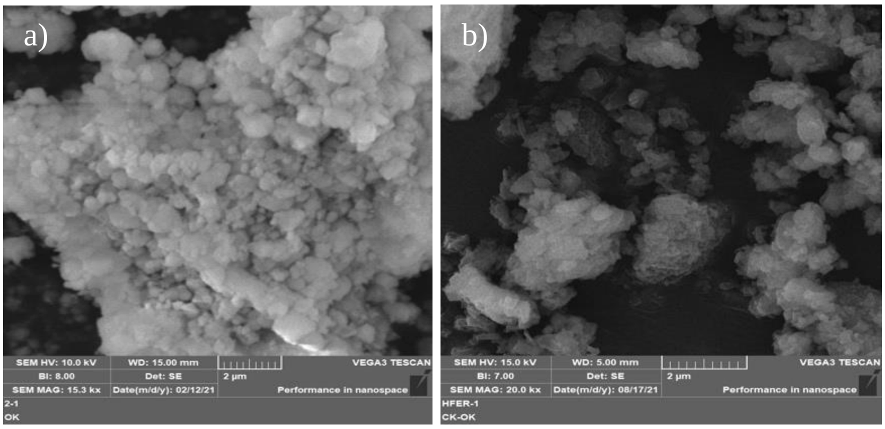

Figure 4.10 SEM images of a) Fe-ZSM-5 and b) H^+-FER

4.1.4 Textural Analysis

4.1.4.1 Pore Volume and Surface Area

Micropore and mesopore volumes are calculated using N_2 physisorption isotherms. Pore volumes and surface areas of samples are summarized in Table 4.2. Mesopore volumes are calculated by subtracting micropore volume from total pore volume. As can be seen from the Table 4.2, conventionally obtained microporous MOR (H^+ form) has 0.083 cm^3/g mesopore volume. Using three step post treatment methods, two dealumination and one desilication processes, mesopore volumes of 0.196 and 0.255 cm^3/g are reached for two different batches. Also, micropores are mostly preserved during these treatments in acidic and basic mediums. For MesoSSZ-13 and MesoSSZ-39 synthesis, mesoporogen, CTABr, is added during synthesis and 0.158 cm^3/g and 0.467 cm^3/g mesopore volumes are reached for MesoSSZ-13 and MesoSSZ-39, respectively. While micropore volumes are similar for micro- and meso- SSZ-13, low micropore volume of 0.054 cm^3/g is observed on H^+-MesoSSZ-39.

Table 4-2 Surface area and pore volumes of NH_4^+-, H^+- and Fe-exchanged zeolites

Sample	BET Surface Area	Langmuir Surface Area	V_{total}	V_{micro}	V_{meso}
	m^2/g		cm^3/g		
H^+-MOR	473	645	0.285	0.202	0.083
Fe-MOR1	421	573	0.259	0.187	0.072
H^+-MesoMORold	480	653	0.388	0.192	0.196
Fe-MesoMORold	445	606	0.373	0.177	0.196
H^+-MesoMORnew	499	681	0.449	0.194	0.255
Fe-MesoMORnew	475	645	0.418	0.185	0.233
NH_4^+-FER	296	402	0.179	0.132	0.047
Fe-FER	315	429	0.201	0.139	0.062
NH_4^+-ZSM-5	416	569	0.250	0.137	0.113
Fe-ZSM-5	429	591	0.278	0.098	0.180
H^+-SSZ-13	730	995	0.364	0.306	0.058
Fe-SSZ-13	651	886	0.259	0.259	-
H^+-MesoSSZ-13	570	774	0.395	0.240	0.155
Fe-MesoSSZ-13	574	779	0.399	0.241	0.158
H^+-SSZ-39	559	766	0.276	0.278	-
Fe-SSZ-39	476	501	0.235	0.235	-
H^+-MesoSSZ-39	749	1028	0.521	0.054	0.467
Fe-MesoSSZ-39	371	512	0.281	0.084	0.197

4.1.4.2 N_2 Adsorption/Desorption Isotherms

N_2 adsorption/desorption isotherms at -196 °C are given in Figures 4.11–4.16. In Figures 4.11 and 4.12, microporous H^+-MOR is compared with first and second batches of prepared mesoporous MOR before and after iron-exchange. The quantity of N_2 adsorbed on the pores increased at the same relative pressures with mesopore addition. Hysteresis is observed on both batches. Microporous MOR shows Type I isotherm with a sharp increase at low relative pressures where Fe-MesoMORnew sample showed Type IV isotherm with a H4 type hysteresis due to pore blocking.

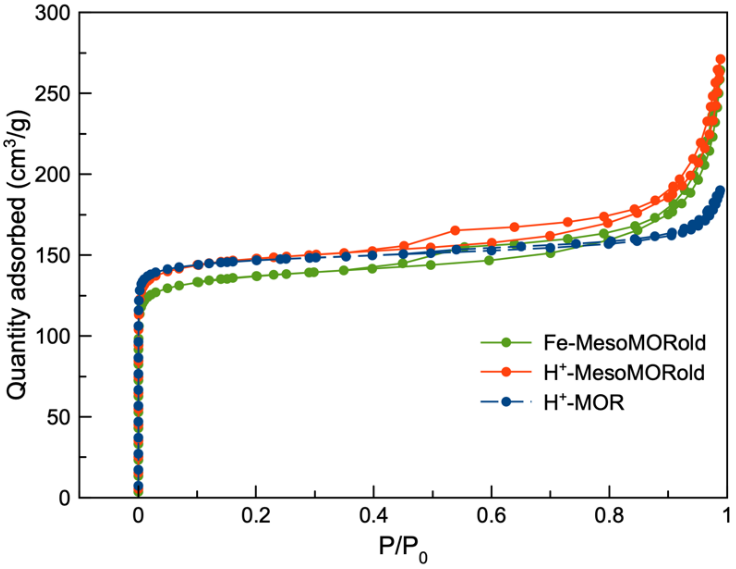

Figure 4.11 N_2 adsorption/desorption isotherms of microporous H^+-MOR and mesoporous MOR (second batch) before and after iron-exchange at -196 °C

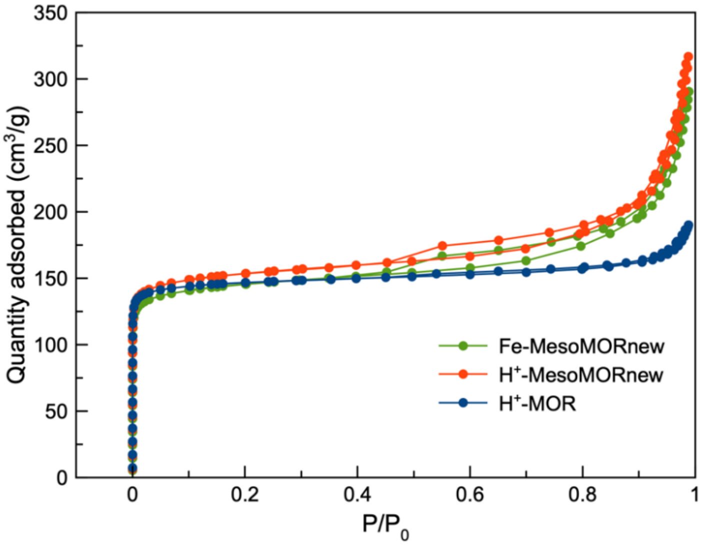

Figure 4.12 N_2 adsorption/desorption isotherms of microporous H^+-MOR and mesoporous MOR (second batch) before and after iron-exchange at -196 °C

N_2 adsorption/desorption isotherms for microporous H^+-SSZ-13 and mesoporous SSZ-13 before and after iron-exchange are given in Figure 4.13. H^+-SSZ-13 exhibited Type I adsorption isotherm due to having only micropores where mesopore addition changed the adsorption isotherm to Type IV with H4 type hysteresis loop.

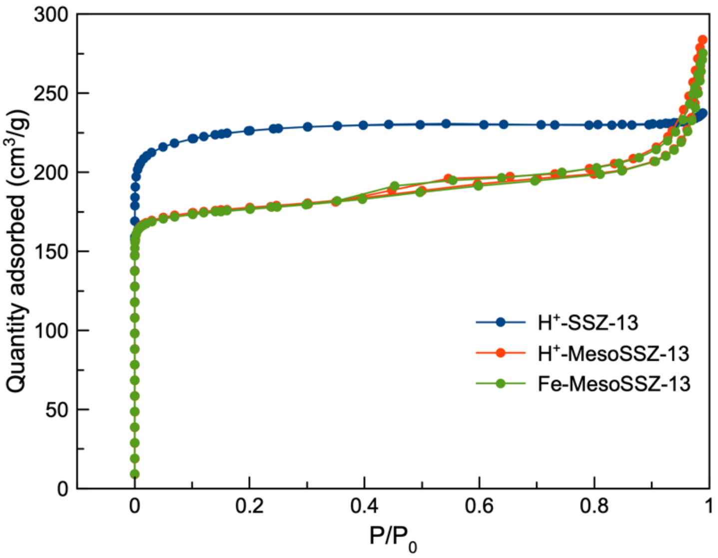

Figure 4.13 N_2 adsorption/desorption isotherms of microporous H^+-SSZ-13 and mesoporous SSZ-13 before and after iron-exchange at -196 °C

In Figure 4.14, N_2 adsorption/desorption isotherms for microporous H^+-SSZ-39 and mesoporous SSZ-39 before and after iron-exchange are given. Microporous H^+-SSZ-39 showed Type I isotherm. Mesoporous H^+- and Fe-SSZ-39 showed Type IV adsorption isotherm with H2 hysteresis loop. Since the quantity of adsorbed N_2 is lower on Fe-MesoSSZ-39 than H^+-MesoSSZ-39, it can be said that iron-exchange affected the N_2 adsorption capacity unlike other samples.

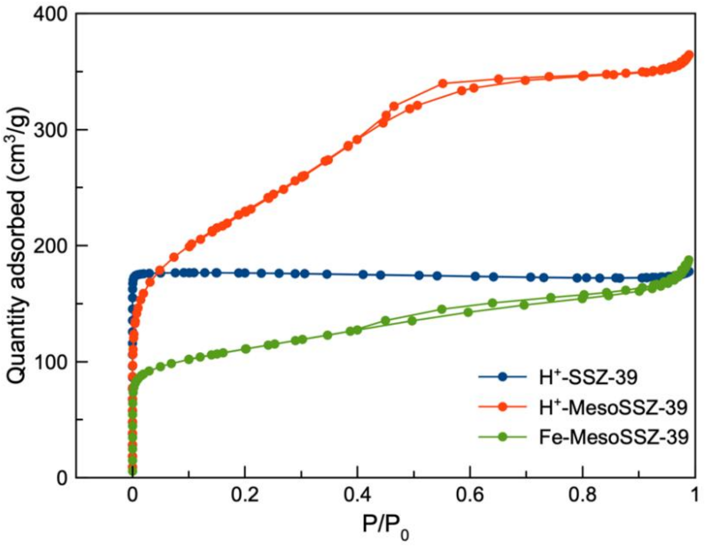

Figure 4.14 N_2 adsorption/desorption isotherms of microporous H^+-SSZ-39 and mesoporous SSZ-39 before and after iron-exchange at -196 °C

The N_2 adsorption/desorption isotherms of ZSM-5 before and after iron-exchange is given in Figure 4.15. ZSM-5 with both H^+ and Fe cations, show Type I adsorption isotherm with H4 hysteresis loop.

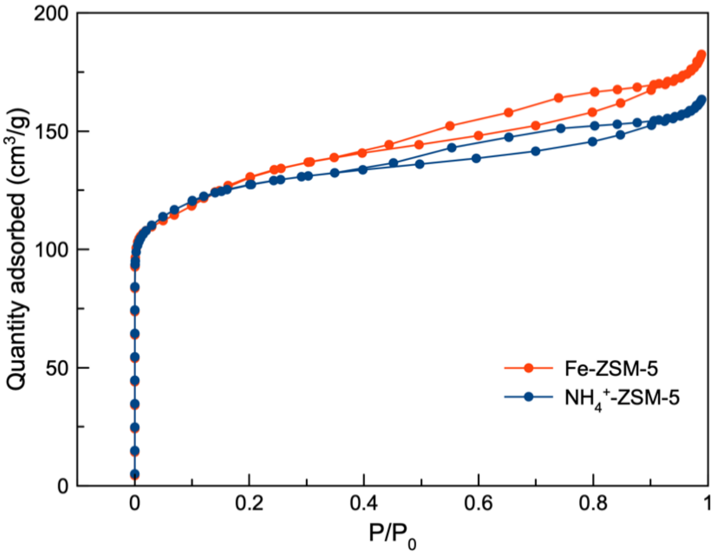

Figure 4.15 N_2 adsorption/desorption isotherms of ZSM-5 before and after iron-exchange at -196 °C

The N_2 adsorption/desorption isotherms of FER before and after iron-exchange is given in Figure 4.16. Both H^+- and Fe-FER show Type I adsorption isotherm with H4 hysteresis loop and iron-exchange did not affect the adsorption capacity of FER.

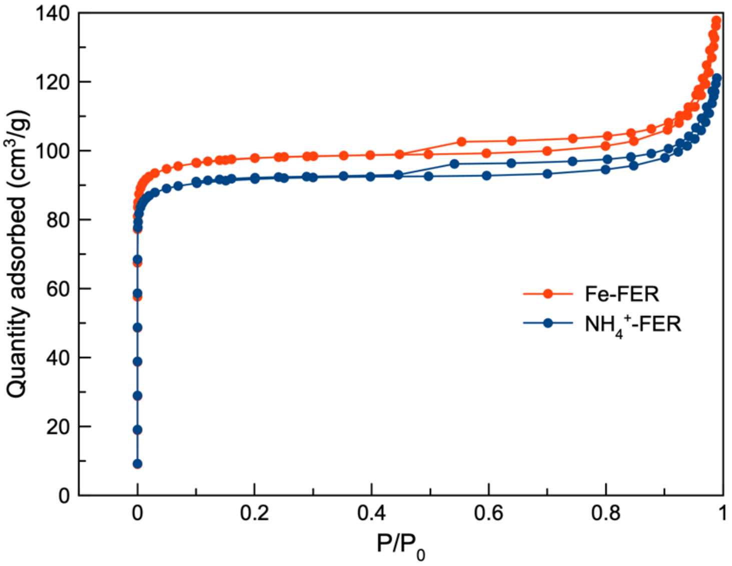

Figure 4.16 N_2 adsorption/desorption isotherms of FER before and after iron-exchange at -196 °C

4.1.4.3 Pore Size Distribution

The pore size distributions are estimated using Barrett-Joyner-Halenda (BJH) adsorption method. The BJH adsorption plots are given between 2–170 nm and given in Figures 4.17–4.19. The desired mesopore sizes between 2 to 50 nm. Wide range of pore size from 2 to 170 nm with macropores (>50 nm) additional to mesopores (2–50 nm) are observed over H^+/Fe-MesoMORold, H^+/Fe-MesoMORnew, Fe-MesoSSZ-13 and Fe-MesoSSZ-39.

Figure 4.17 shows pore size distributions of first and second batches of prepared mesoporous MOR before and after iron-exchange. It can be seen from Figure 4.17 that both batches show similar pore size distribution until 100 nm. The mesopore peaks observed at 10 and 50 nm for both Fe-MesoMORold and Fe-MesoMORnew. However, the macropores are more dominant on Fe-MesoMORold than Fe-MesoMORnew.

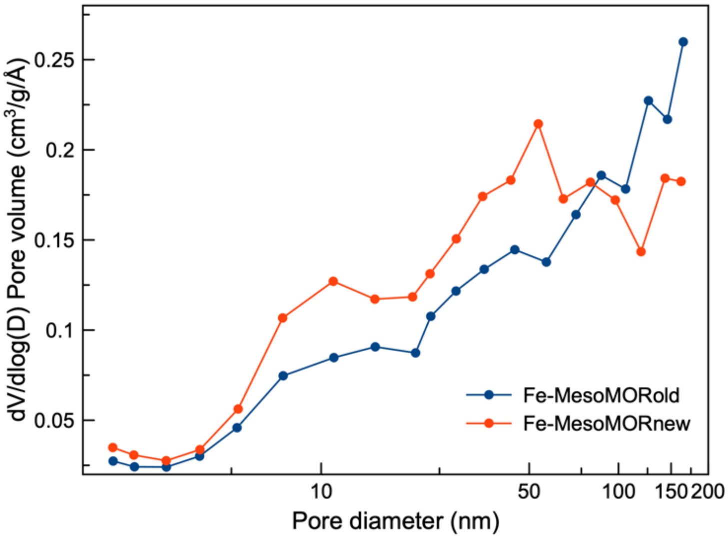

Figure 4.17 BJH adsorption branch pore size distribution of Fe-MesoMORold and Fe-MesoMORnew

Figure 4.18 shows the pore size distribution of Fe-MesoSSZ-13 and macropores in addition to small mesopores with peaking around 3 nm with broad range of mesopores between 15 to 45 nm diameter are present. The macropores are more dominant than mesopores.

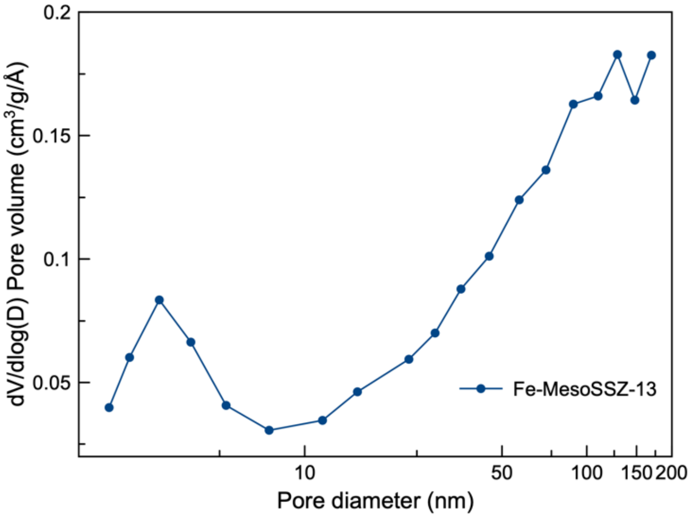

Figure 4.18 BJH adsorption branch pore size distribution of Fe-MesoSSZ-13

Pore size distribution of Fe-MesoSSZ-39 is given in Figure 4.19. The small mesopores around 3 nm are present as well as macropores even though mesopores are more dominant.

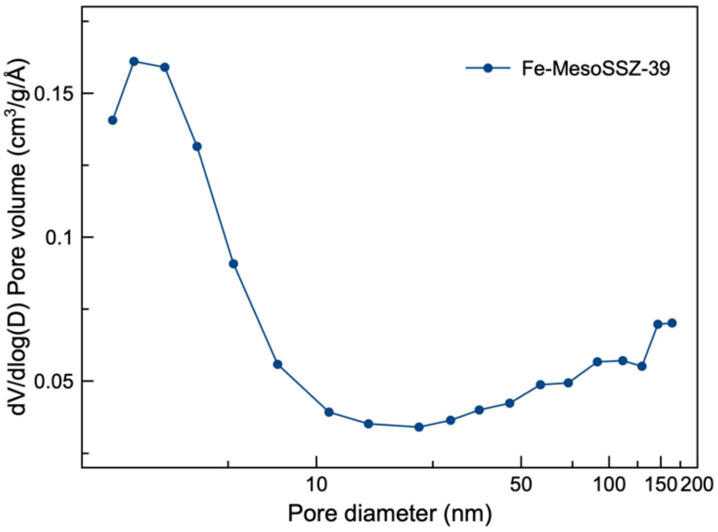

Figure 4.19 BJH adsorption branch pore size distribution of Fe-MesoSSZ-39

4.1.5 UV–Visible Spectroscopy

4.1.5.1 Hydrated Samples

The UV–Vis spectra of micro- and meso-porous MOR, SSZ-13 and SSZ-39 are given in Figure 4.20. The absorbance values obtained for Fe-MOR1 is multiplied with 50 to be comparable in Figure 4.20. As can be seen in Figure 4.20, samples show bands at 220 nm and 280 nm, which are related with isolated Fe^{3+} species in the framework and isolated extra-framework Fe^{3+} species, respectively. The Fe^{3+} cations could be substituted to the framework tetrahedral positions at the acidic Fe^{3+}-exchange conditions (pH 3). Low pH was maintained during the iron-exchange to prevent oxidation of Fe^{2+} cations (where $Fe(SO_4)$ salt is used as the iron source) and to ensure diffusion of hydrated Fe^{2+} cations into the small-pore zeolites [157]. Fe-MOR1, Fe-MesoMORnew and Fe-MesoSSZ-39 zeolites exhibited no additional peaks than extra-framework iron species. An additional peak at 350 nm observed on microporous Fe-SSZ-13 and Fe-MesoSSZ-13 is indicative of presence of Fe_xO_y clusters on zeolite surface. Large surface oxygen species (at nearly 550 nm) are also observed on Fe-SSZ-13. However, isolated extra framework Fe^{3+}cations (at 280 nm) are more significant compared to framework Fe^{3+} cations and Fe_xO_y clusters on all zeolites. The deconvoluted figures are given in Appendix D.

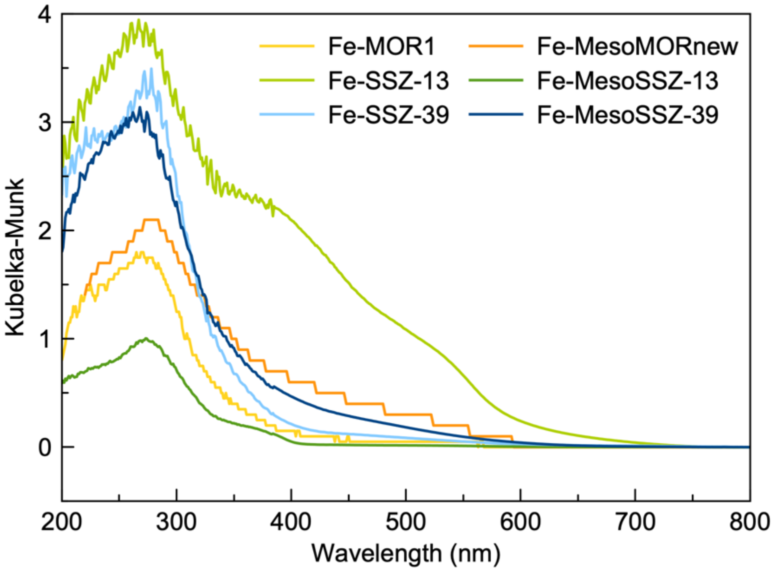

Figure 4.20 UV–vis spectra of hydrated iron-exchanged micro- and meso- MOR, SSZ-13 and SSZ-39

The UV–Vis spectra of Fe-MOR with different iron content is given in Figure 4.21 and there are no inactive iron species such as iron oxide clusters or large surface oxygen species observed over Fe-MOR0.5, Fe-MOR0.75 and Fe-MOR1, but with further increasing iron content, starting Fe/Al to 1.5 and 2, these species are formed.

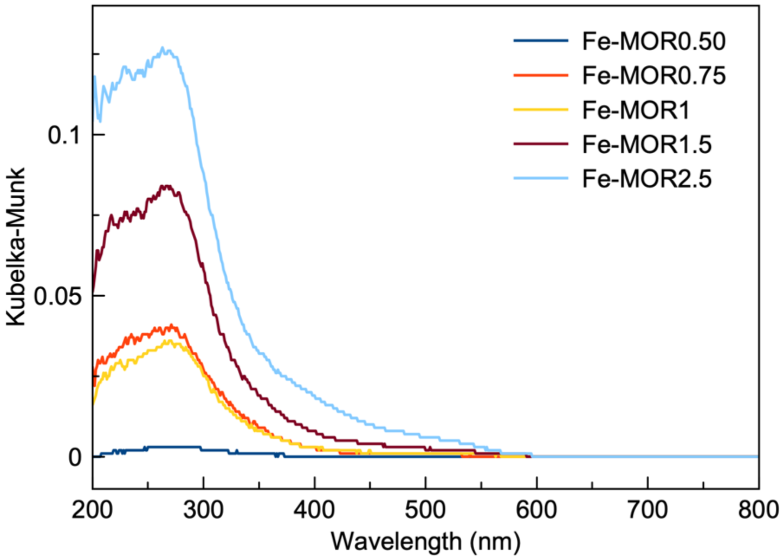

Figure 4.21 The UV–Vis spectra of Fe-MOR with different iron content

In Figure 4.22, the UV–Vis spectra of iron-exchanged micro- and mesoporous MOR are compared with FER and ZSM-5. Iron oxide clusters and larger surface oxygen species are not observed over Fe-MOR0.25 and Fe-MesoMORnew where both species are present in FER and ZSM-5.

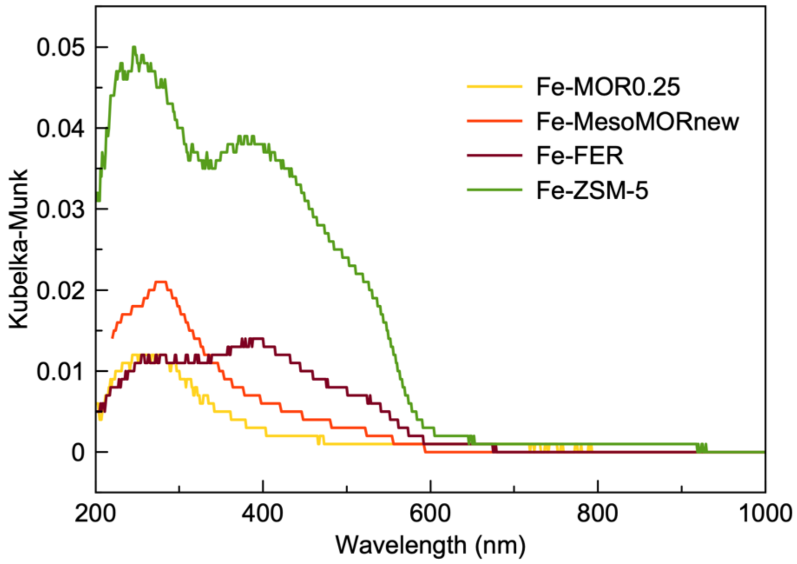

Figure 4.22 The UV–Vis spectra of iron-exchanged MOR0.25, MesoMORnew, FER and ZSM-5

4.1.5.2 N_2O and CH_4 Treated Samples

The UV–Vis spectra of iron-exchanged samples (Fe-MOR2.5, Fe-MesoMORnew, Fe-ZSM-5 and Fe-FER) before and after consecutive treatments with N_2O and CH_4 at 300 °C are given in Figure 4.23–4.26.

The UV–Vis spectra of pure Fe-MOR2.5 before and after subsequent treatments with N_2O and CH_4 are given in Figure 4.23. The peak observed over Fe-MOR2.5 before treatment that is centered around 270 nm is correlated with extra-framework iron species. Upon N_2O deactivation, a new band between 300 and 400 nm is obtained that is an indication of new iron-oxygen site formation. However, there is no change observed after CH_4 treatment unlike the study of Snyder et al. in which the peak observed over activated Fe-*BEA at 629 nm shifted to 592 nm upon N_2O activation and this peak disappeared after reaction with methane at room temperature [140]. In the study of Snyder et al. it is stated that the shift with alpha-oxygen site formation is observed over activated Fe(II)-*BEA, Fe(II)-ZSM-5 and Fe(II)-FER but not over Fe(II)-MOR since it is suggested to be located in the β sites of 6 membered rings and MOR does not exhibit β site 6 membered rings. The shift and new band formation in this study is shown to be consistent with the study of Snyder et al. since there is no change observed at 500–600 nm but new band formation is observed around 300–400 nm. This result suggests the active iron sites is different in MOR than *BEA, ZSM-5 and FER.

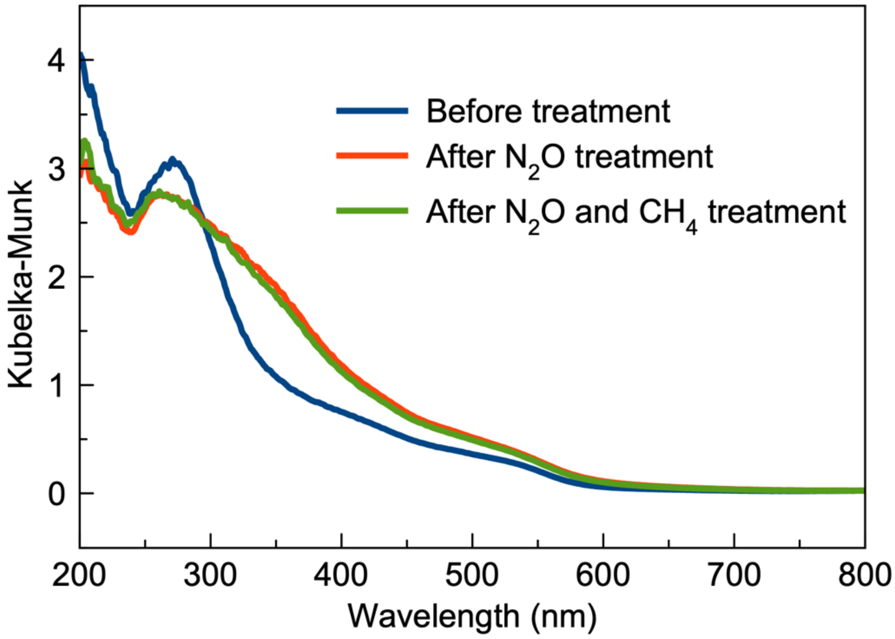

Figure 4.23 The UV–Vis spectra of N_2O and CH_4 treated pure Fe-MOR2.5

Even though a shift is observed over pure Fe-MOR2.5, no new band or species formation is observed upon N_2O treatment of Fe-MesoMORnew and $BaSO_4$ mixture, which is given in Figure 4.24. The lower iron content in Fe-MesoMORnew and $BaSO_4$ mixture might be the reason for the indifference.

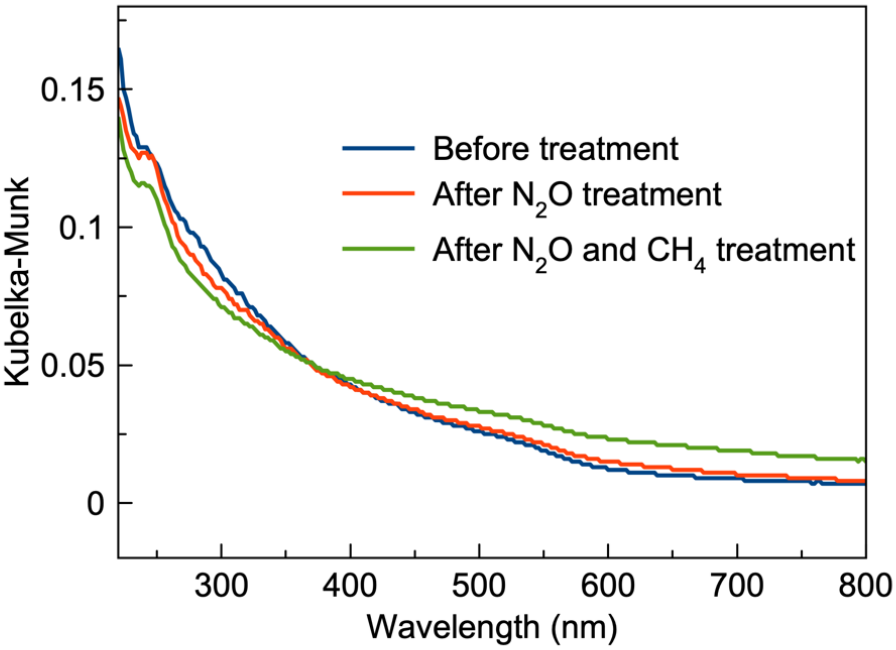

Figure 4.24 The UV–Vis spectra of N_2O and CH_4 treated Fe-MesoMORnew and $BaSO_4$ mixture

The UV–Vis spectra of Fe-FER and Fe-ZSM-5 are given in Figure 4.25 and 4.26, respectively. There are no new bands observed with N_2O treatment or disappearing of bands after methane treatment due to low iron content, since mixed with $BaSO_4$, to show visible peak changes. The reaction conditions used in this study, 300 °C reaction temperature with no pretreatment or activation procedures, are used for active sites characterization using UV–Vis. However, in the study of Snyder et al., iron-exchanged zeolites are firstly activated at high temperature in inert medium to auto reduce Fe^{3+} to Fe^{2+} [140]. Since activation procedure is not performed either during reaction or UV–Vis characterization, it might be the reason for insignificant change upon nitrous oxide or methane treatments.

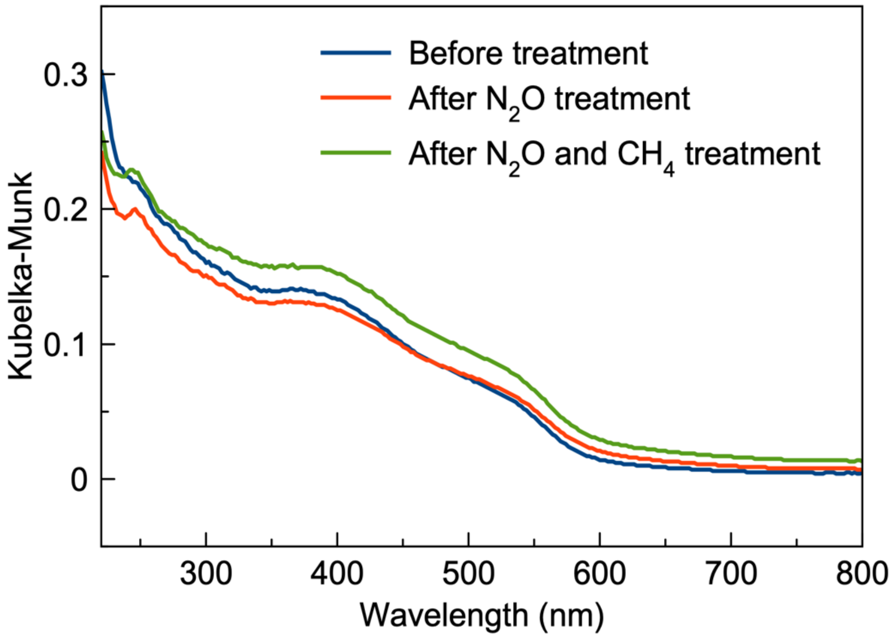

Figure 4.25 The UV–Vis spectra of N_2O and CH_4 treated Fe-FER and $BaSO_4$ mixture

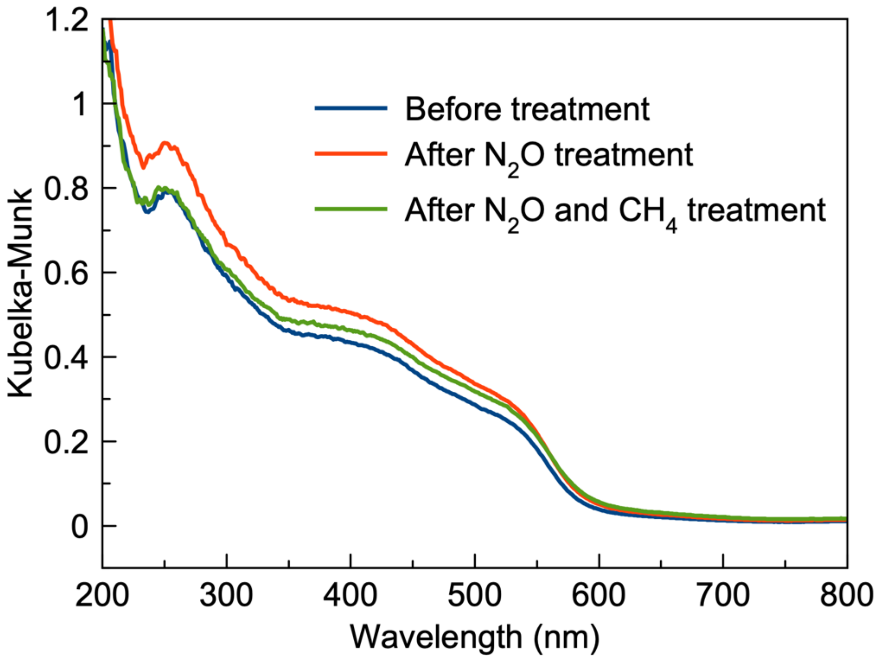

Figure 4.26 The UV–Vis spectra of N_2O and CH_4 treated Fe-ZSM-5 and $BaSO_4$ mixture (almost pure Fe-ZSM-5)

4.1.6 Magic Angle Spinning-Nucleic Magnetic Resonance

4.1.6.1 ^{27}Al MAS NMR

^{27}Al NMR is used to identify if extra-framework Al is formed during synthesis of H^{+}-SSZ-13 and Na^{+}-MesoSSZ-13 and Na^{+}-MesoMORnew that is obtained by dealumination and desilication processes applied to conventional H^{+}-MOR (Figures 4.27 and 4.28).

As can be seen from Figure 4.27, the peak intensity at 60 ppm is attributed to tetrahedrally coordinated and fully incorporated Al in the framework which is the majority of Al for both H^{+}-SSZ-13 and Na^{+}-MesoSSZ-13. Also, the tetrahedrally coordinated Al peak intensity for Na^{+}-MesoSSZ-13 is higher than H^{+}-SSZ-13. The peaks at approximately 0 ppm refer to octahedral Al indicating that extra-framework Al is present for both H^{+}-SSZ-13 and Na^{+}-MesoSSZ-13 with similar intensity values [158].

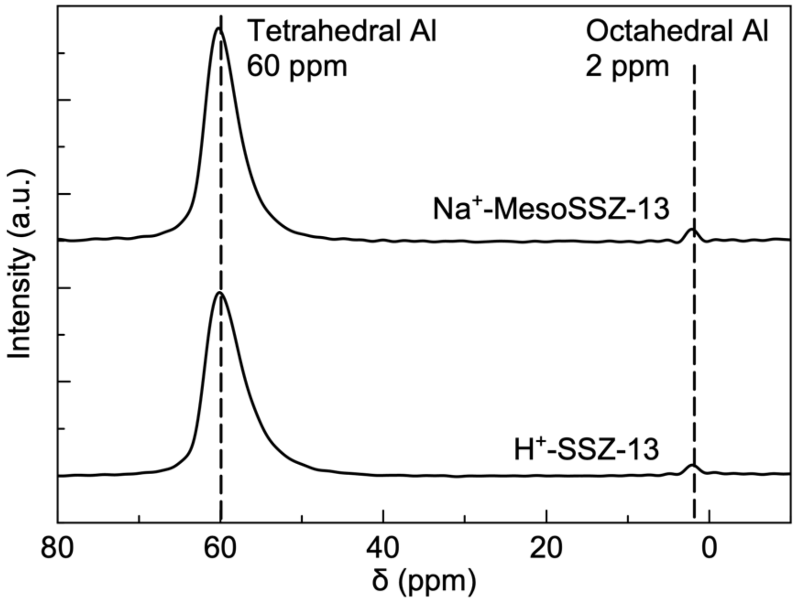

Figure 4.27 ^{27}Al MAS NMR Spectra for H^{+}-SSZ-13 and Na^{+}-MesoSSZ-13

^{27}Al MAS NMR spectra of Na^{+}-MesoMORnew is given in Figure 4.28. The resonance around 57 ppm is attributed to characteristic tetrahedral framework aluminum. There is no extra-framework Al present in this sample which would have been observed as a peak at 0 ppm referring octahedral geometry on Na^{+}-MesoMORnew [159].

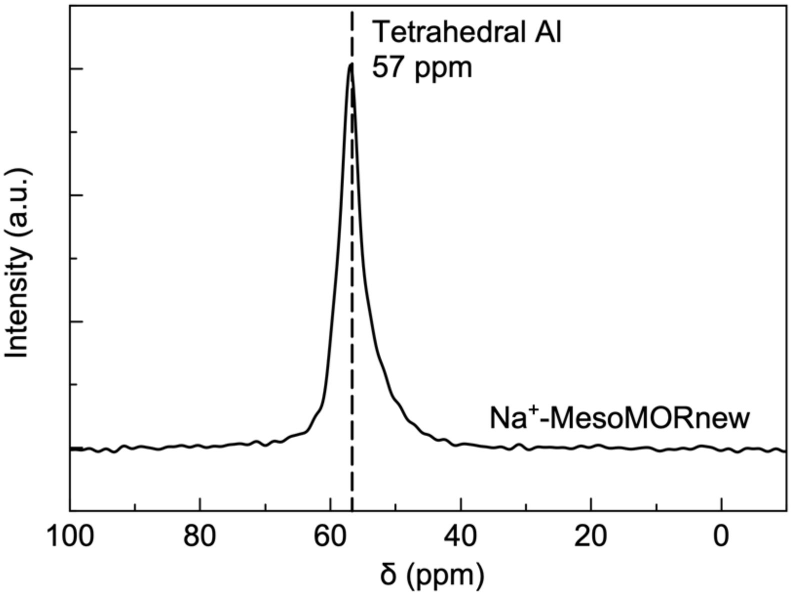

Figure 4.28 ^{27}Al MAS NMR Spectra for Na^{+}-MesoMORnew

4.1.6.2 ^{29}Si MAS NMR

^{29}Si MAS NMR spectra is used to estimate the coordination of Si with Si or Al. The deconvoluted ^{29}Si MAS NMR spectra for H^{+}-SSZ-13 and Na^{+}-MesoSSZ-13 are given in Figure 4.29. The bands observed around -113, -107, -103 and -97 ppm are attributed to Si(0Al), Si(1Al), Si(2Al) and Si(OH) defect sites, respectively.

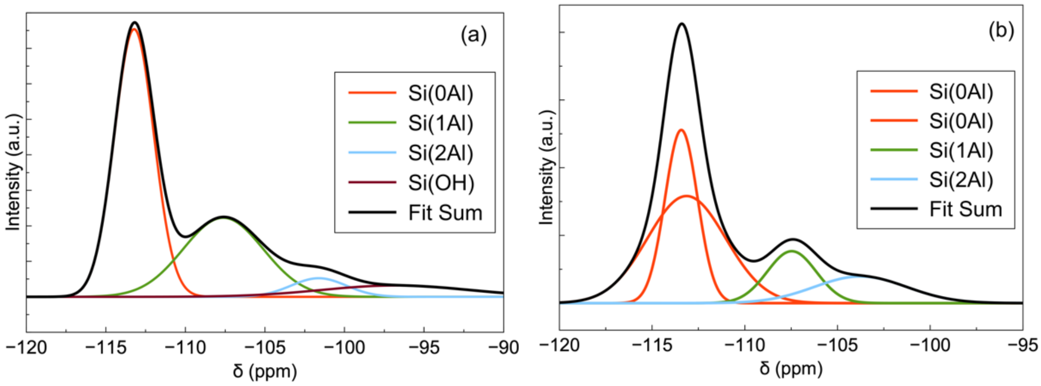

Figure 4.29 ^{29}Si MAS NMR Spectra for (a) H^+-SSZ-13 and (b) Na^+-MesoSSZ-13

The ratio of Al pairs, (Al-O-Si-O-Al), to all Al content is calculated using Equation 4.1 and increased from 25 to 51% with mesopore addition to SSZ-13.

$$Ratio\ of\ Al\ pairs\ (\%) = \frac{2*Area\ of\ Si(2Al)}{Area\ of\ Si(1Al)+2*Area\ of\ Si(2Al)} * 100 \qquad \text{(Eqn. 4.1)}$$

4.2 Methane to Methanol Reaction Results

4.2.1 Effect of Framework and Mesoporosity

Firstly, zeolites with different pore sizes and frameworks are tested at 270 °C to observe the effect of pore size and framework on methanol production rate and selectivity. Also, mesopores are added to these zeolites with different frameworks to observe the effect of shortened diffusion pathway. The methanol production rates with respect to time are given in Figure 4.30. The reaction results are summarized in Appendix E (Table E.1). To calculate methanol selectivity and reactants' conversions, first three (Fe-MesoSSZ-13 and Fe-SSZ-39) or four (Fe-MOR1, Fe-SSZ-13 and Fe-MesoSSZ-39) data obtained at 270 ºC are used due to deactivation of these zeolites. All data are taken into consideration for Fe-MesoMORnew since no deactivation is observed.

In Figure 4.30, methanol production rate and turnover frequency of methanol over time is given for different zeolites and the first three data are obtained as zero since the reaction temperature, 270 °C, is reached at 63 min. Small pore zeolites with maximum of 8-membered rings; i.e., SSZ-13 and SSZ-39 deactivated quickly in microporous form. This trend is expected since formed large methanol-to-olefin intermediate products can not exit the pores and block the micropore of small-pore zeolites [160]. With mesopore addition to Fe-SSZ-39 (having comparable Fe content), stable production of methanol is achieved over a longer catalyst lifetime, which could be due to higher coke tolerance of Fe-MesoSSZ-39 with higher surface areas. Also, with the addition of mesopores, methanol selectivity is increased from 6 to 16% on SSZ-39 (Figure 4.31). On the other hand, mesopore addition to SSZ-13 did not improve selectivity of methanol even though a slightly higher methanol TOF is achieved on Fe-MesoSSZ-13. Slightly larger crystals of MesoSSZ-13 (1–2 μm for Fe-SSZ-13 and 0.25–4 μm for Fe-MesoSSZ-13) could have resulted in higher overoxidation rates. However, higher olefin production rates, especially C_2H_4, are observed on Fe-MesoSSZ-13, which could be due to presence of more Al pairs. Use of Na^+ in the synthesis procedure of MesoSSZ-13 is expected to result in a higher concentration of Al pairs [161], (see Figure 4.29), which results in higher ethylene concentration as well as higher alkane and coke formation [162] . Fe-SSZ-39 showed higher methanol production rate than Fe-SSZ-13 even though iron content is higher on Fe-SSZ-13 as given in Table 4.1. This result might be related with the type of iron species present. Even though iron capacity is higher, iron oxide clusters on Fe-SSZ-13 are inactive sites for methane activation.

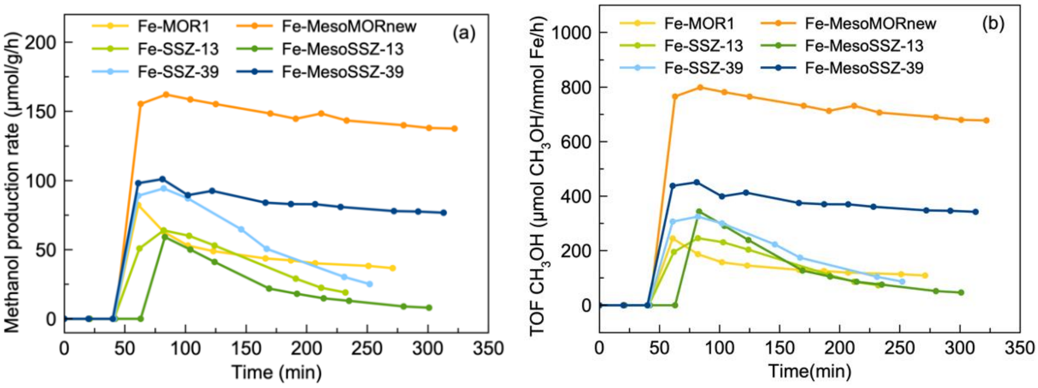

Figure 4.30 (a) Methanol production rate over time and (b) Turnover frequency of methanol over time of iron-exchanged zeolites with different framework and porosity (270 °C, 300 mg catalyst, 50 sccm, 30% CH_4, 30% N_2O, 3% H_2O (balance He))

The product distributions over micro- and mesoporous Fe-zeolites (MOR, SSZ-13, SSZ-39) are given in Figure 4.31. Ethane and propane selectivity are not included in Figure 4.31 since they are found to be lower than 1%. CO selectivity decreased consistently with mesopore addition to MOR, SSZ-13 and SSZ-39, where CO_2 selectivity increased for SSZ-13 and SSZ-39. Also, coke formation is increased with mesopore addition for all zeolites, SSZ-13, SSZ-39 and MOR. Even though reaction is carried out at comparably low temperature, 270 °C, coke formation rates ranging from 110 to 403 µmol/g/h are obtained. The coke formation has two possible routes. The first one is coke formation following the methanol-to-olefin (MTO) synthesis. As the olefin formation rates are very low at 270 °C as expected, the possibility of coke coming from MTO mechanism is low. The other possible route is the Boudouard reaction (Eqn. 4.2), an exothermic reaction in which CO is converted to CO_2 and C. According to thermodynamics, at temperatures below 327 °C, carbon formation from CO is favorable [163].

$$2CO_{(g)} \rightleftharpoons C_{(s)} + CO_{2(g)} \qquad -\Delta H^0_{rxn} = -172\ kJ/mol \qquad \text{(Eqn. 4.2)}$$

For Fe-SSZ-13 and Fe-SSZ-39 samples, CO_2 and coke formation increase with decreasing CO formation with mesopore addition at 270 °C could suggest enhanced Boudouard reaction with mesopore addition. However, for MOR sample, CO and

CO_2 decrease whereas coke selectivity increases with mesopores that might be related to coke formation from MTO route, which increases with the defect sites created during dealumination or desilication processes [164]. Even though coke selectivity increases from 18 to 24% on Fe-MesoMORnew, the most significant change is observed in CO selectivity, from 71 to 38%, which increased methanol selectivity seven times, from 4 to 29%.

The highest selectivity for light olefins, ethylene and propylene, are observed on iron-exchanged SSZ-13, SSZ-39 and MOR in descending order. This result is consistent with literature, zeolites having 8-membered rings, were shown to be more prone to higher selectivity of light olefins [165]. The selectivity of ethylene and propylene are increased with mesopore addition in each zeolite, but most significant change is obtained for Fe-SSZ-13, in which total selectivity is doubled due to the increased Al pairs. The decrease in CO formation rate increased methanol selectivity for MOR and SSZ-39 significantly, from 4 to 29% and from 6 to 16%. But increase in ethylene and propylene formation prevented increase in methanol selectivity for Fe-SSZ-13, where methanol selectivity decreased from 18 to 14%. Dimethyl ether production increased with mesopore addition to Fe-MOR and Fe-SSZ-39. Moreover, ethylene selectivity is halved in MOR due to mesopores whereas it is increased for SSZ-13 and SSZ-39. Propylene production increased with mesopores in all cases. Butane and butene molecules are formed over iron-exchanged micro- and meso-SZZ-13 and SSZ-39, whereas C_4 products are not observed on micro- or meso-MOR.

Microporous Fe-MOR1 and mesoporous Fe-MesoMORnew, which is a large pore zeolite, are also compared. Slight deactivation is also observed on both catalysts. However, mesopore addition to MOR zeolite enhanced methanol production rate over two times even though iron-concentration is lower on Fe-MesoMORnew. As can be seen from Figure 4.31, overoxidation products, CO (1177 to 192 μmol/g/h) and CO_2 (92 to 18 μmol/g/h) decreased dramatically with mesopore addition which increased methanol selectivity four times from 4% to 29%.

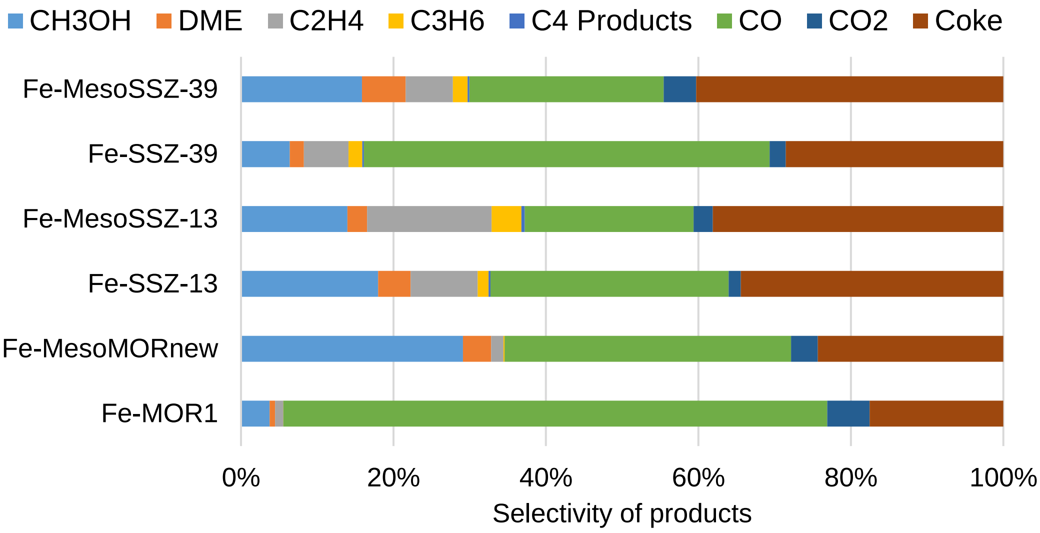

Figure 4.31 Product distribution over iron-exchanged zeolites (270 °C, 300 mg catalyst, 50 sccm, 30% CH_4, 30% N_2O, 3% H_2O (balance He))

The highest methanol production rate of 148 µmol/g/h, most stable methanol production and minimum olefin production with no C_4 products are obtained on Fe-MesoMORnew. So, it is chosen as the optimum zeolite for further optimization. The main product causing lower methanol selectivity is CO. Thus, solutions for CO minimization should be investigated like iron content, mesopore addition, feed composition, water vapor addition in feed and Brønsted acidity.

4.2.2 Effect of Iron Content

The effect of iron content on methanol selectivity is studied over microporous MOR. Conventional NH_4^+-MOR is tested, and no activity is observed which emphasizes the significance of iron species (see Table E.2). As the Fe content increases, CO and CO_2 formation rates increase due to higher concentration of active sites in a zeolite crystal. Hammond et al. studied the effect of iron content in partial oxidation of methane to methanol using H_2O_2 oxidant over Fe-ZSM-5 and showed that while methanol formation rate is increased with increase in iron content, turnover frequency of methanol is halved due to presence of spectator iron species [113].

Methanol and TOF methanol time on streams over time of MOR with different iron content are given in Figure 4.32-a and Figure 4.32-b. The detailed reaction results are given in Appendix E (Table E.2). During average formation rate calculations, the data obtained between 170 to 230 minutes are used for all zeolites due to stability. As can be seen from Figure 4.32, deactivation is observed over Fe-MOR2.5. However, for other iron contents stable production is obtained after peak methanol formation. Fe-MOR0.75 showed the highest methanol formation rate, 333 μmol/g/h, and TOF methanol, 1044 μmol CH_3OH/mmol Fe/h, where lowest TOF methanol, 389 μmol CH_3OH/mmol Fe/h, is obtained over Fe-MOR2.5 which has the highest iron content of 468 mmol Fe/g cat.

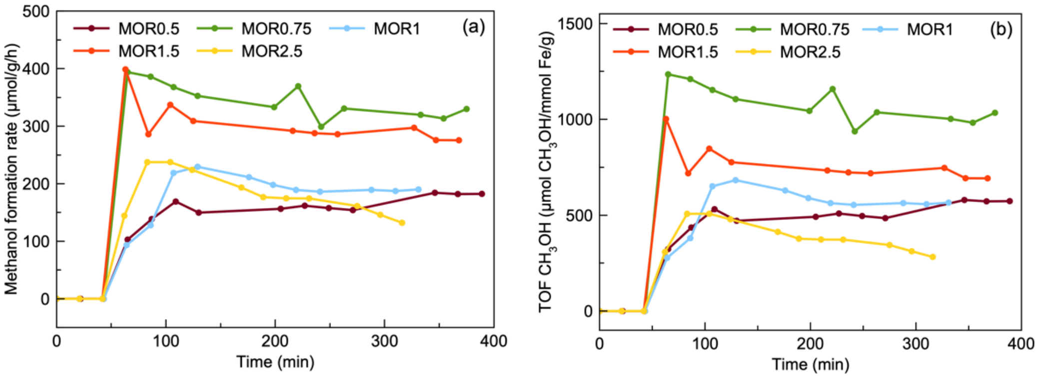

Figure 4.32 (a) Methanol time on stream and b) TOF CH_3OH with respect to time over Fe-MOR samples with different iron content (300 ºC, 300 mg catalyst, 100 sccm, 30% CH_4, 10% N_2O, 11–18% H_2O (balance He))

The product distribution over Fe-MOR with different iron contents is given in Figure 4.33. In the figure below, selectivity of C_2H_6 and C_3H_8 are not included since the total selectivity of these products are below 0.3%. As can be seen from Figure 4.33, the highest overoxidation product selectivity of CO and CO_2 are obtained at the highest iron content and lowest iron content, respectively. The formation rate of dimethyl ether and ethylene have not been changed significantly with changing Fe content in the range of 0.319–0.468 mmol Fe/g cat as expected as MTO mechanism is affected by concentration and type of acid sites. Even though methanol selectivity or TOF methanol does not decrease gradually as iron content is increased, Fe-

MOR0.75 and Fe-MOR1.5 whose iron contents are 0.319 and 0.398 mmol Fe/g, respectively, showed higher TOF and selectivity of methanol. When the UV–Vis spectra of Fe-MOR0.75 and Fe-MOR1.5 are compared, there are no inactive iron oxide species observed on both zeolites. Thus, as a combination of higher methanol formation rate and TOF, Figure 4.32, and methanol selectivity of 25%, Figure 4.33, it can be said that the optimum iron content is 0.319 mmol Fe/g cat.

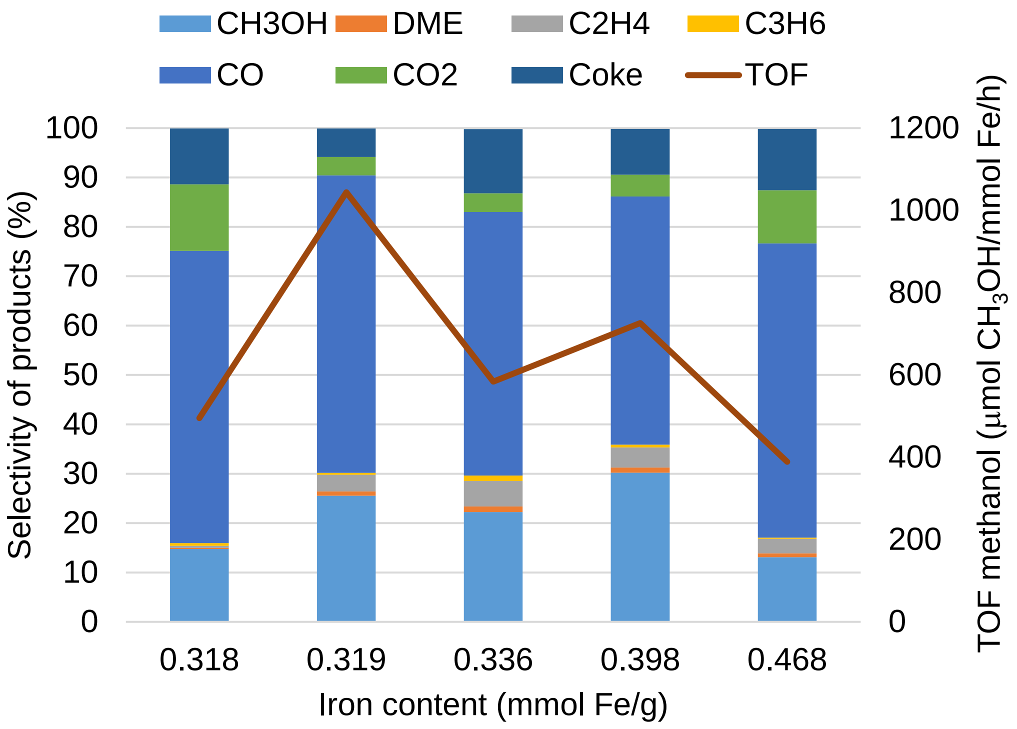

Figure 4.33 Product distribution and TOF CH_3OH with respect to iron content over Fe-MOR with different iron content (300 ºC, 300 mg catalyst, 100 sccm, 30% CH_4, 10% N_2O, 11–18% H_2O (balance He))

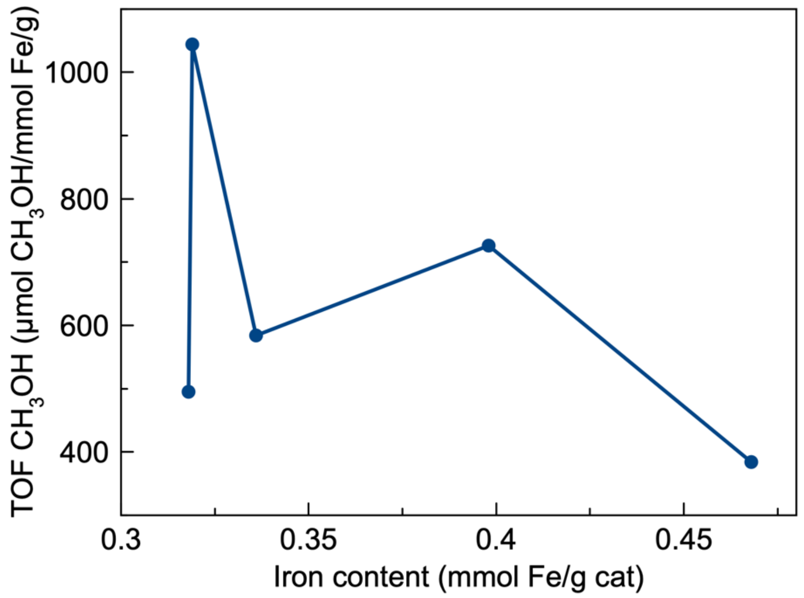

Figure 4.34 TOF methanol with respect to iron content over Fe-MOR with different iron content (300 ºC, 300 mg catalyst, 100 sccm, 30% CH_4, 10% N_2O, 11–18% H_2O (balance He))

4.2.3 Optimization on Fe-MesoMOR

Iron-exchanged mesoporous MOR is chosen to be further optimized due to its ability to produce methanol steadily and more selectively compared to SSZ-13 and SSZ-39. The compositions of reactants, methane, nitrous oxide, and water vapor is varied to achieve the highest methanol selectivity and formation rate with a prolonged catalyst lifetime.

4.2.3.1 Optimization of Methane

The methane optimization is performed by changing methane composition in feed from 20 to 40% over Fe-MesoMORnew. The detailed reaction results can be found in Appendix E (Table E.3). Methanol formation rates with respect to time at different CH_4 compositions in feed are given in Figure 4.35. Deactivation is not observed at any methane concentration in feed.

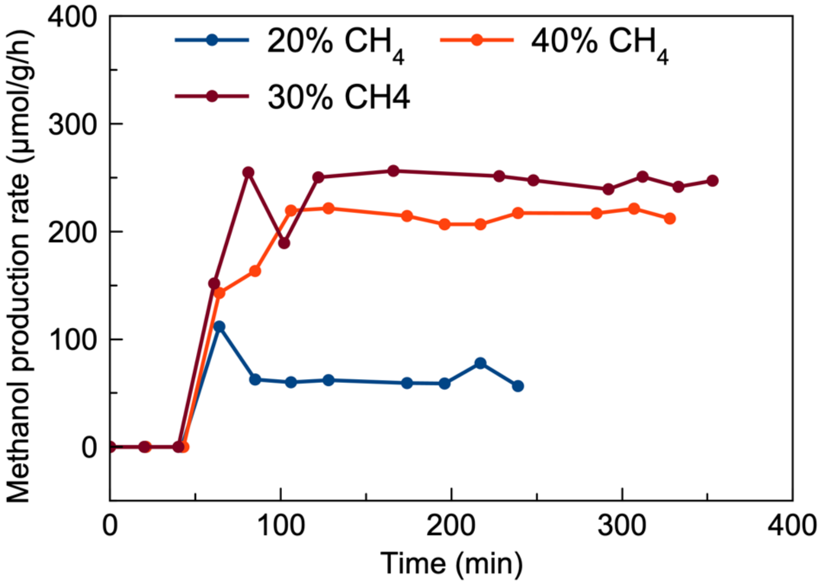

Figure 4.35 Methanol time on stream over Fe-MesoMORnew (300 ºC, 300 mg catalyst, 100 sccm, 20–40% CH_4, 10% N_2O, 11–15% H_2O (balance He))

Selectivity of products are given in Figure 4.36 with respect to different methane compositions in feed. Selectivity of C_2H_6 and C_3H_8 are not included in Figure 4.36 since at 30% and 40% the total selectivity of these products is below 0.3% while at 20% it is 1.7%. This result suggests secondary reactions are more dominant at 20% CH_4 composition in feed which resulted with lowest methanol selectivity. The highest coke selectivity of 42% is obtained at low methane composition, 20%. As methane composition is increased to 30%, coke selectivity is decreased to 1%. On the other hand, with increasing methane composition in feed is increased from 20 to 30%, the selectivity of CO and DME increased from 20 to 50% and 0.8 to 4%, respectively. Due to decreased CO selectivity of 1.4 times, methanol selectivity is increased 1.3 times when methane composition is increased from 30 to 40%. However, higher methanol formation rate is obtained at 30% methane composition as can be seen from Figure 4.36 and lowest coke formation and selectivity is obtained at 30%. Thus, the optimum methane composition in feed is chosen as 30%.

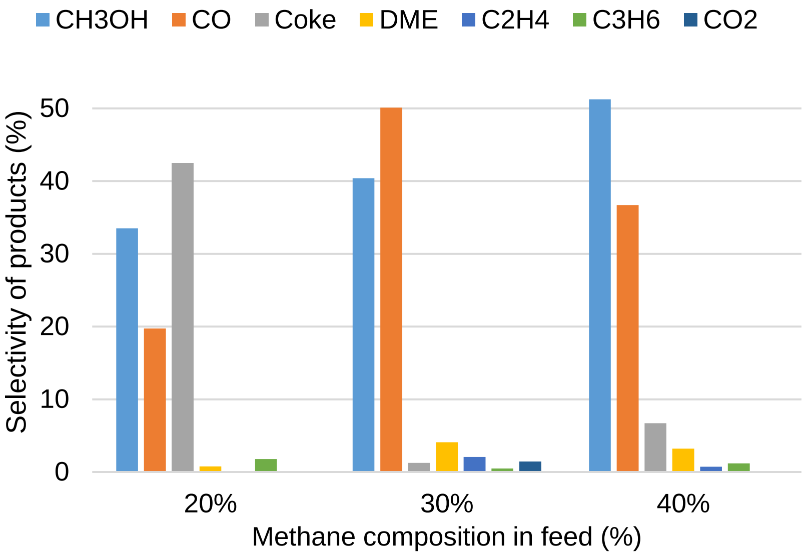

Figure 4.36 Products distribution over Fe-MesoMORnew (300 °C, 300 mg catalyst, 100 sccm, 20–40% CH_4, 10% N_2O, 11–15% H_2O (balance He))

4.2.3.2 Optimization of Nitrous Oxide

It is known that the higher amount of nitrous oxide in feed improves formation of active sites but also accelerate the secondary reactions [94]. This optimization study is done on Fe-MesoMORold. N_2O percentage in feed is changed from 10 to 30% to investigate the effect of oxidant and the reactants conversions (both reactants' conversions are multiplied with ten to be comparable with methanol selectivity), turnover frequency and selectivity of methanol are given in Figure 4.37. Also, the product distributions are given in Figure 4.38. The detailed reaction results can be found in Appendix E (Table E.4). In Figure 4.37, methane and nitrous oxide conversions are multiplied with 10 to be able to compare with methanol selectivity. As can be seen from Figure 4.37, as oxidant in feed is increased, turnover frequency of methanol increases slightly. However, converted methane is mostly overoxidized to CO and CO_2 or turned to coke which lowered methanol selectivity from 31 to 20%

(see Figure 4.38) with an increase in N_2O% in feed from 10 to 30%. Considering the higher methanol selectivity, 10% N_2O in feed is chosen as the optimum condition in the other reaction tests.

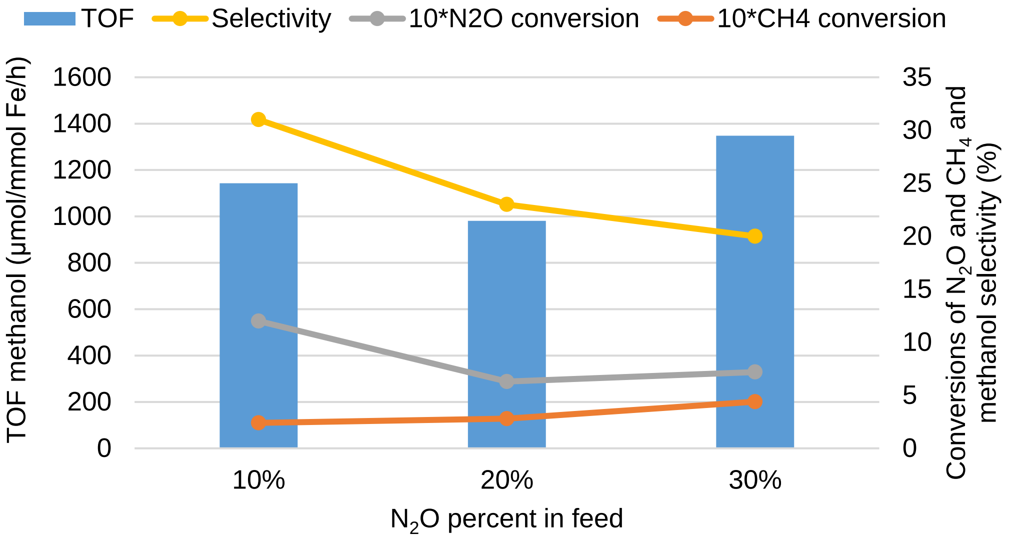

Figure 4.37 Turnover frequency and selectivity of methanol (yellow), and conversions of methane (orange) and nitrous oxide (grey) with respect to N_2O% in feed over Fe-MesoMORold (300 °C, 300 mg catalyst, 100 sccm, 30% CH_4, 10–30% N_2O, 8% H_2O (balance He))

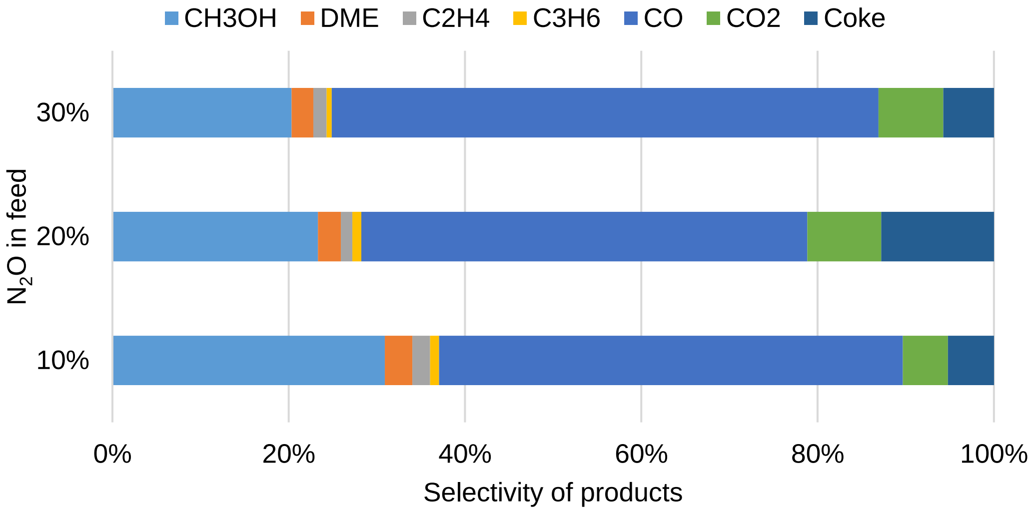

Figure 4.38 Selectivity of products over Fe-MesoMORold (300 °C, 300 mg catalyst, 100 sccm, 30% CH_4, 10–30% N_2O, 8% H_2O (balance He))

4.2.4 Effect of Water Vapor

Water vapor addition in the feed has a known effect of increasing methanol selectivity [127], [130], [132]. Water vapor addition suppresses overoxidation and increase methanol selectivity eventually. Methanol is not easily desorbed from the surface, for stepwise processes water vapor is used for desorption of formed methanol from the active sites. Thus, increase in methanol selectivity is expected if water vapor helps methanol desorption and prevent overoxidation. Presence of water vapor is also known to decrease the coke formation [127], [130], [132], which would result in an increased catalyst lifetime.

The effect of water vapor on methanol selectivity is investigated on Fe-MesoMORold (Si/Al=30, Fe/Al=0.30). The detailed reaction results are given in Appendix E (Table E.5). During average formation rate calculations, first four data obtained at 300 ºC are used due to the slight deactivation observed over Fe-MesoMORold with 3% water vapor in feed. For other cases, all the reaction data are taken into calculations since no deactivation is observed with increasing water vapor in feed.

In Figure 4.39, it is seen Fe-MesoMORold is deactivated at 300 ºC with 3% water vapor in feed, but with increasing water vapor only to 8%, the production is stabilized. The increase in water vapor from 3 to 8% did not only affect the stability but also enhanced the methanol production rate from an average value of 137 to 187 μmol/g/h. Further increase in the water vapor concentration to 12 and 15% did not promote the methanol formation rate even though it is reported in literature that methanol production is also enhanced for Fe-*BEA and Fe-Cu-*BEA [132]. However, the increased methanol selectivity from 20 to 50% due to suppression of secondary reactions, mostly CO, CO_2 and coke formation, with increasing water vapor in feed is consistent with literature [127], [130], [132].

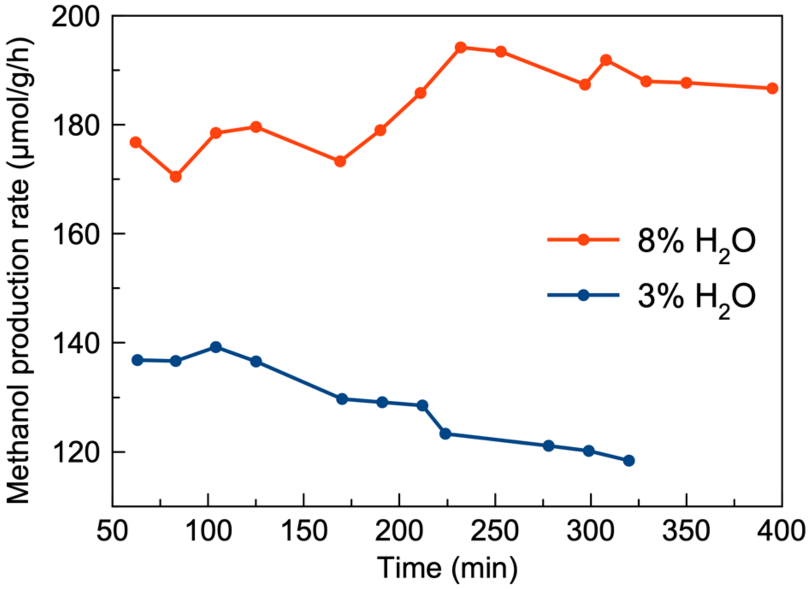

Figure 4.39 Methanol production rate over time over Fe-MesoMORold (300 °C, 300 mg catalyst, 100 sccm, 30% CH_4, 10% N_2O, 3–8% H_2O (balance He))

According to Figure 4.40, as water vapor in feed increases, conversions of both methane and nitrous oxide decrease due to expected decrease in Fe-oxygen active site concentrations. The water vapor is suggested to competitively adsorb on Brønsted acid sites which lowers the conversions of methane and nitrous oxide [130].

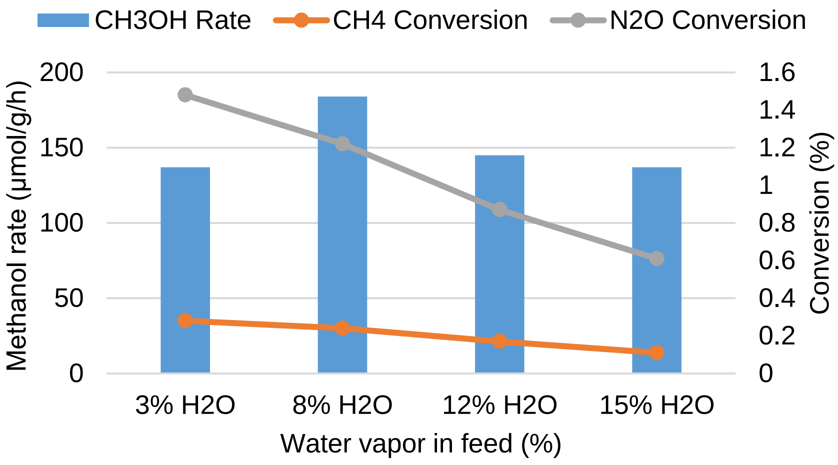

Figure 4.40 Methane and nitrous oxide conversion with respect to water vapor in feed over Fe-MesoMORold (300 °C, 300 mg catalyst, 100 sccm, 30% CH_4, 10% N_2O, 3–8% H_2O (balance He))

In Figure 4.41, only alkene selectivity is included for C_2 and C_3 products since the selectivity of ethane and propane are lower than 1%. As can be understood from Figure 4.41, addition of water vapor affects formation of secondary products, mostly CO, CO_2 and coke. Ethylene and dimethyl ether production rates are less than 15 and 10 µmol/g/h, respectively. Still, DME rate decreased 20% with 15% water vapor addition which might be related with the LeChatelier's principle in methanol to dimethyl reaction given in Equation 4.3. As water vapor in medium increases, the reverse reaction is favored towards methanol.

$$2CH_3OH \leftrightarrow CH_3OCH_3 + H_2O \tag{Eqn. 4.3}$$

Increasing water vapor ratio in the feed decreases DME, C_2H_4, CO, CO_2 and coke formation significantly, where C_3H_6 selectivity increases. Overall, increasing water vapor from 3 to 15% resulted with an increase in methanol selectivity from 20 to 50% as can be seen from Figure 4.42.

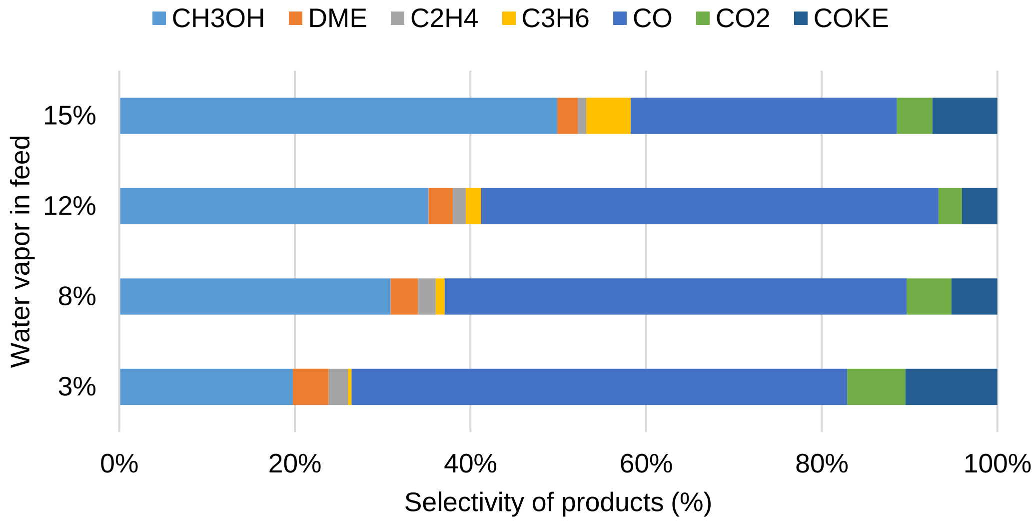

Figure 4.41 Product distribution versus water vapor in feed over Fe-MesoMORold (300 °C, 300 mg catalyst, 100 sccm, 30% CH_4, 10% N_2O, 3–15% H_2O (balance He))

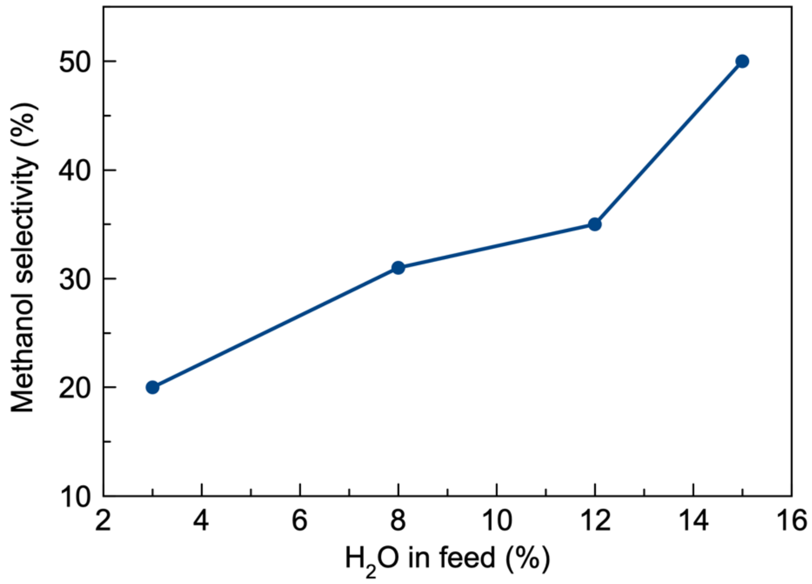

Figure 4.42 Methanol selectivity with respect to water vapor in feed over Fe-MesoMORold (300 °C, 300 mg catalyst, 100 sccm, 30% CH_4, 10% N_2O, 3–15% H_2O (balance He))

4.2.5 Effect of Mesopores on MOR

In order to observe the mesopore effect on methanol selectivity, micro- and meso-Mordenite samples with similar Fe contents are compared since Si/Al ratios changed after dealumination and desilication processes. Fe-MesoMORnew sample has 0.203 mmol Fe/g cat whereas the lowest and most compatible ratio observed on microporous MOR is 0.280 mmol Fe/g cat denoted as Fe-MOR0.25. Fe-MOR0.25 and Fe-MesoMORnew were tested for partial methane oxidation at 300, 320 and 340 °C using a feed flow having a molar composition of 30% CH_4, 10% N_2O, 21-23% H_2O (Figure 4.43). The detailed reaction results are given in Appendix E (Table E.6). Due to severe deactivation, only the first two data obtained at 340 ºC are considered for average rate calculations over Fe-MOR0.25. The data obtained at 200–250 minutes are used for average rate calculations for Fe-MesoMORnew at all three temperatures.

At 300 °C steady-state production of methanol without deactivation is observed on both zeolites. However, as temperature increases to 320 °C, deactivation due to coke formation is observed on Fe-MOR0.25, whereas Fe-MesoMORnew produces methanol steadily with an average of 795 µmol/g/h. As reaction temperature is elevated to 340 °C, since methanol to olefins pathway is accelerated [166], deactivation is observed on both Fe-MOR0.25 and Fe-MesoMORnew. However, despite the deactivation, the methanol formation rate on Fe-MesoMORnew was observed as two times of the rate observed on Fe-MOR0.25. During the deactivation of both catalysts, increase in CO and CO_2 formation rates were observed in the gas phase in addition to the increased coke formation (see Figure 4.44).

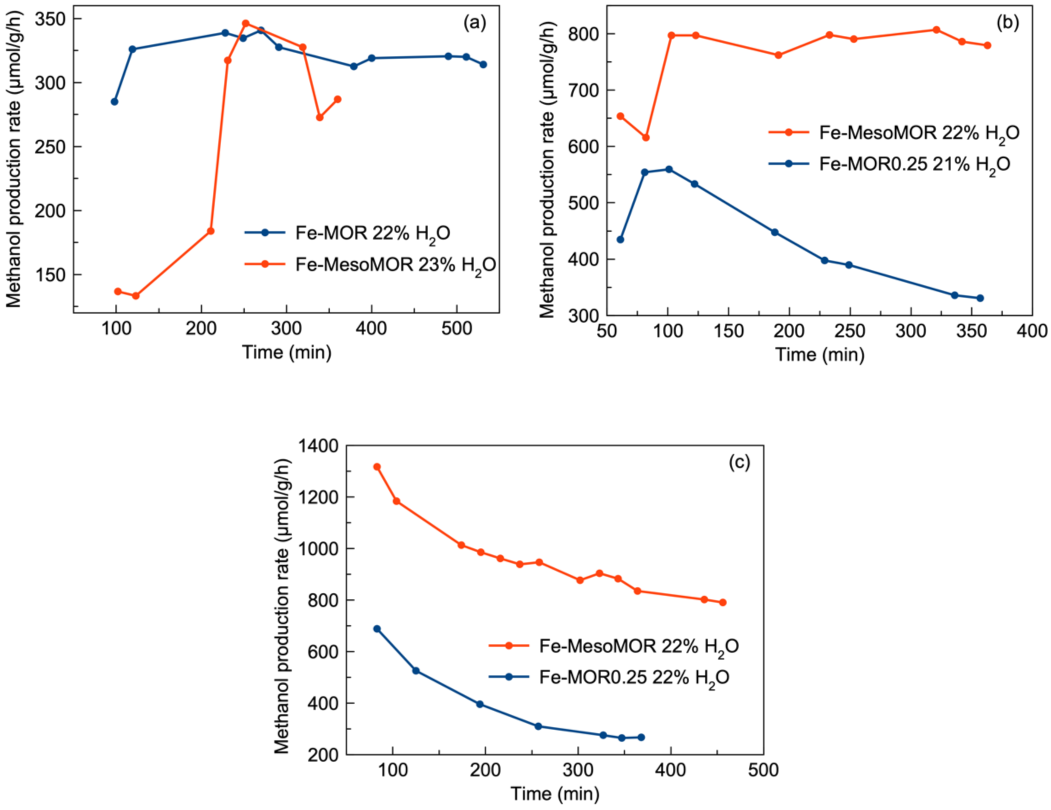

Figure 4.43 Methanol production rate over iron-exchanged micro- and meso- MOR (300 mg catalyst, 100 sccm, 30% CH_4, 10% N_2O, 21–23% H_2O (balance He)) (a) T=300 °C, (b) T=320 °C and (c) T=340 °C

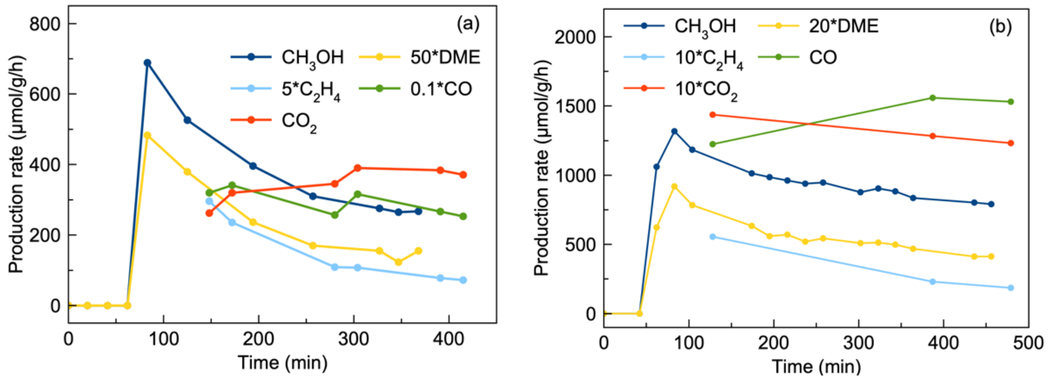

Figure 4.44 Products time on stream over (a) Fe-MOR0.25 (340 °C, 300 mg catalyst, 100 sccm, 30% CH_4, 10% N_2O, 22% H_2O (balance He)) and (b) Fe-MesoMORnew (340 °C, 300 mg catalyst, 100 sccm, 30% CH_4, 10% N_2O, 22% H_2O (balance He))

Figure 4.45 gives the product selectivity of Fe-MOR0.25 and Fe-MesoMORnew at three different temperatures. The average of the first three/four reaction rate data is used in Figure 4.43 due to significant deactivation. Also, selectivity of ethane, propane and propylene are not included since total of these products' selectivity is lower than 1.5% and cannot be distinguished on the figure. The detailed production rates could be seen in Appendix E, Table E.3. At all three temperatures, Fe-MesoMORnew resulted in much lower CO and CO_2 formation rates when compared to microporous zeolite, i.e., Fe-MOR0.25, which resulted in higher methanol selectivity values (39% vs. 52% at 300 °C). Added intracrystalline mesopores shorten the diffusion pathway and prevent secondary oxidation reaction on Fe-oxygen active centers inside the zeolite crystal for MOR hat has 1-D pore structure. In MTO pathway, formed methanol is dehydrated to dimethyl ether then light olefins like ethylene and propylene then higher olefins then paraffins, aromatics and eventually coke that causes catalyst deactivation. At 300 and 320 °C, lower ethylene and coke selectivity is obtained on Fe-MesoMORnew when compared to FeMOR0.25, which could be also related to faster exit of methanol from the zeolite crystals with suppressed interaction with the surface acid sites of the zeolites. The kinetics of MTO reaction is known to become significant at temperatures above 350 °C, which is apparent for both Fe-MOR0.25 and Fe-MesoMORnew at 340 °C. But at 340 °C, all MTO products including dimethyl ether, ethylene and coke are increased with mesopore addition. This could be due to pronounced effect of defect sites on MesoMORnew, created during dealumination, that resulted in increased ethylene and coke formation [167], [168]. There is no extra-framework Al detected using ^{27}Al NMR (see Figure 4.28), however there might be other defect sites that could be formed during subsequent dealumination, desilication and dealumination steps for mesopore addition to MOR. Despite slightly increased MTO activity on Fe-MesoMORnew, methanol turnover frequency values increased significantly with temperature when compared to Fe-MOR0.25 due to suppressed CO and CO_2 formation. At 320 °C, TOF of methanol observed on Fe-MesoMORnew was two times of that observed on Fe-MOR0.25 and further increase of the reaction temperature to 340 °C resulted in a TOF value that is more than two times of that on Fe-MOR0.25 (see Appendix E, Table E.6).

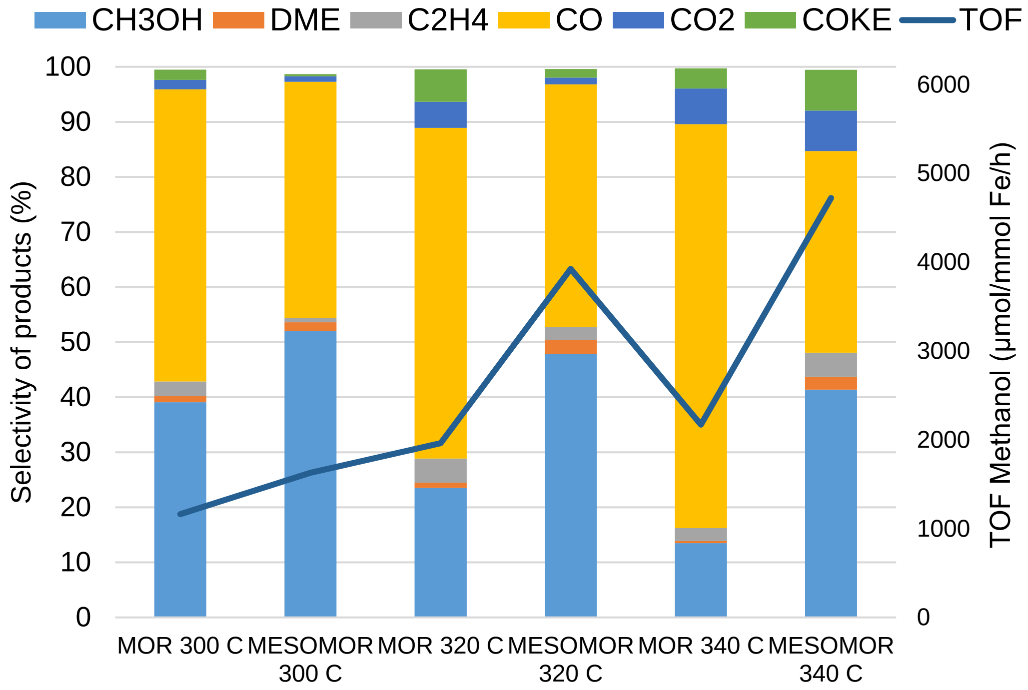

Figure 4.45 Product distribution and turnover frequency of methanol on iron-exchanged Micro- and Meso- MOR at different temperatures (300–340 °C, 300 mg catalyst, 100 sccm, 30% CH_4, 10% N_2O, 21-23% H_2O (balance He))

The mesopore effect is also investigated at low water vapor content in feed (11%) with Fe-MOR0.25 and Fe-MesoMORnew. The detailed reaction results are given in Appendix E, Table E.3. While reporting average formation rate of products, first three data obtained at 300 °C are used for Fe-MOR0.25 due to deactivation, where all the data are considered for Fe-MesoMORnew. Methanol formation rate over time for Fe-MOR0.25 and Fe-MesoMORnew are given in Figure 4.46. As can be seen from Figure 4.46, Fe-MOR0.25 catalyst is deactivated due to severe coke formation. On the other hand, Fe-MesoMORnew did not deactivate and was able to produce methanol in steady state at 300 °C for 12 hours.

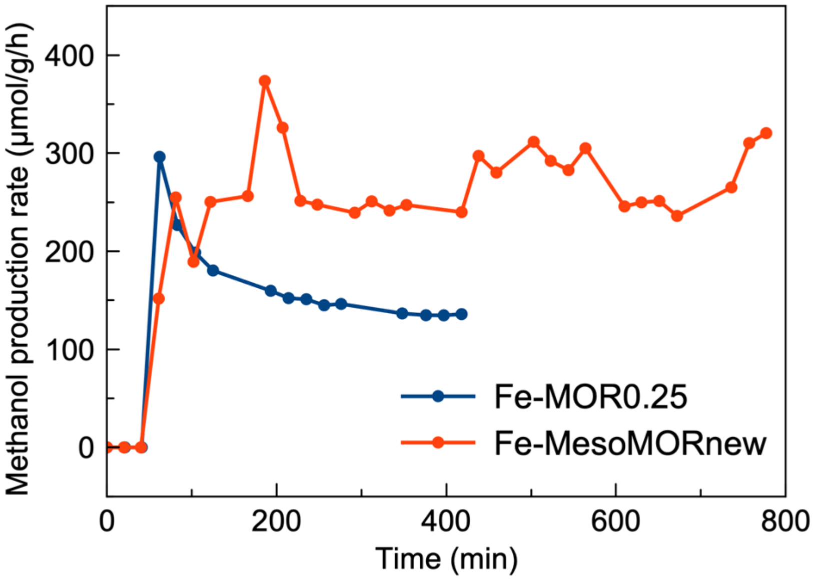

Figure 4.46 Methanol production rate over Fe-MOR0.25 and Fe-MesoMORnew (300 °C, 300 mg catalyst, 100 sccm, 30% CH_4, 10% N_2O, 11% H_2O (balance He))

The product distribution is given in Figure 4.47. The selectivity of C_2H_6 and C_3 products are not included in the Figure 4.47 since total of these products' selectivity is less than 0.7%. The sum of selectivity of CO and CO_2 is 98.3% for Fe-MOR0.25. Almost all the methanol formed is overoxidized to CO and CO_2. However, the addition of mesopores suppressed overoxidation reaction by shortening the escape pathway of methanol before going through overoxidation. The addition of mesopores decreased CO formation 70 times. The conversions of methane and nitrous oxide are significantly higher over Fe-MOR0.25 than Fe-MesoMORnew 15 and 0.3% for methane and 68 and 1% for nitrous oxide, respectively. However, higher amount of converted oxidizing agent is used for methane and methanol overoxidation to CO and CO_2 over Fe-MOR0.25.

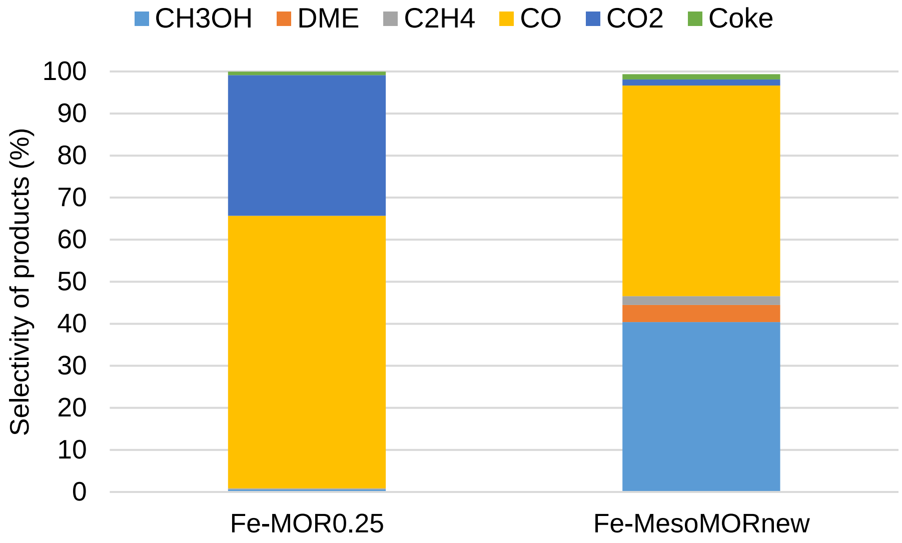

Figure 4.47 Product distribution over Fe-MOR0.25 and Fe-MesoMORnew (300 °C, 300 mg catalyst, 100 sccm, 30% CH_4, 10% N_2O, 11% H_2O (balance He))

4.2.6 Comparison of MOR, ZSM-5 and FER at Optimum Conditions

Iron-exchanged microporous (Fe-MOR0.25) and mesoporous (Fe-MesoMORnew) MOR are compared with Fe-FER and Fe-ZSM-5 at optimum conditions determined for Fe-MesoMORnew, which is at 300 ºC with a total flowrate of 100 sccm and feed composition of 30% CH_4, 10% N_2O and 20% H_2O. The detailed reaction results are summarized in Appendix E (Table E.7). While reporting average products results, data obtained at 200–250 minutes are used for Fe-MesoMORnew and Fe-FER and all the data are considered for Fe-MOR0.25 and Fe-ZSM-5. The methanol time on stream of Fe-MOR0.25, Fe-MesoMORnew, Fe-FER and Fe-ZSM-5 are given in Figure 4.48. The highest average methanol formation rate is obtained over Fe-FER (581 µmol/g/h) where Fe-MOR0.25 (325 µmol/g/h), Fe-MesoMORnew (330 μmol/g/h) and Fe-ZSM-5 (267 μmol/g/h) are similar to each other. Moreover, there is slight deactivation observed over Fe-ZSM-5 but not over other zeolites.

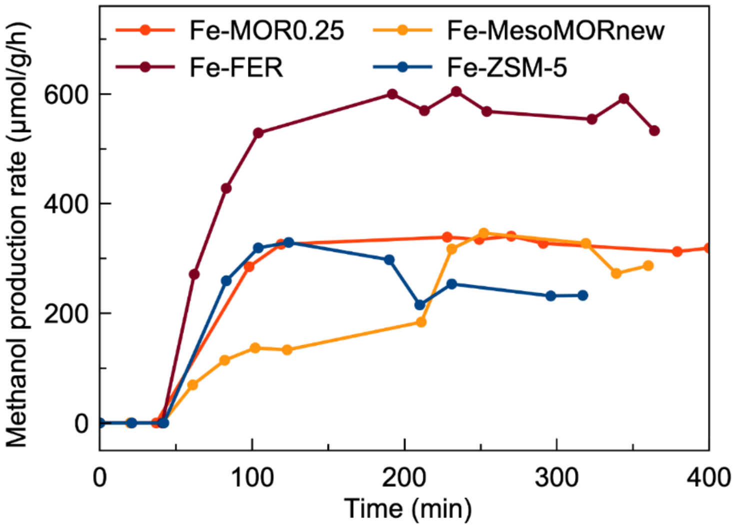

Figure 4.48 Methanol production rate over iron-exchanged micro- and meso- MOR, FER, and ZSM-5 (300 ºC, 300 mg catalyst, 100 sccm, 30% CH_4, 10% N_2O, 14–23% H_2O (balance He))

The selectivity of products is given in Figure 4.49, the selectivity of C_3H_6, C_3H_8 and C_4 products are not included. The highest coke selectivity is obtained over Fe-ZSM-5 (17%). The water vapor in feed is less in Fe-ZSM-5 with 14% in feed composition where for other zeolites used, water vapor composition in feed is in the range of 22–24%. Higher water vapor would suppress the coke formation, however considering that the highest coke selectivity is 10% on Fe-MesoMORold at 3% water vapor, 14% coke selectivity observed on Fe-ZSM-5 at >14% water vapor indicates higher coke formation on ZSM-5. Also, the highest C_2H_4, C_3H_6 and C_3H_8 selectivity are obtained over Fe-ZSM-5, which suggests the MTO mechanism is favored mostly in Fe-ZSM-5. In Figure 4.49, selectivity of C_2H_6, C_3H_6, C_3H_8 and C_4 products are not included since for Fe-MOR0.25, Fe-MesoMORnew and Fe-FER the selectivity of these products does not exceed 0.6%. However, for Fe-ZSM-5 the total of these products is 2%. The major product causing lower methanol selectivity is CO and the highest CO selectivity is obtained over both micro- and meso- MOR. This result might be due to one dimensional channels of MOR where FER has two dimensional and ZSM-5 has three dimensional channels. Due to transfer limitations in one dimensional channels of MOR, the possibility of methanol leaving the channels without going overoxidation is less than FER and ZSM-5 frameworks. The CO selectivity is halved in FER and ZSM-5 than Fe-MOR0.25 and Fe-MesoMORnew, which results in increased methanol selectivity. The high selectivity of coke in Fe-ZSM-5 caused lower methanol selectivity in Fe-ZSM-5 (49%) than Fe-FER (71%). The higher selectivity of methanol and lower selectivity of secondary reactions are proposed to be due to the migration of formed methoxy groups to silanol groups on Fe-FER where methoxy groups bound to iron sites in Fe-ZSM-5 and Fe-*BEA are more prone to be overoxidized, thus low methanol selectivity [129].

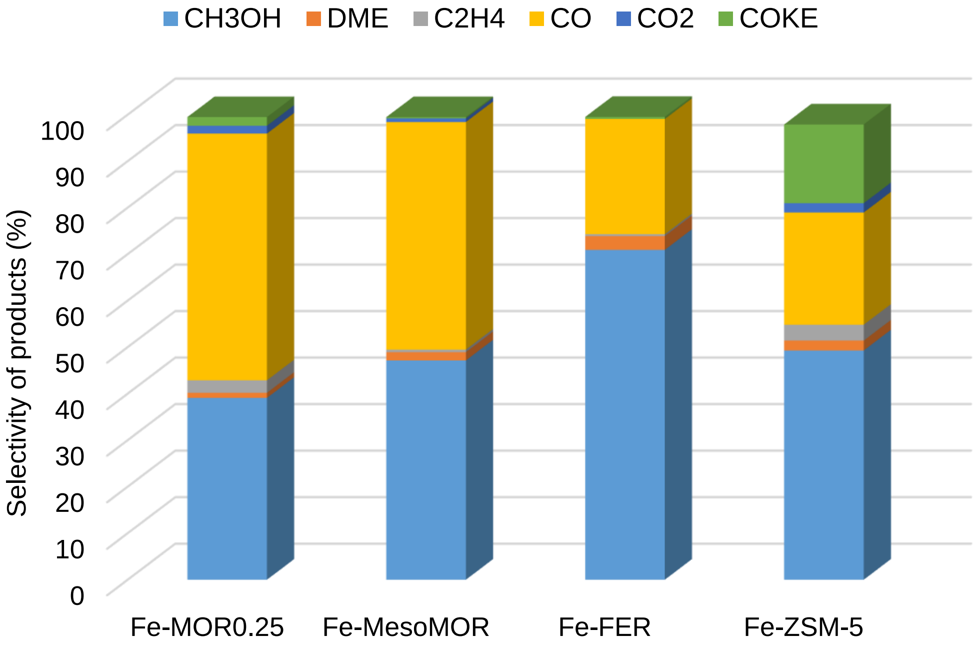

Figure 4.49 The selectivity of products over Fe-MOR0.25, Fe-MesoMORnew, Fe-FER and Fe-ZSM-5 (300 mg catalyst, 100 sccm, 30% CH_4, 10% N_2O, 14–23% H_2O (balance He))

Fe-MesoMORnew and Fe-FER are further compared at slightly elevated reaction temperatures, 320 and 340 °C. Methanol time on stream over these zeolites at 320 and 340 °C are given in Figure 4.50. As can be seen from Figures 4.48 and 4.50, the methanol formation rate over Fe-FER is higher than Fe-MesoMORnew at all three temperatures, 300, 320 and 340 °C. Both zeolites did not deactivate at temperatures 300 and 320 °C. However, as the reaction temperature is increased to 340 °C, deactivation is observed over Fe-MesoMORnew. Even though the area percentage of Fe_xO_y species and the presence of large surface oxygen species in Fe-FER, which are thought to be inactive for methane partial oxidation, Fe-FER exhibit higher TOF values than Fe-MesoMORnew at all three temperatures. The activity of extra-framework Fe species, the suggested position of active sites, are found to be higher than the extra-framework Fe species in Fe-MesoMORnew.

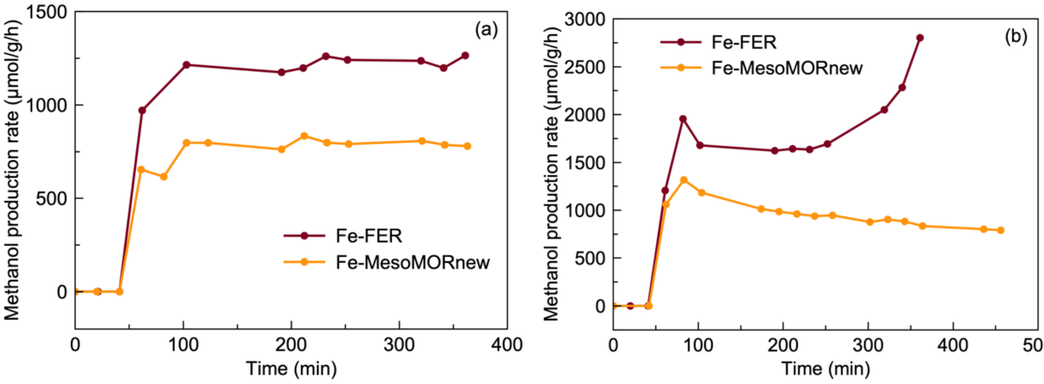

Figure 4.50 Methanol production rate over Fe-MesoMORnew and Fe-FER (300 mg catalyst, 100 sccm, 30% CH_4, 10% N_2O, 20–24% H_2O (balance He)) (a) T=320 °C and (b) T=340 °C

The detailed reaction results are given in Appendix E (Table E.7). The conversions of CH_4 and N_2O increased as the reaction temperature is increased from 300 to 340 ºC due to enhanced kinetics. The increase in N_2O conversion reached to 2.8% at 340 ºC on Fe-FER where it reached 5.4% at 340 ºC on Fe-MesoMORnew. Due to higher conversion of oxidant, higher overoxidation products and coke formation is observed over Fe-MesoMORnew at 340 ºC. At 320 ºC, N_2O conversions are similar on both zeolites as well as CO formation rate, but more CO and coke are formed over Fe-MesoMORnew. It is already shown that the formed methoxy groups migrate from the iron active sites to silanol groups over Fe-FER using in-situ FTIR where methoxy groups bound to iron active sites are more prone to overoxidation over Fe-ZSM-5 and Fe-*BEA, which result with higher methanol selectivity and lower secondary reaction products [129]. For Fe-MesoMORnew the formed methoxy groups might be bound to iron centers or due to one-dimensional diffusion pathway, the chance of methanol overoxidation is higher over Fe-MesoMORnew when compared to Fe-FER, despite of addition of mesopores in MOR.

The selectivity of products are given in Figure 4.51. The selectivity of C_2H_6, C_3H_6, C_3H_8 and C_4 products are not included in Figure 4.51 since the total selectivity of not included products are below 0.8%. As can be seen from Figure 4.51, as temperature is increased from 300 to 340 °C, the selectivity of C_2H_4, CO_2 and coke are increased, where the selectivity of CO and CH_3OH are decreased over Fe-MesoMORnew. However, the selectivity of all products is similar to each other except coke over Fe-FER as temperature is increased from 320 to 340 °C. Even though CO selectivity over two zeolites is slightly different (8%) than each other at 320 °C, as the temperature is increased from 320 to 340 °C, the difference drops to 3%. However, the difference in methanol selectivity is increased from 9 to 17%, with Fe-FER being higher than Fe-MesoMORnew, with increased temperature. The main reason behind that increase in difference is the accelerated secondary reactions and tripled CO_2 and coke selectivity over Fe-MesoMORnew.

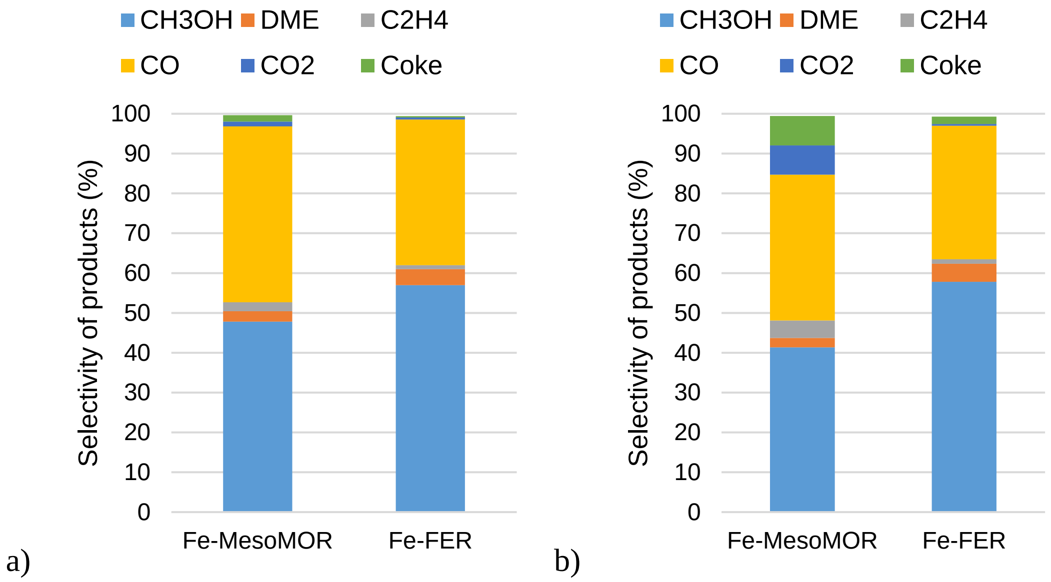

Figure 4.51 The selectivity of products over Fe-MesoMORnew and Fe-FER (300 mg catalyst, 100 sccm, 30% CH_4, 10% N_2O, 20–24% H_2O (balance He)) a) T=320 °C and b) T=340 °C

In literature, methanol formation rate and selectivity excluding coke are reported as ca. 491 μmol/g/h and 17%, respectively, over Fe-MOR [133]. In this study, by introducing 24% H_2O in feed, methanol selectivity of 39%, including coke, is achieved at 300 °C over Fe-MOR. Also, by adding mesopores methanol selectivity is improved to 47% over Fe-MesoMORnew. Moreover, 21% methanol selectivity with calculated methanol formation rate of 1010 μmol/g/h are obtained over Fe-FER at 350 °C by Zhao et al. [129]. By including 24% water vapor in feed, higher methanol formation rate, 1648 μmol/g/h, and selectivity, 58%, are obtained over Fe-FER.

4.2.7 Activation Energy Calculations

In order to calculate the activation energy of methane activation and methanol production, catalysts are tested at least at three temperatures and the Arrhenius equation is used for E_a calculation as given in Equations 4.4 and 4.5.

$$k = A * e^{-\frac{E_a}{R*T}} \quad \text{(Eqn. 4.4)}$$

$$\ln(rate) = \left(-\frac{E_a}{R}\right) * \left(\frac{1}{T}\right) + \ln(B) \quad \text{(Eqn. 4.5)}$$

Methane activation rate is calculated using carbon balanced equation as given in Equation 4.6.

$$r_{CH4} = 1 * \sum r_{C1\,products} + 2 * \sum r_{C2\,products} + 3 * \sum r_{C3\,products} + 4 * \sum r_{C4\,products} + r_{Coke} \quad \text{(Eqn. 4.6)}$$

The activation energy of N_2O conversion is calculated using the rare of N_2 produced over rate of N_2O in feed.

The slope of ln(r_{CH4}), ln(r_{N2O}) or ln(r_{CH3OH}) versus 1/T plot gives activation energy of methane and nitrous oxide conversion and methanol production, respectively.

4.2.7.1 Fe-MOR0.25 with 22% H_2O

Methanol time on stream over Fe-MOR0.25 with H_2O in feed at 300, 320 and 340 °C are given Figure 4.52. The detailed reaction results can be found in Appendix E (Table E.8), while calculating average reaction, all the data are taken into calculations at 300 °C since no deactivation is observed. However, since deactivation is observed at 320 and 340 °C, first two or three data are taken into calculations.

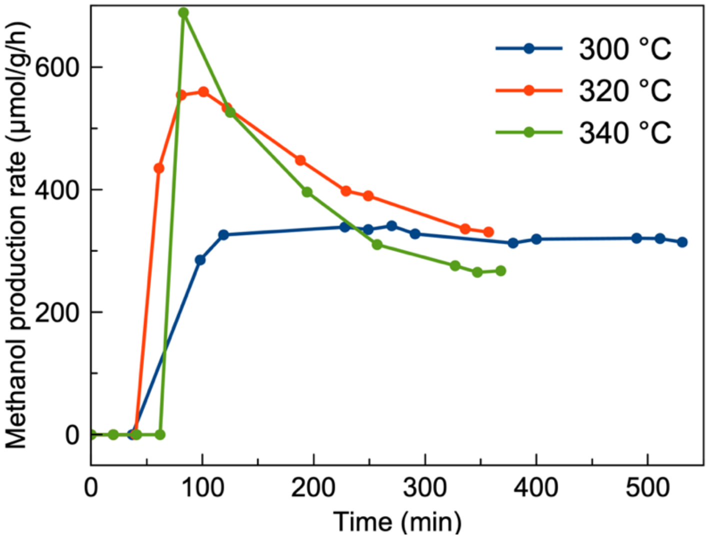

Figure 4.52 Methanol time on stream over Fe-MOR0.25 at different temperatures (300–340 °C, 300 mg catalyst, 100 sccm, 30% CH_4, 10% N_2O, 21–22% H_2O (balance He))

Using Arrhenius plot, Figure 4.53, activation energy of methane and nitrous oxide conversions over Fe-MOR0.25 are found to be 124 and 130 kJ/mol and methanol formation activation energy is found to be 46 kJ/mol. Detailed reaction results are given in Appendix E (Table E.8).

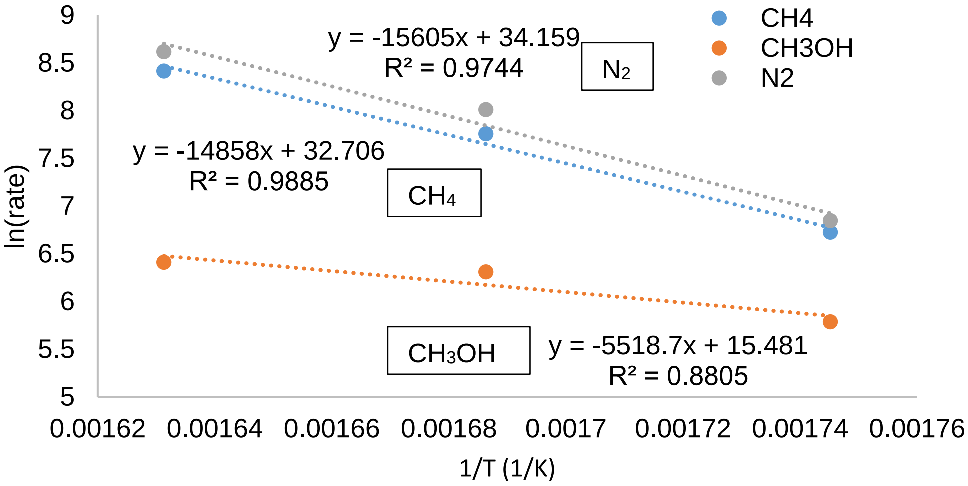

Figure 4.53 Natural logarithm of rates of CH_4, N_2O and CH_3OH over Fe-MOR0.25 at different temperatures (300–340 °C, 300 mg catalyst, 100 sccm, 30% CH_4, 10% N_2O, 21–22% H_2O (balance He))

4.2.7.2 Fe-MesoMORnew with 13% H_2O

Methanol formation rate over Fe-MesoMORnew with 10–15% H_2O in feed at 270, 300 and 330 °C with respect to time are given in Figure 4.54. As can be seen from Figure 4.54, deactivation is only observed at 330 °C. For activation energy calculations, data obtained between 170 and 230 minutes are taken into consideration. The detailed reaction results are given in Table E.9.

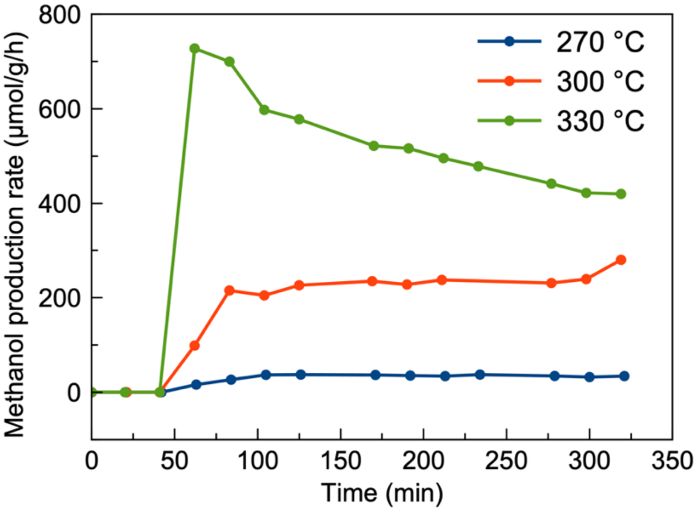

Figure 4.54 Methanol time on stream over Fe-MesoMORnew (270–330 °C, 300 mg catalyst, 100 sccm, 30% CH_4, 10% N_2O, 10–15% H_2O (balance He))

As a result, methane and nitrous oxide conversion activation energy are calculated as 158 and 181 kJ/mol, respectively (see Figure 4.55). Also, the activation energy for methanol production is found as 121 kJ/mol.

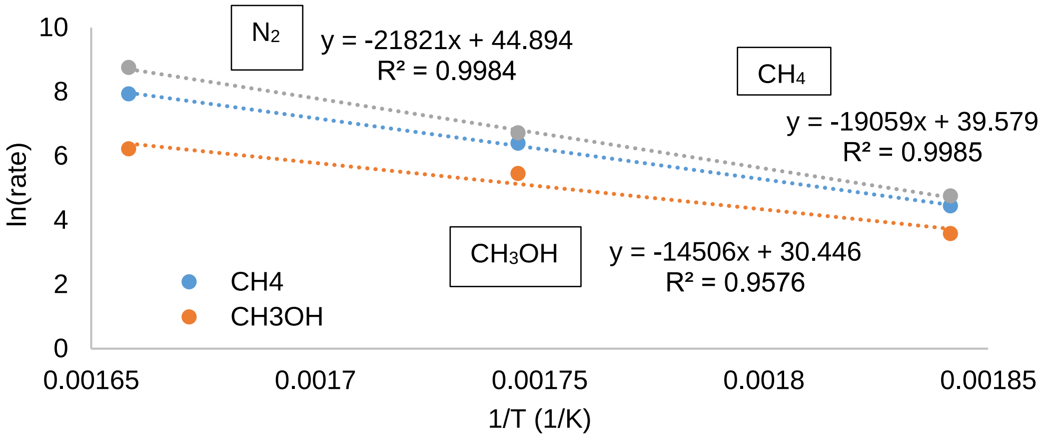

Figure 4.55 Natural logarithm of rates of CH_4, N_2O and CH_3OH at different temperatures (270–330 °C, 300 mg catalyst, 100 sccm, 30% CH_4, 10% N_2O, 10–15% H_2O (balance He))

4.2.7.3 Fe-MesoMORnew with 22% H_2O

Methanol time on stream for Fe-MesoMORnew with 22% H_2O in feed is given at temperatures 300, 320 and 340 °C in Figure 4.56. The activation energies are calculated using most stable data region between 200 and 250 minutes. The detailed reaction results can be found in Appendix E (Table E.10).

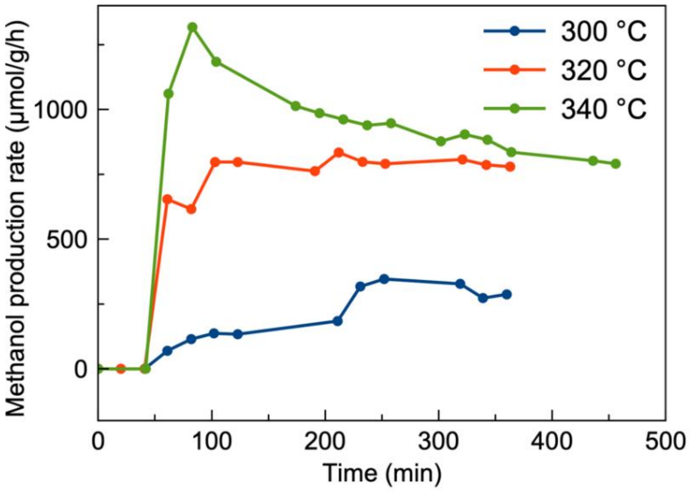

Figure 4.56 Methanol time on stream over Fe-MesoMORnew (300–340 °C, 300 mg catalyst, 100 sccm, 30% CH_4, 10% N_2O, 22–23% H_2O (balance He))

Using Figure 4.57, activation energy of methane and nitrous oxide conversions are found to be 88 kJ/mol and 141 kJ/mol and for methanol production it is calculated as 78 kJ/mol.

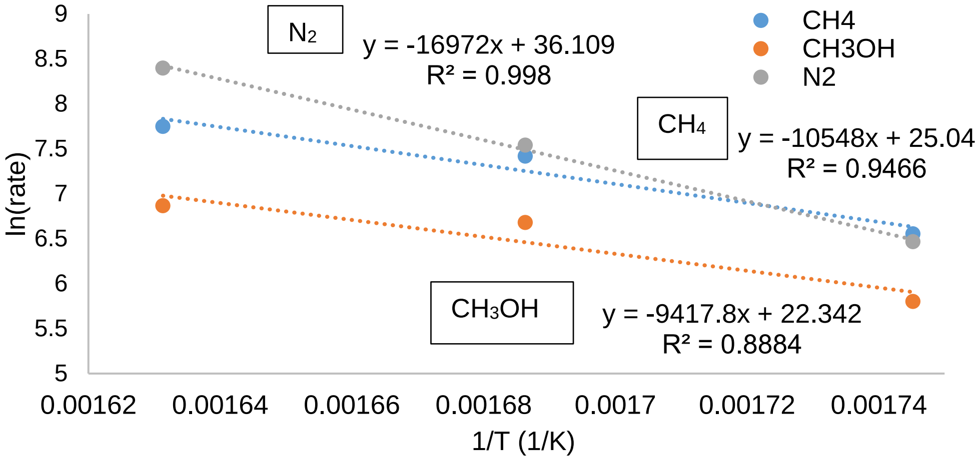

Figure 4.57 Natural logarithm of rates of CH_4, N_2O and CH_3OH over Fe-MesoMORnew at different temperatures (300–340 °C, 300 mg catalyst, 100 sccm, 30% CH_4, 10% N_2O, 22–23% H_2O (balance He))

4.2.7.4 Fe-FER with 22% H_2O

Methanol formation rate over time for FeFER with 22% H_2O in feed at temperatures 280, 300, 320 and 340 °C are given in the Figure 4.58. The detailed results can be found in Appendix E (Table E.11). The data obtained at 200–250 minutes are considered for reporting average formation rates of products.

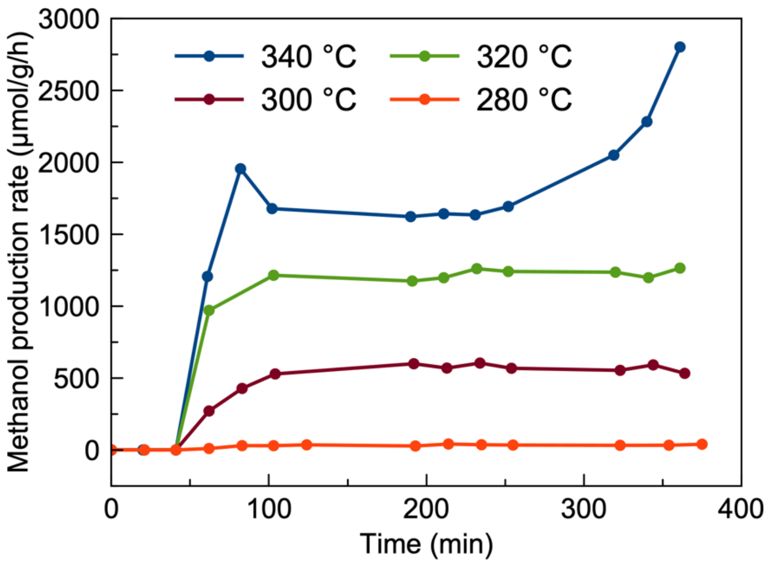

Figure 4.58 Methanol time on stream over Fe-FER (280–340 °C, 300 mg catalyst, 100 sccm, 30% CH_4, 10% N_2O, 20–22% H_2O (balance He))

Using the Arrhenius plot, Figure 4.59, the activation energy of methane and nitrous oxide conversions are calculated as 175 and 164 kJ/mol and the activation energy of methanol production is found as 176 kJ/mol.

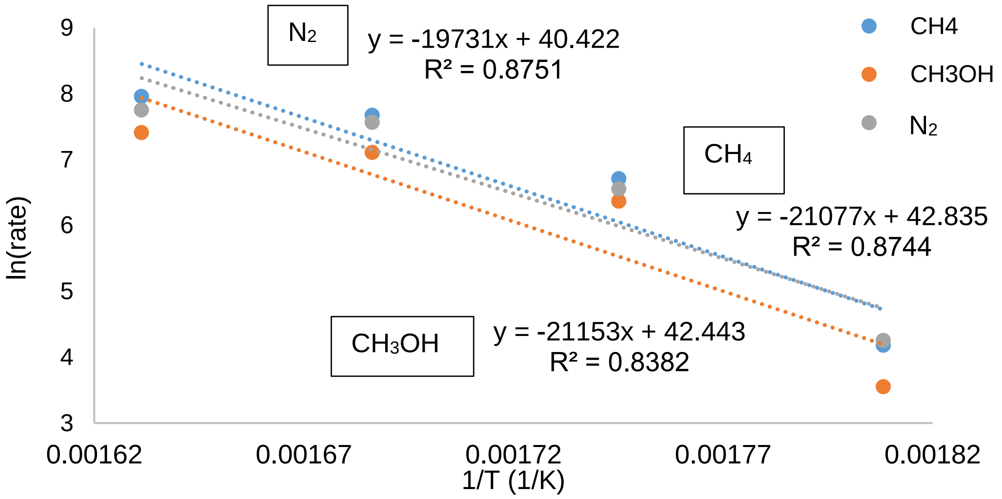

Figure 4.59 Natural logarithm of rates of CH_4, N_2O and CH_3OH over Fe-FER at different temperatures (280–340 °C, 300 mg catalyst, 100 sccm, 30% CH_4, 10% N_2O, 20–22% H_2O (balance He))

4.2.7.5 Comparison with Theoretical Studies

Experimental results are compared with Density Functional Theory (DFT) calculations carried out over $[Fe]^{2+}$-MFI zeolite [18]. In this study, activation energy of N-O bond cleavage over $[Fe]^{2+}$-MFI is calculated as 13.7 kcal/mol (57 kJ/mol). Then, methane interaction with $[FeO]^{2+}$-MFI zeolite is studied, and C-H bond cleavage energy of methane is calculated to be 6.3 kcal/mol (26 kJ/mol). Moreover, methanol desorption energy is found to be 32.8 kcal/mol (137 kJ/mol), which is the highest activation energy indicating methanol desorption from the surface is the rate determining step in methanol formation. These DFT results are compared with experimental results, which are calculated in the absence of water vapor, in Table 4.3.

Water has known effect on methanol desorption from the surface, especially at lower temperatures in 3-step process. Thus, including water vapor has decreased methanol desorption energy from 54.0 to 28.8 kcal/mol (227.6 kJ/mol to 120.5 kJ/mol) for $[CuO_2(\mu\text{-}O)]^{2+}$-MOR zeolite [18], [149]. This finding is consistent with experimental result over Fe-MesoMORnew as water vapor is increased from 13 to 22% methanol formation energy is decreased. The difference in activation energies indicate formation of different active sites. In the presence of water vapor with high composition (~20%), there is possibility of active sites containing oxo or hydroxyl groups. The C-H activation barrier and methanol desorption energies over $[Fe_2(\mu\text{-}O)]^{2+}$ site are reported as 132 and 145 kJ/mol, respectively, with C-H activation being the rate determining step [169]. Also, the C-H activation barrier over $[Fe_2(\mu\text{-}O)_2]^{2+}$ site is calculated as 173.6 kJ/mol, which is close to experimentally calculated value of 175.2 kJ/mol over Fe-FER. However, reported methanol desorption over $[Fe_2(\mu\text{-}O)_2]^{2+}$ site 37.2 kJ/mol is almost five times lower than experimental value, 175.9 kJ/mol [18].

Table 4-3 The comparison of experimentally and theoretically calculated activation energies

Fe-zeolite	Nitrous Oxide Conversion	Methane Conversion	Methanol Formation
	kJ/mol		
MOR0.25 (22 % H_2O)	130	124	45.9
MesoMORnew (13% H_2O)	181	158	121
MesoMORnew (22% H_2O)	141	87.7	78.3
FER (22% H_2O)	164	175	176
$[FeO]^{2+}$ [18]	57^{*}	26.4^{**}	137^{***}
$[Fe_2(\mu\text{-}O)]^{2+}$ [169]	-	132	145
$[Fe_2(\mu\text{-}O)_2]^{2+}$ [18]	-	174	37
$[Fe_2(\mu\text{-}OH)_2]^{2+}$ [109]	-	50	-

*: activation energy of N-O bond cleavage

**: activation energy of C-H bond cleavage

***: activation energy of methanol desorption from the surface

CHAPTER 5

CONCLUSION

In this study, the effects of framework and mesopore addition on methanol formation rate and selectivity were studied over iron-exchanged SSZ-13, SSZ-39 and MOR. Then, the optimizations in terms of iron content and reactant compositions at 300 °C were performed over best performing zeolite among SSZ-13, SSZ-39 and MOR. The effect of water vapor in methanol selectivity was studied over Fe-MesoMOR. Mesopore addition to MOR was further investigated at slightly elevated reaction temperatures, 320 and 340 °C, with both low and high water vapor in feed. Also, the best performed Fe-zeolites which are micro- and mesoporous MOR were compared with Fe-FER and Fe-ZSM-5, which are best performed and mostly studied Fe-zeolites in literature. The activation energies of methane and nitrous oxide conversions as well as methanol formation were calculated for Fe-MOR (22% H_2O), Fe-MesoMOR (13 and 22% H_2O) and Fe-FER (22% H_2O).

Fe-MOR, large pore zeolite, was able to produce methanol in steady state even in microporous form and the mesopore addition to MOR increased methanol formation rate and selectivity significantly. On the other hand, small pore zeolites, SSZ-13 and SSZ-39, deactivated quickly due to coke formation even after mesopore addition except for Fe-MesoSSZ-39, which produced methanol in steady-state but also produced C4 products that were not observed over Fe-MesoMOR. Thus, MOR was chosen framework for further optimization.

The effect of iron content on methanol selectivity was studied over Fe-MOR since at higher iron content, over-oxidation could be enhanced. Indeed, the lowest TOF methanol was obtained over Fe-MOR with the highest Fe content, in addition to slight deactivation. The highest TOF, 1044 μmol CH_3OH/mmol Fe/h, and methanol formation rate, 333 μmol/g/h, with 25% selectivity was obtained over Fe-MOR0.75 with 0.319 mmol Fe/g iron content and chosen as optimum iron content.

The optimization of reactant compositions was performed over Fe-MesoMOR, and at 300 °C the optimum methane and nitrous oxide compositions were determined as 30% and 10%, respectively. Also, increased water vapor in the feed favored methanol selectivity but due to the competitive adsorption of water vapor and N_2O, slight decrease in methanol activity was observed. The optimum water vapor concentration was selected as 22% for Fe-MesoMORnew. At these optimized conditions, methanol formation rate of 330 μmol/g/h with 47% selectivity was obtained over Fe-MesoMORnew.

The mesopore addition was further investigated over Fe-MOR both with low (11%) and high (22%) water vapor in the feed. Mesopore addition contributed to methanol stability. Deactivation was observed on microporous Fe-MOR0.25 at 320 °C, whereas over Fe-MesoMORnew, it started at 340 °C. Methanol production rate was also promoted with mesopore addition at 320 and 340 °C. The effect of mesopores was found more dominant at low water vapor concentration in the feed. Methanol selectivity increased from 0.7% to 40 % at 300 ºC with mesopore addition, due to shortened diffusion pathways and thus prevented overoxidation of methanol to CO, CO_2, and coke.

Fe-FER showed the highest methanol selectivity (71%) and methanol formation rate (581 μmol/g/h) at 300 ºC compared to micro- and mesoporous MOR and ZSM-5. Fe-MesoMORnew and Fe-ZSM-5 showed similar methanol selectivity (~48%) at 300 ºC but with different product distribution. The highest coke formation was obtained over Fe-ZSM-5, where CO formation was more dominant over Fe-MOR0.25, which caused lowered methanol selectivity. At 340 ºC, slight deactivation was observed over Fe-MesoMORnew, where no deactivation is observed over Fe-FER. Fe-FER produced methanol with higher formation rate and selectivity compared to Fe-MesoMORnew at all temperatures.

In order to characterize the active sites, DR UV–Vis spectra was used before and after consecutive treatments of N_2O and CH_4 at 300 ºC. There was a band shift observed from 270 nm to 350 nm over pure Fe-MOR0.25 upon treatment with N_2O. However, there were no changes observed over Fe-MesoMORnew, Fe-FER and Fe-ZSM-5 mixed with $BaSO_4$. The reason might be the low Fe content of the sample or the lack of the high temperature activation step.

Similar methanol formation activation energies were obtained over Fe-MesoMORnew and Fe-FER, which are significantly higher than Fe-MOR0.25. Lower activation energy for methanol formation is obtained over Fe-MesoMOR with increased water vapor in feed from 13 to 22%, which supports water vapor helping methanol desorption from the surface. However, the obtained results were different than the theoretical results reported for $[FeO]^{2+}$-ZSM-5 site where water vapor is not taken into consideration. In the presence of water vapor, the active sites formed might differ and might contain oxo or hydroxyl groups.

REFERENCES

[1] B. Yilmaz and U. Müller, “Catalytic applications of zeolites in chemical industry,” in *Topics in Catalysis*, Jun. 2009, vol. 52, no. 6–7, pp. 888–895.

[2] J. H. Lunsford, “Catalytic conversion of methane to more useful chemicals and fuels: a challenge for the 21st century,” *Catal Today*, vol. 63, pp. 165–174, 2000.

[3] R. Barati and J. T. Liang, “A review of fracturing fluid systems used for hydraulic fracturing of oil and gas wells,” *J Appl Polym Sci*, vol. 131, no. 16, Aug. 2014.

[4] M. Saunois *et al.*, “The global methane budget 2000-2017,” *Earth Syst Sci Data*, vol. 12, no. 3, pp. 1561–1623, Jul. 2020.

[5] D. R. Caulton, P. B. Shepson, M. O. L. Cambaliza, D. McCabe, E. Baum, and B. H. Stirm, “Methane destruction efficiency of natural gas flares associated with shale formation wells,” *Environ Sci Technol*, vol. 48, no. 16, pp. 9548–9554, Aug. 2014.

[6] R. B. Jackson, E. I. Solomon, J. G. Canadell, M. Cargnello, and C. B. Field, “Methane removal and atmospheric restoration,” *Nat Sustain*, vol. 2, no. 6, pp. 436–438, Jun. 2019.

[7] R. L. Mortensen, H. D. Noack, K. Pedersen, S. Mossin, and J. Mielby, “Recent Advances in Complete Methane Oxidation using Zeolite-Supported Metal Nanoparticle Catalysts,” *ChemCatChem*, 2022.

[8] U.S. Energy Information Administration, “Annual Energy Outlook with projections to 2050,” Mar. 2022.

[9] A. I. Olivos-Suarez, À. Szécsényi, E. J. M. Hensen, J. Ruiz-Martinez, E. A. Pidko, and J. Gascon, “Strategies for the Direct Catalytic Valorization of Methane Using Heterogeneous Catalysis: Challenges and Opportunities,” *ACS Catal*, vol. 6, no. 5, pp. 2965–2981, 2016.

[10] G. A. Olah, “Beyond oil and gas: The methanol economy,” *Angewandte Chemie - International Edition*, vol. 44, no. 18, pp. 2636–2639, Apr. 2005.

[11] C. E. Bjorck, P. D. Dobson, and J. Pandhal, “Biotechnological conversion of methane to methanol: evaluation of progress and potential,” *AIMS Bioeng*, vol. 5, no. 1, pp. 1–38, 2018.

[12] S. Iliev, “A comparison of ethanol, methanol, and butanol blending with gasoline and its effect on engine performance and emissions using engine simulation,” *Processes*, vol. 9, Aug. 2021.

[13] J. Sehested, “Industrial and scientific directions of methanol catalyst development,” *J Catal*, vol. 371, pp. 368–375, Mar. 2019.

[14] R. Sharma, H. Poelman, G. B. Marin, and V. v. Galvita, “Approaches for selective oxidation of methane to methanol,” *Catalysts*, vol. 10, no. 2. MDPI, Feb. 01, 2020.

[15] M. J. da Silva, “Synthesis of methanol from methane: Challenges and advances on the multi-step (syngas) and one-step routes (DMTM),” *Fuel Processing Technology*, vol. 145. Elsevier, pp. 42–61, May 01, 2016.

[16] R. Banerjee, J. C. Jones, and J. D. Lipscomb, “Soluble Methane Monooxygenase,” *Annu Rev Biochem*, vol. 88, pp. 409–431, .

[17] M. O. Ross and A. C. Rosenzweig, “A tale of two methane monooxygenases,” *Journal of Biological Inorganic Chemistry*, vol. 22, no. 2–3, pp. 307–319, Apr. 2017.

[18] M. Mahyuddin, Y. Shiota, and K. Yoshizawa, “Methane selective oxidation to methanol by metal-exchanged zeolites: A review of active sites and their reactivity,” *Catal Sci Technol*, vol. 9, no. 8, 2019.

[19] B. Ruscic, “Active Thermochemical Tables: Sequential Bond Dissociation Enthalpies of Methane, Ethane, and Methanol and the Related

Thermochemistry," *Journal of Physical Chemistry A*, vol. 119, no. 28, pp. 7810–7837, Jul. 2015.

[20] S. Li, R. Ahmed, Y. Yi, and A. Bogaerts, "Methane to methanol through heterogeneous catalysis and plasma catalysis," *Catalysts*, vol. 11, no. 5. MDPI, May 01, 2021.

[21] M. Ravi, M. Ranocchiari, and J. A. van Bokhoven, "The Direct Catalytic Oxidation of Methane to Methanol—A Critical Assessment," *Angewandte Chemie - International Edition*, vol. 56, no. 52, pp. 16464–16483, 2017.

[22] G. I. Panov, V. I. Sobolev, and A. S. Kharitonov, "THE ROLE OF IRON IN NaO DECOMPOSITION ON ZSM-5 ZEOLITE AND REACTIVITY OF THE SURFACE OXYGEN FORMED," 1990.

[23] M. Moshoeshoe, M. Silas Nadiye-Tabbiruka, and V. Obuseng, "A Review of the Chemistry, Structure, Properties and Applications of Zeolites," *American Journal of Materials Science*, vol. 2017, no. 5, pp. 196–221, 2017.

[24] D. S. Coombs *et al.*, "Recommended nomenclature for zeolite minerals: report of the subcommittee on zeolites of the International Mineralogical Association, Commission on new Minerals and Mineral names," *Can Mineral*, vol. 35, no. 6, pp. 1571–1606, 1997.

[25] E. M. Flanigen, R. W. Broach, and S. T. Wilson, *Zeolites in Industrial Separation and Catalysis*. 2010.

[26] R. E. Fletcher, S. Ling, and B. Slater, "Violations of Löwenstein's rule in zeolites," *Chem Sci*, vol. 8, no. 11, pp. 7483–7491, 2017.

[27] M. Yabushita, R. Osuga, and A. Muramatsu, "Control of location and distribution of heteroatoms substituted isomorphously in framework of zeolites and zeotype materials," *CrystEngComm*, vol. 23, no. 36, pp. 6226–6233, Sep. 2021.

[28] "International Zeolite Association. Database of Zeolite Structures," *http://www.iza-structure.org/databases/.*

[29] X. Jia, W. Khan, Z. Wu, J. Choi, and A. C. K. Yip, "Modern synthesis strategies for hierarchical zeolites: Bottom-up versus top-down strategies," *Advanced Powder Technology*, vol. 30, no. 3, pp. 467–484, Mar. 2019.

[30] X. Zhao, J. Xu, and F. Deng, "Solid-state NMR for metal-containing zeolites: From active sites to reaction mechanism," *Front Chem Sci Eng*, vol. 14, no. 2, pp. 159–187, Apr. 2020.

[31] G. V. A. Martins, G. Berlier, C. Bisio, S. Coluccia, H. O. Pastore, and L. Marchese, "Quantification of brønsted acid sites in microporous catalysts by a combined FTIR and NH3-TPD study," *Journal of Physical Chemistry C*, vol. 112, no. 18, pp. 7193–7200, May 2008.

[32] E. M. El-Malki, R. A. van Santen, and W. M. H. Sachtler, "Introduction of Zn, Ga, and Fe into HZSM-5 cavities by sublimation: Identification of acid sites," *Journal of Physical Chemistry B*, vol. 103, no. 22, pp. 4611–4622, Jun. 1999.

[33] A. S. Al-Dughaither and H. de Lasa, "HZSM-5 zeolites with different SiO2/Al2O3 ratios. Characterization and NH3 desorption kinetics," *Ind Eng Chem Res*, vol. 53, no. 40, pp. 15303–15316, Oct. 2014.

[34] J. Kowalska-Kuś, A. Held, and K. Nowińska, "Oxydehydrogenation of C2-C4 hydrocarbons over Fe-ZSM-5 zeolites with N2O as an oxidant," *Catal Sci Technol*, vol. 3, no. 2, pp. 508–518, 2013.

[35] K. Margeta, N. Zabukovec, M. Siljeg, and A. Farkas, "Natural Zeolites in Water Treatment – How Effective is Their Use," in *Water Treatment*, InTech, 2013.

[36] "REPORTING PHYSISORPTION DATA FOR GAS/SOLID SYSTEMS with Special Reference to the Determination of Surface Area and Porosity (Recommendations 1984)," 1985.

[37] E. Koohsaryan and M. Anbia, "Nanosized and hierarchical zeolites: A short review," *Cuihua Xuebao/Chinese Journal of Catalysis*, vol. 37, no. 4. Science Press, pp. 447–467, Apr. 01, 2016.

[38] D. P. Serrano, J. M. Escola, and P. Pizarro, "Synthesis strategies in the search for hierarchical zeolites," *Chem Soc Rev*, vol. 42, no. 9, pp. 4004–4035, Apr. 2013.

[39] A. H. Janssen, I. Schmidt, C. J. H. Jacobsen, A. J. Koster, and K. P. de Jong, "Exploratory study of mesopore templating with carbon during zeolite synthesis," *Microporous and Mesoporous Materials*, vol. 65, no. 1, pp. 59–75, Oct. 2003.

[40] Y. Tao, H. Kanoh, and K. Kaneko, "Uniform mesopore-donated zeolite Y using carbon aerogel templating," *Journal of Physical Chemistry B*, vol. 107, no. 40. American Chemical Society, pp. 10974–10976, Oct. 09, 2003.

[41] H. Zhu, Z. Liu, Y. Wang, D. Kong, X. Yuan, and Z. Xie, "Nanosized CaCO3 as hard template for creation of intracrystal pores within silicalite-1 crystal," *Chemistry of Materials*, vol. 20, no. 3, pp. 1134–1139, Feb. 2008.

[42] B. P. S. Santos, N. C. Almeida, I. S. Santos, M. de F. v. Marques, and L. D. Fernandes, "Synthesis and Characterization of Mesoporous Mordenite Zeolite Using Soft Templates," *Catal Letters*, vol. 148, no. 7, pp. 1870–1878, Jul. 2018.

[43] M. Hartmann, M. Thommes, and W. Schwieger, "Hierarchically-Ordered Zeolites: A Critical Assessment," *Advanced Materials Interfaces*, vol. 8, no. 4. Wiley-VCH Verlag, Feb. 01, 2021.

[44] S. van Donk, A. H. Janssen, J. H. Bitter, and K. P. de Jong, “Generation, characterization, and impact of mesopores in zeolite catalysts,” *Catalysis Reviews - Science and Engineering*, vol. 45, no. 2. pp. 297–319, May 2003.

[45] Z. Qin *et al.*, “A defect-based strategy for the preparation of mesoporous zeolite y for high-performance catalytic cracking,” *J Catal*, vol. 298, pp. 102–111, Feb. 2013.

[46] J. C. Groen, J. C. Jansen, J. A. Moulijn, and J. Pérez-Ramírez, “Optimal aluminum-assisted mesoporosity development in MFI zeolites by desilication,” *Journal of Physical Chemistry B*, vol. 108, no. 35, pp. 13062–13065, Sep. 2004.

[47] D. Verboekend and J. Pérez-Ramírez, “Desilication mechanism revisited: Highly mesoporous all-silica zeolites enabled through pore-directing agents,” *Chemistry - A European Journal*, vol. 17, no. 4, pp. 1137–1147, Jan. 2011.

[48] B. Liu *et al.*, “Synthesis of low-silica CHA zeolite chabazite in fluoride media without organic structural directing agents and zeolites,” *Microporous and Mesoporous Materials*, vol. 196, pp. 270–276, Sep. 2014.

[49] C. Wen *et al.*, “A comparative first principles study on trivalent ion incorporated SSZ-13 zeolites,” *Physical Chemistry Chemical Physics*, vol. 17, no. 44, pp. 29586–29596, 2015.

[50] J. H. Kwak, R. G. Tonkyn, D. H. Kim, J. Szanyi, and C. H. F. Peden, “Excellent activity and selectivity of Cu-SSZ-13 in the selective catalytic reduction of NOx with NH3,” *J Catal*, vol. 275, no. 2, pp. 187–190, Oct. 2010.

[51] M. R. Hudson, W. L. Queen, J. A. Mason, D. W. Fickel, R. F. Lobo, and C. M. Brown, “Unconventional, highly selective CO 2 adsorption in zeolite SSZ-13,” *J Am Chem Soc*, vol. 134, no. 4, pp. 1970–1973, Feb. 2012.

[52] S. Prodinger, R. S. Vemuri, T. Varga, B. Peter McGrail, R. K. Motkuri, and M. A. Derewinski, “Impact of chabazite SSZ-13 textural properties and

chemical composition on CO2 adsorption applications," *New Journal of Chemistry*, vol. 40, no. 5, pp. 4375–4385, 2016.

[53] Z. Xu *et al.*, "Size control of SSZ-13 crystals with APAM and its influence on the coking behaviour during MTO reaction," *Catal Sci Technol*, vol. 9, no. 11, pp. 2888–2897, 2019.

[54] F. Bleken *et al.*, "The effect of acid strength on the conversion of methanol to olefins over acidic microporous catalysts with the CHA topology," *Top Catal*, vol. 52, no. 3, pp. 218–228, Apr. 2009.

[55] Q. Li *et al.*, "Rapid synthesis of hierarchical nanosized SSZ-13 zeolite with excellent MTO catalytic performance," *Microporous and Mesoporous Materials*, vol. 331, Jan. 2022.

[56] X. Zhu *et al.*, "Trimodal Porous Hierarchical SSZ-13 Zeolite with Improved Catalytic Performance in the Methanol-to-Olefins Reaction," *ACS Catal*, vol. 6, no. 4, pp. 2163–2177, Apr. 2016.

[57] S. I. Zones, Y. Nakagawa, S. T. Evans, and G. S. Lee, "Zeolite SSZ-39," U. S. Pat. 5,958,370, Sep. 28, 1999.

[58] H. Xu, L. Zhu, Q. Wu, X. Meng, and F. S. Xiao, "Advances in the synthesis and application of the SSZ-39 zeolite," *Inorganic Chemistry Frontiers*, vol. 9, no. 6. Royal Society of Chemistry, pp. 1047–1057, Feb. 09, 2022.

[59] W. Yao, L. Gang-gang, Z. Shao-qing, Z. Xin-yan, Z. Xin, and H. Zheng-ping, "Promoting effect of Ce and Mn addition on Cu-SSZ-39 zeolites for NH3-SCR reaction: Activity, hydrothermal stability, and mechanism study," *Chemical Engineering Journal*, vol. 393, Aug. 2020.

[60] J. Du *et al.*, "Unexpected increase in low-temperature NH3-SCR catalytic activity over Cu-SSZ-39 after hydrothermal aging," *Appl Catal B*, vol. 294, Oct. 2021.

[61] N. Martín, P. N. R. Vennestrøm, J. R. Thøgersen, M. Moliner, and A. Corma, "Iron-Containing SSZ-39 (AEI) Zeolite: An Active and Stable High-Temperature NH3-SCR Catalyst," *ChemCatChem*, vol. 9, no. 10, pp. 1754–1757, May 2017.

[62] M. Dusselier, M. A. Deimund, J. E. Schmidt, and M. E. Davis, "Methanol-to-Olefins Catalysis with Hydrothermally Treated Zeolite SSZ-39," *ACS Catal*, vol. 5, no. 10, pp. 6078–6085, Oct. 2015.

[63] H. Xu *et al.*, "Organosilane surfactant-assisted synthesis of mesoporous SSZ-39 zeolite with enhanced catalytic performance in the methanol-to-olefins reaction," *Front Chem Sci Eng*, vol. 14, no. 2, pp. 267–274, Apr. 2020.

[64] S. Narayanan, P. Tamizhdurai, V. L. Mangesh, C. Ragupathi, P. Santhana krishnan, and A. Ramesh, "Recent advances in the synthesis and applications of mordenite zeolite - review," *RSC Advances*, vol. 11, no. 1. Royal Society of Chemistry, pp. 250–267, Nov. 23, 2020.

[65] P. Vanelderen *et al.*, "Spectroscopic definition of the copper active sites in mordenite: Selective methane oxidation," *J Am Chem Soc*, vol. 137, no. 19, pp. 6383–6392, May 2015.

[66] I. Georgieva, L. Benco, D. Tunega, N. Trendafilova, J. Hafner, and H. Lischka, "Multiple adsorption of NO on cobalt-exchanged chabazite, mordenite, and ferrierite zeolites: A periodic density functional theory study," *Journal of Chemical Physics*, vol. 131, no. 5, 2009.

[67] M. D. Smolikov *et al.*, "Effect of the zeolite modulus of Pt/MOR/Al2O3 catalysts on the n-heptane isomerization reaction," *Catal Ind*, vol. 8, no. 2, pp. 121–127, Apr. 2016.

[68] O. v. Dzhikiya *et al.*, "A study of fluorine-containing catalysts based on MOR and BEA zeolites in isomerization of n-hexane," in *AIP Conference Proceedings*, Nov. 2020, vol. 2285.

[69] Y. Li *et al.*, “Template-induced Al distribution in MOR and enhanced activity in dimethyl ether carbonylation,” *Physical Chemistry Chemical Physics*, vol. 22, no. 20, pp. 11374–11381, May 2020.

[70] Z. Cheng *et al.*, “Role of bronsted acid sites within 8-MR of mordenite in the deactivation roadmap for dimethyl ether carbonylation,” *ACS Catal*, vol. 11, no. 9, pp. 5647–5657, May 2021.

[71] K. Góra-Marek *et al.*, “Hierarchical mordenite dedicated to the fluid catalytic cracking process: Catalytic performance regarding textural and acidic properties,” *Journal of Physical Chemistry C*, vol. 118, no. 48, pp. 28043–28054, Dec. 2014.

[72] G. A. Nasser *et al.*, “Cracking of n-hexane over hierarchical MOR zeolites derived from natural minerals,” *J Taiwan Inst Chem Eng*, vol. 61, pp. 20–25, Jun. 2015.

[73] Y. Liu *et al.*, “Isomerization of α-pinene with a hierarchical mordenite molecular sieve prepared by the microwave assisted alkaline treatment,” *Microporous and Mesoporous Materials*, vol. 299, Jun. 2020.

[74] X. Wang, R. Li, C. Yu, L. Zhang, C. Xu, and H. Zhou, “Dimethyl ether carbonylation over nanosheet-assembled hierarchical mordenite,” *Microporous and Mesoporous Materials*, vol. 274, pp. 227–235, Jan. 2019.

[75] S. Liu *et al.*, “Improved Catalytic Performance in Dimethyl Ether Carbonylation over Hierarchical Mordenite by Enhancing Mass Transfer,” *Ind Eng Chem Res*, vol. 59, no. 31, pp. 13861–13869, Aug. 2020.

[76] H. Sheng, W. Qian, H. Zhang, P. Zhao, H. Ma, and W. Ying, “Synthesis of hierarchical porous H-mordenite zeolite for carbonylation of dimethyl ether,” *Microporous and Mesoporous Materials*, vol. 295, Mar. 2020.

[77] G. J. Gomes, M. B. Costa, P. R. S. Bittencourt, M. F. Zalazar, and P. A. Arroyo, “Catalytic improvement of biomass conversion: Effect of adding

mesoporosity on MOR zeolite for esterification with oleic acid,” *Renew Energy*, vol. 178, pp. 1–12, Nov. 2021.

[78] Y. Wei, P. E. de Jongh, M. L. M. Bonati, D. J. Law, G. J. Sunley, and K. P. de Jong, “Enhanced catalytic performance of zeolite ZSM-5 for conversion of methanol to dimethyl ether by combining alkaline treatment and partial activation,” *Appl Catal A Gen*, vol. 504, pp. 211–219, Sep. 2015.

[79] J. Dedecek, V. Balgová, V. Pashkova, P. Klein, and B. Wichterlová, “Synthesis of ZSM-5 zeolites with defined distribution of Al atoms in the framework and multinuclear MAS NMR analysis of the control of Al distribution,” *Chemistry of Materials*, vol. 24, no. 16, pp. 3231–3239, Aug. 2012.

[80] J. Dědeček, Z. Sobalík, and B. Wichterlová, “Siting and Distribution of Framework Aluminium Atoms in Silicon-Rich Zeolites and Impact on Catalysis,” *Catalysis Reviews - Science and Engineering*, vol. 54, no. 2. pp. 135–223, Apr. 01, 2012.

[81] J. Li, S. Liu, H. Zhang, E. Lü, P. Ren, and J. Ren, “Synthesis and characterization of an unusual snowflake-shaped ZSM-5 zeolite with high catalytic performance in the methanol to olefin reaction,” *Cuihua Xuebao/Chinese Journal of Catalysis*, vol. 37, no. 2, pp. 308–315, Feb. 2016.

[82] T. Weissenberger *et al.*, “Hierarchical ZSM-5 Catalysts: The Effect of Different Intracrystalline Pore Dimensions on Catalyst Deactivation Behaviour in the MTO Reaction,” *ChemCatChem*, vol. 12, no. 9, pp. 2461–2468, May 2020.

[83] F. Mohammadparast, R. Halladj, and S. Askari, “The Crystal Size Effect of Nano-Sized ZSM-5 in the Catalytic Performance of Petrochemical Processes: A Review,” *Chemical Engineering Communications*, vol. 202, no. 4. Taylor and Francis Ltd., pp. 542–556, May 01, 2015.

[84] Y. Ji, H. Yang, and W. Yan, “Strategies to enhance the catalytic performance of ZSM-5 zeolite in hydrocarbon cracking: A review,” *Catalysts*, vol. 7, no. 12. MDPI, Dec. 01, 2017.

[85] N. Rahimi and R. Karimzadeh, “Catalytic cracking of hydrocarbons over modified ZSM-5 zeolites to produce light olefins: A review,” *Applied Catalysis A: General*, vol. 398, no. 1–2. pp. 1–17, May 15, 2011.

[86] F. Mohammadparast, R. Halladj, and S. Askari, “The Crystal Size Effect of Nano-Sized ZSM-5 in the Catalytic Performance of Petrochemical Processes: A Review,” *Chemical Engineering Communications*, vol. 202, no. 4. Taylor and Francis Ltd., pp. 542–556, May 01, 2015.

[87] P. A. Vaughan, “The Crystal Structure of the Zeolite Ferrierite,” 1966.

[88] H. Hu *et al.*, “Designing ferrierite-based catalysts with improved properties for skeletal isomerization of n -butene to isobutene,” *RSC Adv*, vol. 7, no. 50, pp. 31535–31543, 2017.

[89] H. Abrevaya, “Cracking of naphtha range alkanes and naphthenes over zeolites,” 2007.

[90] Z. Fang *et al.*, “Selective mild oxidation of methane to methanol or formic acid on Fe-MOR catalysts,” *Catal Sci Technol*, vol. 9, no. 24, pp. 6946–6956, 2019.

[91] M. H. Groothaert, P. J. Smeets, B. F. Sels, P. A. Jacobs, and R. A. Schoonheydt, “Selective oxidation of methane by the bis(μ-oxo)dicopper core stabilized on ZSM-5 and mordenite zeolites,” *J Am Chem Soc*, vol. 127, no. 5, pp. 1394–1395, Feb. 2005.

[92] K. Narsimhan, K. Iyoki, K. Dinh, and Y. Román-Leshkov, “Catalytic oxidation of methane into methanol over copper-exchanged zeolites with oxygen at low temperature,” *ACS Cent Sci*, vol. 2, no. 6, pp. 424–429, Jun. 2016.

[93] T. Sheppard, C. D. Hamill, A. Goguet, D. W. Rooney, and J. M. Thompson, “A low temperature, isothermal gas-phase system for conversion of methane to methanol over Cu-ZSM-5,” *Chemical Communications*, vol. 50, no. 75, pp. 11053–11055, Aug. 2014.

[94] B. Ipek and R. F. Lobo, “Catalytic conversion of methane to methanol on Cu-SSZ-13 using N2O as oxidant,” *Chem Comm*, no. 300, pp. 13401–13404, 2016.

[95] M. B. Park, E. D. Park, and W. S. Ahn, “Recent progress in direct conversion of methane to methanol over copper-exchanged zeolites,” *Frontiers in Chemistry*, vol. 7. Frontiers Media S.A., pp. 1–7, 2019.

[96] M. J. Wulfers, S. Teketel, B. Ipek, and R. F. Lobo, “Conversion of methane to methanol on copper-containing small-pore zeolites and zeotypes,” *Chemical Communications*, vol. 51, no. 21, pp. 4447–4450, Mar. 2015.

[97] M. B. Park, S. H. Ahn, A. Mansouri, M. Ranocchiari, and J. A. van Bokhoven, “Comparative Study of Diverse Copper Zeolites for the Conversion of Methane into Methanol,” *ChemCatChem*, vol. 9, no. 19, pp. 3705–3713, Oct. 2017.

[98] S. H. Lee, J. K. Kang, and E. D. Park, “Continuous methanol synthesis directly from methane and steam over Cu(II)-exchanged mordenite,” *Korean Journal of Chemical Engineering*, vol. 35, no. 11, pp. 2145–2149, Nov. 2018.

[99] E. Mae Alayon, M. Nachtegaal, M. Ranocchiari, and J. A. van Bokhoven, “Catalytic conversion of methane to methanol over Cu-mordenite,” *Chemical Communications*, vol. 48, no. 3, pp. 404–406, Dec. 2012.

[100] D. K. Pappas *et al.*, “The Nuclearity of the Active Site for Methane to Methanol Conversion in Cu-Mordenite: A Quantitative Assessment,” *J Am Chem Soc*, vol. 140, no. 45, pp. 15270–15278, Nov. 2018.

[101] D. K. Pappas *et al.*, “Methane to Methanol: Structure-Activity Relationships for Cu-CHA,” *J Am Chem Soc*, vol. 139, no. 42, pp. 14961–14975, Oct. 2017.

[102] D. K. Pappas *et al.*, “Understanding and Optimizing the Performance of Cu-FER for The Direct CH4 to CH3OH Conversion,” *ChemCatChem*, vol. 11, no. 1, pp. 621–627, Jan. 2019.

[103] A. R. Kulkarni, Z. J. Zhao, S. Siahrostami, J. K. Nørskov, and F. Studt, “Monocopper Active Site for Partial Methane Oxidation in Cu-Exchanged 8MR Zeolites,” *ACS Catal*, vol. 6, no. 10, pp. 6531–6536, Oct. 2016.

[104] K. T. Dinh *et al.*, “Continuous Partial Oxidation of Methane to Methanol Catalyzed by Diffusion-Paired Copper Dimers in Copper-Exchanged Zeolites,” *J Am Chem Soc*, vol. 141, no. 29, pp. 11641–11650, Jul. 2019.

[105] J. Xu *et al.*, “Continuous selective oxidation of methane to methanol over Cu- and Fe-modified ZSM-5 catalysts in a flow reactor,” *Catal Today*, vol. 270, pp. 93–100, Jul. 2016.

[106] C. Kalamaras, D. Palomas, R. Bos, A. Horton, M. Crimmin, and K. Hellgardt, “Selective Oxidation of Methane to Methanol over Cu- And Fe-Exchanged Zeolites: The Effect of Si/Al Molar Ratio,” *Catal Letters*, vol. 146, no. 2, pp. 483–492, Feb. 2016.

[107] C. Hammond *et al.*, “Catalytic and mechanistic insights of the low-temperature selective oxidation of methane over Cu-promoted Fe-ZSM-5,” *Chemistry - A European Journal*, vol. 18, no. 49, pp. 15735–15745, Dec. 2012.

[108] O. Memioglu and B. Ipek, “A potential catalyst for continuous methane partial oxidation to methanol using,” pp. 1364–1367, 2021.

[109] C. Hammond *et al.*, “Direct Catalytic Conversion of Methane to Methanol in an Aqueous Medium by using Copper-Promoted Fe-ZSM-5,” *Angewandte Chemie*, vol. 124, no. 21, pp. 5219–5223, May 2012.

[110] V. I. Sobolev, G. I. Panov, A. S. Kharitonov, V. N. Romannikov, A. M. Volodin, and K. G. Ione, “Catalytic Properties of ZSM-5 Zeolites in N2O Decomposition: The Role of Iron,” *J Catal*, vol. 139, no. 2, pp. 435–443, 1993.

[111] E. v Starokon, K. A. Dubkov, G. I. Panov, L. v Pirutko, and G. I. Panov, “Mechanisms of Iron Activation on Fe-Containing Zeolites and the Charge of α-Oxygen Mechanisms of iron activation on Fe-containing zeolites and the charge of-oxygen,” *Top Catal*, vol. 23, no. 1/4, pp. 137–143, 2003.

[112] C. Hammond *et al.*, “Aqueous-phase methane oxidation over Fe-MFI zeolites; Promotion through isomorphous framework substitution,” *ACS Catal*, vol. 3, no. 8, pp. 1835–1844, Aug. 2013.

[113] C. Hammond *et al.*, “Elucidation and evolution of the active component within Cu/Fe/ZSM-5 for catalytic methane oxidation: From synthesis to catalysis,” *ACS Catal*, vol. 3, no. 4, pp. 689–699, Apr. 2013.

[114] M. S. Kim and E. D. Park, “Aqueous-phase partial oxidation of methane with H2O2 over Fe-ZSM-5 catalysts prepared from different iron precursors,” *Microporous and Mesoporous Materials*, vol. 324, Sep. 2021.

[115] A. Oda *et al.*, “Rational design of ZSM-5 zeolite containing a high concentration of single Fe sites capable of catalyzing the partial oxidation of methane with high turnover frequency,” *Catal Sci Technol*, vol. 12, no. 2, pp. 542–550, Jan. 2022.

[116] M. S. Kim, K. H. Park, S. J. Cho, and E. D. Park, “Partial oxidation of methane with hydrogen peroxide over Fe-ZSM-5 catalyst,” *Catal Today*, vol. 376, pp. 113–118, Sep. 2021.

[117] T. Yu *et al.*, “Identifying key mononuclear Fe species for low-temperature methane oxidation,” *Chem Sci*, vol. 12, no. 9, pp. 3152–3160, Mar. 2021.

[118] M. Shahami and D. F. Shantz, “Zeolite acidity strongly influences hydrogen peroxide activation and oxygenate selectivity in the partial oxidation of methane over M,Fe-MFI (M: Ga, Al, B) zeolites,” *Catal Sci Technol*, vol. 9, no. 11, pp. 2945–2951, 2019.

[119] C. Xu, Q. Song, N. Merdanoglu, H. Liu, and E. Klemm, “Identifying Monomeric Fe Species for Efficient Direct Methane Oxidation to C1 Oxygenates with H2O2 over Fe/MOR Catalysts,” *Methane*, vol. 1, no. 2, pp. 107–124, May 2022.

[120] V. Pashkova, P. Klein, J. Dedecek, V. Tokarová, and B. Wichterlová, “Incorporation of Al at ZSM-5 hydrothermal synthesis. Tuning of Al pairs in the framework,” *Microporous and Mesoporous Materials*, vol. 202, no. C, pp. 138–146, Jan. 2015.

[121] V. I. Sobolev, K. A. Dubkov, O. v Panna, and G. I. Panov, “Selective oxidation of methane to methanol on a FeZSM-5 surface,” 1995.

[122] G. I. Panov *et al.*, “IRON COMPLEXES IN ZEOLITES AS A NEW MODEL OF METHANE MONOOXYGENASE,” *React. Kinet.Catal.Lett.*, vol. 61, no. 2, pp. 251–258, 1997.

[123] E. v. Starokon, M. v. Parfenov, L. v. Pirutko, S. I. Abornev, and G. I. Panov, “Room-temperature oxidation of methane by α-oxygen and extraction of products from the FeZSM-5 surface,” *Journal of Physical Chemistry C*, vol. 115, no. 5, pp. 2155–2161, 2011.

[124] E. v. Starokon, M. v. Parfenov, S. S. Arzumanov, L. v. Pirutko, A. G. Stepanov, and G. I. Panov, “Oxidation of methane to methanol on the surface of FeZSM-5 zeolite,” *J Catal*, vol. 300, pp. 47–54, 2013.

[125] M. L. Bols *et al.*, “Spectroscopic Identification of the α-Fe/α-O Active Site in Fe-CHA Zeolite for the Low-Temperature Activation of the Methane C-H Bond,” *J Am Chem Soc*, vol. 140, no. 38, pp. 12021–12032, 2018.

[126] M. L. Bols *et al.*, “Selective Formation of α-Fe(II) Sites on Fe-Zeolites through One-Pot Synthesis,” *J Am Chem Soc*, vol. 143, no. 39, pp. 16243–16255, Oct. 2021.

[127] M. v. Parfenov, E. v. Starokon, L. v. Pirutko, and G. I. Panov, “Quasicatalytic and catalytic oxidation of methane to methanol by nitrous oxide over FeZSM-5 zeolite,” *J Catal*, vol. 318, pp. 14–21, 2014.

[128] Y. K. Chow *et al.*, “Investigating the influence of acid sites in continuous methane oxidation with N2O over Fe/MFI zeolites,” *Catal Sci Technol*, vol. 8, no. 1, pp. 154–163, 2018.

[129] G. Zhao, E. Benhelal, A. Adesina, E. Kennedy, and M. Stockenhuber, “Comparison of Direct, Selective Oxidation of Methane by N2O over Fe-ZSM-5, Fe-Beta, and Fe-FER Catalysts,” *Journal of Physical Chemistry C*, vol. 123, no. 45, pp. 27436–27447, Nov. 2019.

[130] Y. K. Chow *et al.*, “A Kinetic Study of Methane Partial Oxidation over Fe-ZSM-5 Using N2O as an Oxidant,” *ChemPhysChem*, vol. 19, no. 4, pp. 402–411, 2018.

[131] K. S. Park *et al.*, “Direct activation of CH4 to oxygenates and unsaturated hydrocarbons using N2O on Fe-modified zeolites,” *J Mol Catal A Chem*, vol. 426, pp. 130–140, Jan. 2017.

[132] Y. Li *et al.*, “Synergistic effect of neighboring fe and cu cation sites boosts fencum-bea activity for the continuous direct oxidation of methane to methanol,” *Catalysts*, vol. 11, no. 12, Dec. 2021.

[133] S. Li, L. Fan, L. Song, D. Cheng, and F. Chen, “Influence of extra-framework Al in Fe-MOR catalysts for the direct conversion of methane to oxygenates by nitrous oxide,” *Chin J Chem Eng*, vol. 33, pp. 132–138, May 2021.

[134] S. S. Ndlela, H. B. Friedrich, and M. N. Cele, “Effects of framework disruption of ga and ba containing zeolitic materials by thermal treatment,” *Catalysts*, vol. 10, no. 9, Sep. 2020.

[135] A. P. E. York, T. Xiao, and M. L. H. Green, “Brief overview of the partial oxidation of methane to synthesis gas,” *Top Catal*, vol. 22, no. 3–4, pp. 345–358, Apr. 2003.

[136] B. R. Wood, J. A. Reimer, A. T. Bell, M. T. Janicke, and K. C. Ott, “Methanol formation on Fe/Al-MFI via the oxidation of methane by nitrous oxide,” *J Catal*, vol. 225, no. 2, pp. 300–306, Jul. 2004.

[137] R. Xu *et al.*, “H2O-Built Proton Transfer Bridge Enhances Continuous Methane Oxidation to Methanol over Cu-BEA Zeolite,” *Angewandte Chemie - International Edition*, vol. 60, no. 30, pp. 16634–16640, Jul. 2021.

[138] G. Zhao, K. Chodyko, E. Benhelal, A. Adesina, E. Kennedy, and M. Stockenhuber, “Methane oxidation by N2O over Fe-FER catalysts prepared by different methods: Nature of active iron species, stability of surface oxygen species and selectivity to products,” *J Catal*, vol. 400, pp. 10–19, Aug. 2021.

[139] J. Wang, H. Xia, X. Ju, Z. Feng, F. Fan, and C. Li, “Influence of extra-framework Al on the structure of the active iron sites in Fe/ZSM-35,” *J Catal*, vol. 300, pp. 251–259, Apr. 2013.

[140] B. E. R. Snyder *et al.*, “The active site of low-temperature methane hydroxylation in iron-containing zeolites,” *Nature*, vol. 536, no. 7616, pp. 317–321, Aug. 2016.

[141] K. A. Dubkov, N. S. Ovanesyan, A. A. Shteinman, E. v. Starokon, and G. I. Panov, “Evolution of iron states and formation of α-sites upon activation of FeZSM-5 zeolites,” *J Catal*, vol. 207, no. 2, pp. 341–352, 2002.

[142] G. Zhao, A. Adesina, E. Kennedy, and M. Stockenhuber, “Formation of Surface Oxygen Species and the Conversion of Methane to Value-Added

Products with N2O as Oxidant over Fe-Ferrierite Catalysts," *ACS Catal*, vol. 10, no. 2, pp. 1406–1416, Jan. 2020.

[143] G. I. Panov, G. A. Sheveleva, A. S. Kharitonov, V. N. Romannikov, and L. A. Vostrikova, "Oxidation of benzene to phenol by nitrous oxide over Fe-ZSM-5 zeolites," *Appl Catal A Gen*, vol. 82, pp. 31–36, 1992.

[144] K. Jíša, J. Nováková, M. Schwarze, A. Vondrová, S. Sklenák, and Z. Sobalik, "Role of the Fe-zeolite structure and iron state in the N2O decomposition: Comparison of Fe-FER, Fe-BEA, and Fe-MFI catalysts," *J Catal*, vol. 262, no. 1, pp. 27–34, Feb. 2009.

[145] S. Sklenak *et al.*, "N2O decomposition over Fe-zeolites: Structure of the active sites and the origin of the distinct reactivity of Fe-ferrierite, Fe-ZSM-5, and Fe-beta. A combined periodic DFT and multispectral study," *J Catal*, vol. 272, no. 2, pp. 262–274, Jun. 2010.

[146] M. H. Mahyuddin, A. Staykov, Y. Shiota, and K. Yoshizawa, "Direct Conversion of Methane to Methanol by Metal-Exchanged ZSM-5 Zeolite (Metal = Fe, Co, Ni, Cu)," *ACS Catal*, vol. 6, no. 12, pp. 8321–8331, Dec. 2016.

[147] F. Göltl *et al.*, "Computationally Exploring Confinement Effects in the Methane-to-Methanol Conversion over Iron-Oxo Centers in Zeolites," *ACS Catal*, vol. 6, no. 12, pp. 8404–8409, Dec. 2016.

[148] M. H. Mahyuddin, Y. Shiota, A. Staykov, and K. Yoshizawa, "Theoretical Investigation of Methane Hydroxylation over Isoelectronic [FeO]2+- and [MnO]+-Exchanged Zeolites Activated by N2O," *Inorg Chem*, vol. 56, no. 17, pp. 10370–10380, Sep. 2017.

[149] M. H. Mahyuddin, T. Tanaka, Y. Shiota, A. Staykov, and K. Yoshizawa, "Methane Partial Oxidation over [Cu2(μ-O)]2+ and [Cu3(μ-O)3]2+ Active Species in Large-Pore Zeolites," *ACS Catal*, vol. 8, no. 2, pp. 1500–1509, Feb. 2018.

[150] K. Liu, A. I. Rykov, J. Wang, and T. Zhang, “Recent advances in the application of Möβbauer spectroscopy in heterogeneous catalysis,” in *Advances in Catalysis*, vol. 58, Academic Press Inc., 2015, pp. 1–142.

[151] M. L. Bols *et al.*, “Coordination and activation of nitrous oxide by iron zeolites,” *Nat Catal*, vol. 4, no. 4, pp. 332–340, Apr. 2021.

[152] S. D. Hallaert, M. L. Bols, P. Vanelderen, R. A. Schoonheydt, B. F. Sels, and K. Pierloot, “Identification of α-Fe in High-Silica Zeolites on the Basis of ab Initio Electronic Structure Calculations,” *Inorg Chem*, vol. 56, no. 17, pp. 10681–10690, Sep. 2017.

[153] T. D. Pham, Q. Liu, and R. F. Lobo, “Carbon dioxide and nitrogen adsorption on cation-exchanged SSZ-13 zeolites,” *Langmuir*, vol. 29, no. 2, pp. 832–839, 2013.

[154] B. Ipek *et al.*, “Formation of [Cu2O2]2+ and [Cu2O]2+ toward C-H Bond Activation in Cu-SSZ-13 and Cu-SSZ-39,” *ACS Catal*, vol. 7, no. 7, pp. 4291–4303, 2017.

[155] Z. Li, M. T. Navarro, J. Martínez-Triguero, J. Yu, and A. Corma, “Synthesis of nano-SSZ-13 and its application in the reaction of methanol to olefins,” *Catal Sci Technol*, vol. 6, no. 15, pp. 5856–5863, 2016.

[156] K. Leng, Y. Sun, X. Zhang, M. Yu, and W. Xu, “Ti-modified hierarchical mordenite as highly active catalyst for oxidative desulfurization of dibenzothiophene,” *Fuel*, vol. 174, pp. 9–16, 2016.

[157] N. Martín, P. N. R. Vennestrøm, J. R. Thøgersen, M. Moliner, and A. Corma, “Iron-Containing SSZ-39 (AEI) Zeolite: An Active and Stable High-Temperature NH3-SCR Catalyst,” *ChemCatChem*, vol. 9, no. 10, pp. 1754–1757, May 2017.

[158] A. Palčić *et al.*, “Nanosized CU-SSZ-13 and its application in NH3-SCR,” *Catalysts*, vol. 10, no. 5, May 2020.

[159] M. Ravi, V. L. Sushkevich, and J. A. van Bokhoven, “On the location of Lewis acidic aluminum in zeolite mordenite and the role of framework-associated aluminum in mediating the switch between Brønsted and Lewis acidity,” *Chem Sci*, vol. 12, no. 11, pp. 4094–4103, Mar. 2021.

[160] J. Goetze, I. Yarulina, J. Gascon, F. Kapteijn, and B. M. Weckhuysen, “Revealing Lattice Expansion of Small-Pore Zeolite Catalysts during the Methanol-to-Olefins Process Using Combined Operando X-ray Diffraction and UV-vis Spectroscopy,” *ACS Catal*, vol. 8, no. 3, pp. 2060–2070, Mar. 2018.

[161] J. R. di Iorio and R. Gounder, “Controlling the Isolation and Pairing of Aluminum in Chabazite Zeolites Using Mixtures of Organic and Inorganic Structure-Directing Agents,” *Chemistry of Materials*, vol. 28, no. 7, pp. 2236–2247, Apr. 2016.

[162] M. A. Deimund *et al.*, “Effect of Heteroatom Concentration in SSZ-13 on the Methanol-to-Olefins Reaction,” *ACS Catal*, vol. 6, no. 2, pp. 542–550, Feb. 2016.

[163] J. Y. Lim, J. McGregor, A. J. Sederman, and J. S. Dennis, “The role of the Boudouard and water–gas shift reactions in the methanation of CO or CO2 over Ni/γ-Al2O3 catalyst,” *Chem Eng Sci*, vol. 152, pp. 754–766, Oct. 2016.

[164] P. Losch *et al.*, “H-ZSM-5 zeolite model crystals: Structure-diffusion-activity relationship in methanol-to-olefins catalysis,” *J Catal*, vol. 345, pp. 11–23, Jan. 2017.

[165] G. Seo, J. H. Kim, and H. G. Jang, “Methanol-to-Olefin Conversion over Zeolite Catalysts: Active Intermediates and Deactivation,” *Catalysis Surveys from Asia*, vol. 17, no. 3–4. pp. 103–118, Dec. 2013.

[166] I. Yarulina, A. D. Chowdhury, F. Meirer, B. M. Weckhuysen, and J. Gascon, “Recent trends and fundamental insights in the methanol-to-hydrocarbons

process," *Nature Catalysis,* vol. 1, no. 6. Nature Publishing Group, pp. 398–411, Jun. 01, 2018.

[167] P. Sazama *et al.*, "FTIR and 27Al MAS NMR analysis of the effect of framework Al- and Si-defects in micro- and micro-mesoporous H-ZSM-5 on conversion of methanol to hydrocarbons," *Microporous and Mesoporous Materials,* vol. 143, no. 1, pp. 87–96, Aug. 2011.

[168] K. Barbera, F. Bonino, S. Bordiga, T. V. W. Janssens, and P. Beato, "Structure-deactivation relationship for ZSM-5 catalysts governed by framework defects," *J Catal*, vol. 280, no. 2, pp. 196–205, Jun. 2011.

[169] M. He, J. Zhang, X. L. Sun, B. H. Chen, and Y. G. Wang, "Theoretical Study on Methane Oxidation Catalyzed by Fe/ZSM-5: The Significant Role of Water on Binuclear Iron Active Sites," *Journal of Physical Chemistry C*, vol. 120, no. 48, pp. 27422–27429, Dec. 2016.

APPENDICES

A. Thermodynamic Analysis

Table A.1 Equilibrium conversion and carbon based selectivity results with no water vapor in feed

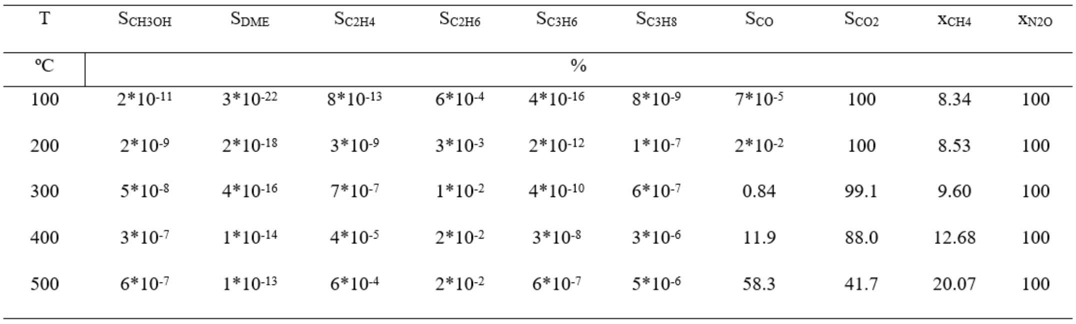

T	S_{CH3OH}	S_{DME}	S_{C2H4}	S_{C2H6}	S_{C3H6}	S_{C3H8}	S_{CO}	S_{CO2}	x_{CH4}	x_{N2O}
℃	%									
100	$2*10^{-11}$	$3*10^{-22}$	$8*10^{-13}$	$6*10^{-4}$	$4*10^{-16}$	$8*10^{-9}$	$7*10^{-5}$	100	8.34	100
200	$2*10^{-9}$	$2*10^{-18}$	$3*10^{-9}$	$3*10^{-3}$	$2*10^{-12}$	$1*10^{-7}$	$2*10^{-2}$	100	8.53	100
300	$5*10^{-8}$	$4*10^{-16}$	$7*10^{-7}$	$1*10^{-2}$	$4*10^{-10}$	$6*10^{-7}$	0.84	99.1	9.60	100
400	$3*10^{-7}$	$1*10^{-14}$	$4*10^{-5}$	$2*10^{-2}$	$3*10^{-8}$	$3*10^{-6}$	11.9	88.0	12.68	100
500	$6*10^{-7}$	$1*10^{-13}$	$6*10^{-4}$	$2*10^{-2}$	$6*10^{-7}$	$5*10^{-6}$	58.3	41.7	20.07	100

Table A. 2 Equilibrium conversion and carbon based selectivity results with 24% water vapor in feed

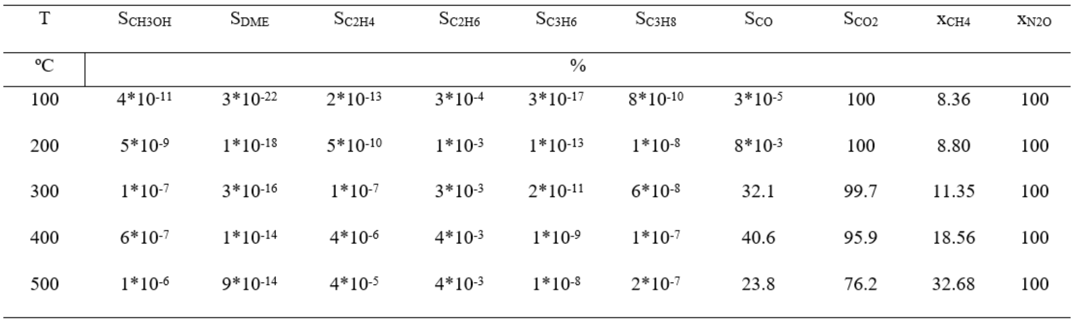

T	S_{CH3OH}	S_{DME}	S_{C2H4}	S_{C2H6}	S_{C3H6}	S_{C3H8}	S_{CO}	S_{CO2}	x_{CH4}	x_{N2O}
℃	%									
100	$4*10^{-11}$	$3*10^{-22}$	$2*10^{-13}$	$3*10^{-4}$	$3*10^{-17}$	$8*10^{-10}$	$3*10^{-5}$	100	8.36	100
200	$5*10^{-9}$	$1*10^{-18}$	$5*10^{-10}$	$1*10^{-3}$	$1*10^{-13}$	$1*10^{-8}$	$8*10^{-3}$	100	8.80	100
300	$1*10^{-7}$	$3*10^{-16}$	$1*10^{-7}$	$3*10^{-3}$	$2*10^{-11}$	$6*10^{-8}$	32.1	99.7	11.35	100
400	$6*10^{-7}$	$1*10^{-14}$	$4*10^{-6}$	$4*10^{-3}$	$1*10^{-9}$	$1*10^{-7}$	40.6	95.9	18.56	100
500	$1*10^{-6}$	$9*10^{-14}$	$4*10^{-5}$	$4*10^{-3}$	$1*10^{-8}$	$2*10^{-7}$	23.8	76.2	32.68	100

B. Experimental Methods Sample Calculations

In order to determine the required amount of iron salt to achieve target Fe/Al ratio, firstly molecular weight of the zeolite in NH_4^+ or H^+ form is calculated. For commercial zeolites, Si/Al ratio is known and for synthesized zeolites EDX or ICP results are used. For example, for commercial NH_4^+-MOR, Si/Al ratio is 10. Then the molecular formula of NH_4^+-MOR can be expressed as $[NH_4^+]\ (SiO_2)_{10}(AlO_2)$.

$$MW_{Mordenite} = MW_{NH4+} + 10 * MW_{AlO2} + MW_{SiO2}$$

$$MW_{Mordenite} = 18 + 10 * 60.08 + 59 = 677.8\ g\ zeolite/mol$$

Following sample calculation is based on starting Fe/Al of 2.

$$\frac{1\ mol\ zeolite}{677.8\ g\ zeolite} * \frac{1\ mol\ (AlO_2)^-}{1\ mol\ zeolite} * \frac{1\ mol\ Al}{1\ mol\ (AlO_2)^-} * \frac{2\ mol\ Fe}{1\ mol\ Al}$$
$$= 2.95 * 10^{-3}\ \frac{mol\ Fe}{g\ zeolite}$$

$$MW_{FeSO_4.7H_2O} = 278.02\ g/mol$$

$$\frac{2.95 * 10^{-3}\ mol\ Fe}{g\ zeolite} * \frac{1\ mol\ FeSO_4.7H_2O}{1\ mol\ Fe} * \frac{278.02\ g}{1\ mol\ FeSO_4.7H_2O}$$
$$= 0.820\ \frac{g\ FeSO_4.7H_2O}{g\ zeolite}$$

Required amount of $FeSO_4.7H_2O$ is calculated below for 5 grams of NH_4^+-MOR.

$$0.820\ \frac{g\ FeSO_4.7H_2O}{g\ zeolite} * 5\ g\ zeolite = 4.102\ g\ of\ FeSO_4.7H_2O$$

Also, starting iron concentrations in terms of molarity are given in Table 3.1. Calculation of starting iron concentration is given below for iron-exchange of 5 grams of NH_4^+-MOR with starting Fe/Al ratio of 2.

$$\frac{2.95 * 10^{-3}\ \frac{mol\ Fe}{g\ zeolite} * 5\ g\ zeolite}{0.1\ \frac{L\ H_2O}{g\ zeolite} * 5\ g\ zeolite} = 0.0295\ M$$

Calculation of Iron Content

From ICP or EDX results, Si/Al and Fe/Al ratios are calculated for each zeolite. Molecular weight of zeolites are calculated assuming 1 mol of AlO_2 is present.

$$MW_{zeolite} = (Si/Al) * MW_{SiO2} + MW_{AlO2} + (Fe/Al) * MW_{Fe}$$

Sample calculation for Fe-MesoMORnew is given below:

$$Si/Al = 25$$

$$Fe/Al = 0.32$$

$$Na/Al = 0$$

$$MW_{Fe-MesoMORnew} = (25) * 60.08 + 58.98 + (0.32) * 55.85 = 1578.85 \ {}^{g}/_{mol}$$

$$\frac{0.32\, mol\ Fe}{1\, mol\ Al} * \frac{1\, mol\ Al}{1\, mol\ zeolite} * \frac{1\, mol\ zeolite}{1578.85\, g} * \frac{1000\, mmol\ Fe}{1\, mol\ Fe}$$

$$= 0.203\ \frac{mmol\ Fe}{g\ catalyst}$$

C. MTM Reaction Formulas Sample Calculations

Following calculations are based on Fe-MesoMORnew data obtained at 300 ºC with 0.300 g catalyst and 100 sccm total flowrate comprising 30% CH_4, 10% N_2O, 23% H_2O and balance He. The room temperature is measured as 19.1 ºC.

Calculation of methane inlet flowrate:

$$F_{CH4,fed} = \frac{y_{CH4}\left(\frac{kPa}{kPa}\right) * P(Pa) * Q_{inlet\ total}\left(\frac{cm^3}{min}\right) * \frac{60\ min}{1\ h}}{R\left(\frac{Pa * m^3}{\mu mol * K}\right) * T(K) * W_{catalyst}(g)}$$

$$= \frac{\frac{30.3}{101.325} * 101325\ Pa * 100\ \frac{cm^3}{min} * \frac{60\ min}{1\ h}}{8.314\ \frac{Pa * cm^3}{\mu mol * K} * (292.1\ K) * 0.300\ g\ cat}$$

$$= 250337.7\ \frac{\mu mol}{g\ cat * h}$$

Calculation of nitrous oxide inlet flowrate:

$$F_{N2O,fed} = \frac{y_{N2O}\left(\frac{kPa}{kPa}\right) * P(Pa) * Q_{inlet\ total}\left(\frac{cm^3}{min}\right) * \frac{60\ min}{1\ h}}{R\left(\frac{Pa * m^3}{\mu mol * K}\right) * T(K) * W_{catalyst}(g)}$$

$$= \frac{\frac{10.1}{101.325} * 101325\ Pa * 100\ \frac{cm^3}{min} * \frac{60\ min}{1\ h}}{8.314\ \frac{Pa * cm^3}{\mu mol * K} * (292.1\ K) * 0.300\ g\ cat}$$

$$= 83178.3\ \frac{\mu mol}{g\ cat * h}$$

Calculation of nitrogen outlet flowrate:

$$r_{N2} = \frac{Area\ of\ N_2 * RF_{N2}\left(\frac{ppm}{area}\right) * 10^{-6} * P(Pa) * Q_{\,total}\left(\frac{cm^3}{min}\right) * \frac{60\ min}{1\ h}}{R\left(\frac{Pa * cm^3}{\mu mol * K}\right) * T(K) * W_{catalyst}(g)}$$

$$= \frac{62.5 * 8.95 * 10^{-6} * 101325\ Pa * 100\frac{cm^3}{min} * \frac{60\ min}{1\ h}}{8.314\ \frac{Pa * cm^3}{\mu mol * K} * 292.1\ K * 0.300\ g\ cat}$$

$$= 466.8\ \frac{\mu mol}{g\ cat * h}$$

Calculation of methanol formation rate:

$$r_{CH3OH}$$

$$= \frac{Area\ of\ CH_3OH * RF_{CH3OH}\left(\frac{ppm}{area}\right) * 10^{-6} * P(Pa) * Q_{\,total}\left(\frac{cm^3}{min}\right) * \frac{60\ min}{1\ h}}{R\left(\frac{Pa * cm^3}{\mu mol * K}\right) * T(K) * W_{catalyst}(g)}$$

$$= \frac{270.6 * 1.463\frac{ppm}{area} * 10^{-6} * 101325\ Pa * 100\ \frac{cm^3}{min} * \frac{60\ min}{1\ h}}{8.314\ \frac{Pa * cm^3}{\mu mol * K} * 292.1\ K * 0.300\ g\ cat}$$

$$= 330.4\ \frac{\mu mol}{g\ cat * h}$$

Calculation of methane reaction rate:

Methane reaction rate is calculated based on carbon balance. All products average formation rates are multiplied with carbon number and summed together including coke. Products' formation rates are calculated like given in calculation of methanol formation rate.

$$r_{CH4}\left(^{\mu mol}/_{g\ cat * h}\right)$$

$$= r_{CH3OH} + r_{CO} + r_{CO2} + 2 * \left(\sum r_{C2}\right) + 3 * \left(\sum r_{C3}\right) + 4$$

$$* \left(\sum r_{C4}\right) + r_{Coke}$$

$$r_{CH4}\left(^{\mu mol}/_{g\ cat * h}\right) = 330.4 + 343.0 + 2.8 + 2 * (6.2 + 1.9 + 0.4) + 3 * (1.8 + 0) + 4 * (0 + 0 + 0 + 0) + 1.9 = 700.5\ \frac{\mu mol}{g\ cat * h}$$

Calculation of methanol selectivity:

$$S_{CH3OH} = \frac{r_{CH3OH}}{r_{CH4}} * 100\% = \frac{330.4\ \frac{\mu mol}{g\ cat * h}}{700.5\ \frac{\mu mol}{g\ cat * h}} * 100\% = 47.2\%$$

Calculation of methane conversion:

$$X_{CH4} = \frac{r_{CH4}}{F_{CH4,fed}} * 100\% = \frac{700.5\ \frac{\mu mol}{g\ cat * h}}{250337.7\ \frac{\mu mol}{g\ cat * h}} * 100\% = 0.28\%$$

Calculation of nitrous oxide conversion:

$$X_{N2O} = \frac{r_{N2}}{F_{N2O,fed}} * 100\% = \frac{643.0\ \frac{\mu mol}{g\ cat * h}}{83178.3\ \frac{\mu mol}{g\ cat * h}} * 100\% = 0.77\%$$

Calculation of turnover frequency of methanol:

Fe content is determined using ICP or EDX.

$$TOF_{CH3OH}\left(\frac{^{\mu mol}/_{g\ cat * h}}{^{mmol\ Fe}/_{g\ cat * h}}\right) = \frac{r_{CH3OH}}{Fe\ content}$$

$$= \frac{330.4\ \frac{\mu mol}{g\ cat * h}}{0.203\ ^{mmol\ Fe}/_{g\ cat * h}} = 1627.9 \frac{\mu mol}{mmol\ Fe * h}$$

D. Deconvoluted UV–Vis Spectra

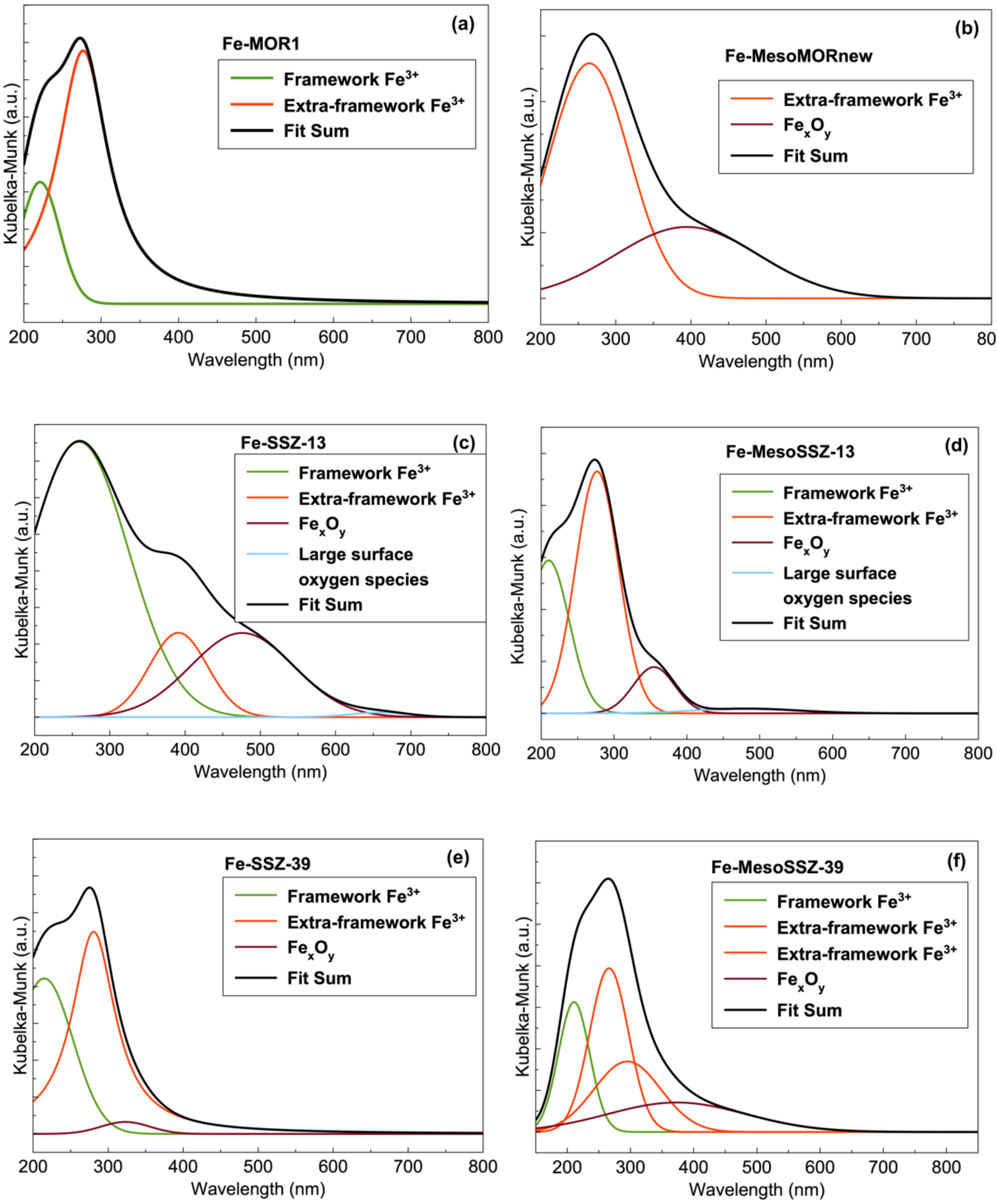

Figure D.1 The deconvolution of UV–Vis spectra for Fe-exchanged zeolites with different framework and porosity (a) Fe-MOR1, (b) Fe-MesoMORnew, (c) Fe-SSZ-13, (d) Fe-MesoSSZ-13, (e) Fe-SSZ-39 and (f) Fe-MesoSSZ-39

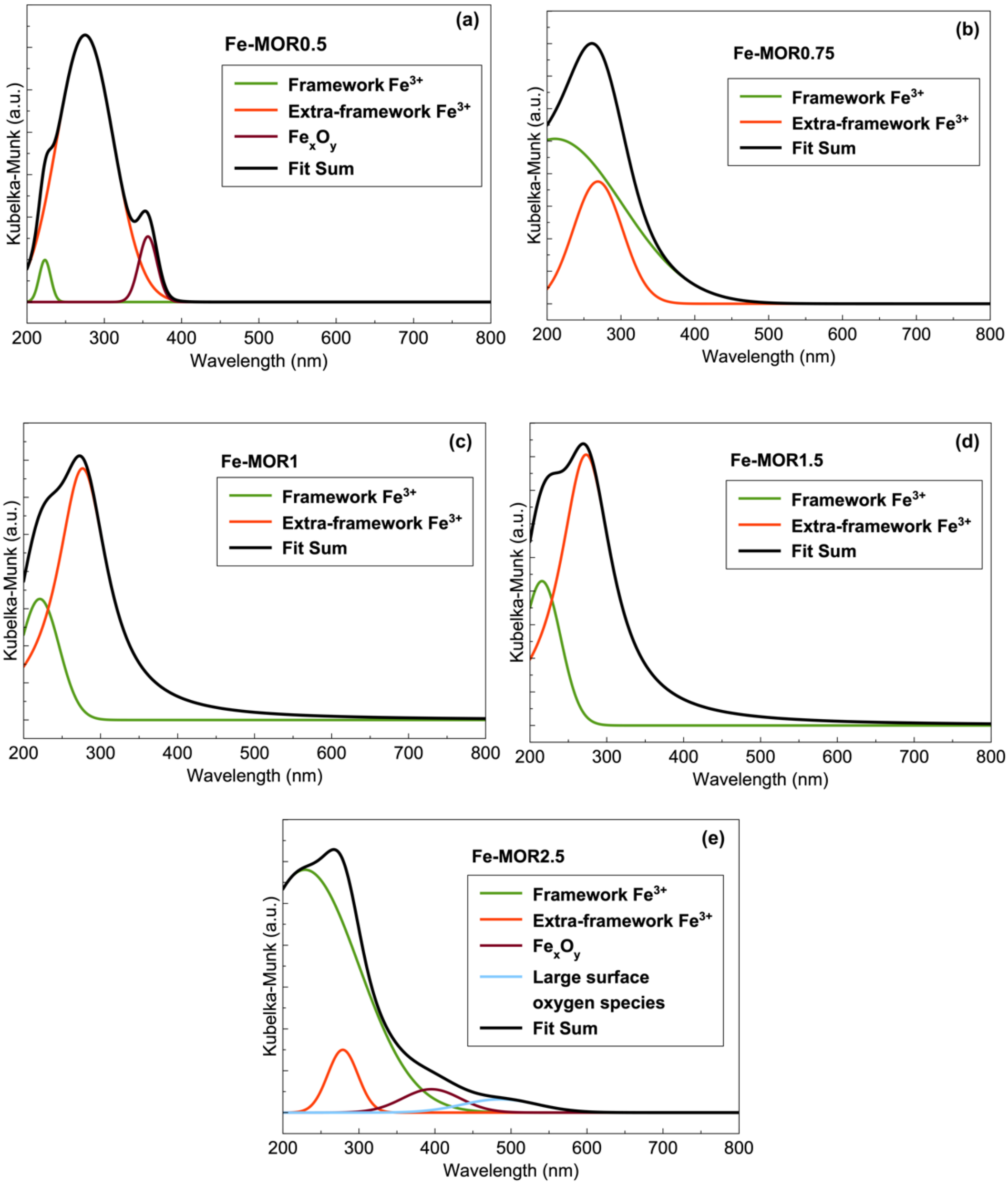

Figure D.2 The deconvoluted UV−Vis spectra of Fe exchanged MOR with various iron content (a) 0.318, (b) 0.319, (c) 0.336, (d) 0.398 and (e) 0.468 mmol Fe/g cat

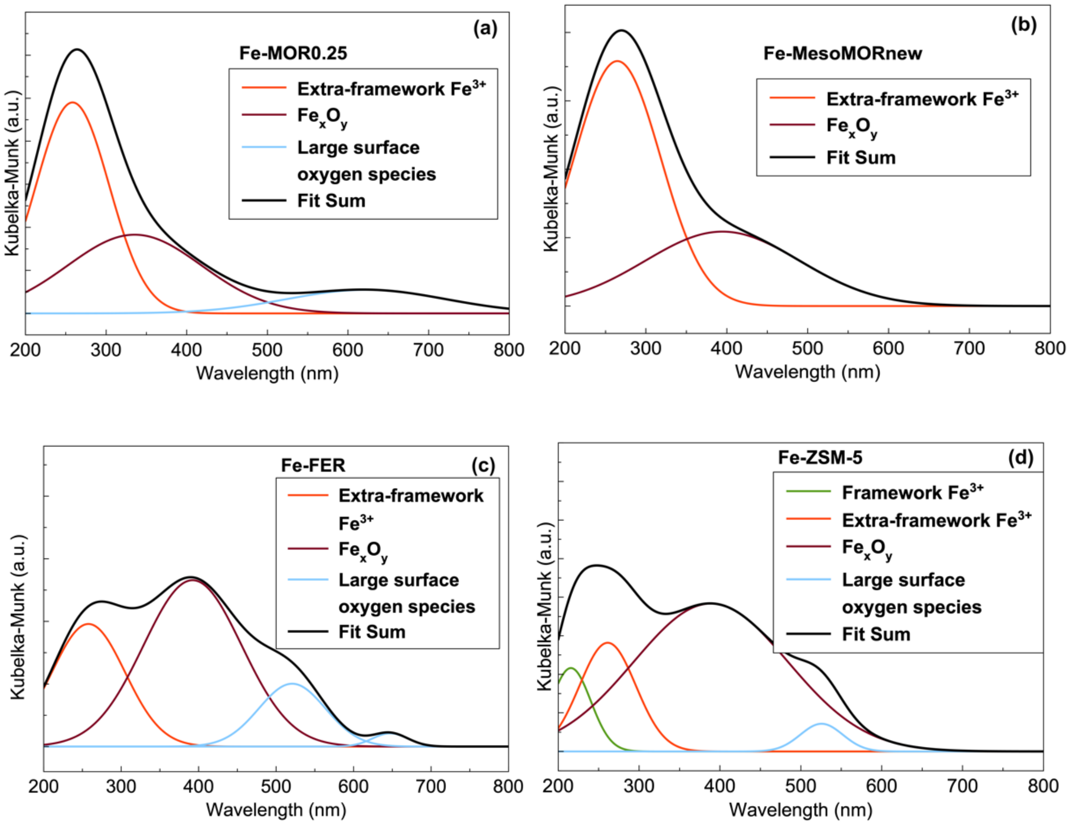

Figure D.3 The deconvoluted UV–Vis spectra of Fe exchanged (a) MOR0.25, (b) MesoMORnew, (c) FER and (d) ZSM-5

E. MTM Reaction Results

Table E.1 Reaction results over iron-exchanged zeolites with different frameworks and mesoporosity (270 ºC, 300 mg catalyst, 50 sccm, 30% CH_4, 30% N_2O, 3% H_2O (balance He))

Fe-zeolites	r_{CH3OH}	r_{DME}	r_{C2H4}	r_{C2H6}	r_{C3H6}	r_{C3H8}	r_{CO}	r_{CO2}	r_{Coke}	TOF CH_3OH	x_{CH4}	x_{N2O}	S_{CH3OH}
	µmol/g/h									µmol/mmol/h	%		
MOR1	62	6	9	0.2	0.09	0.03	1177	92	289	184	1.4	0.7	4
MesoMOR new	148	9	4	0.2	0.2	0.20	192	18	124	731	0.4	0.5	29
SSZ-13	57	7	14	0.4	1.5	0.05	100	5	110	220	0.3	0.2	18
MesoSSZ-13	50	5	29	0.8	5	0.21	80	9	137	292	0.3	0.3	14
SSZ-39	90	13	41	2	8	0.65	751	30	403	311	1.2	0.7	6
MesoSSZ-39	95	17	19	0.8	4	0.20	153	26	242	425	0.5	0.7	16

Table E.2 Reaction results over Fe-MOR samples with different iron content (300 ºC, 300 mg catalyst, 100 sccm,30% CH_4, 10% N_2O, 11−18% H_2O (balance He))

Fe-zeolite	r_{CH3OH}	r_{DME}	r_{C2H4}	r_{C2H6}	r_{C3H6}	r_{C3H8}	r_{CO}	r_{CO2}	r_{Coke}	TOF CH_3OH	x_{CH4}	x_{N2O}	S_{CH3OH}
	µmol/g/h									µmol/mmol/h	%		
NH_4^+-MOR	2	0.1	0	0	4	0.3	0	0	-	-	0.01	0.05	11
MOR0.5	158	1	2	0.4	2	0.05	633	144	121	495	0.44	1.63	15
MOR0.75	333	6	22	0.3	2	0.2	786	49	75	1044	0.53	1.53	25
MOR1	196	5	23	0.5	3	0.3	471	33	114	584	0.37	1.36	22
MOR1.5	289	5	20	0.4	2	0.2	480	42	89	726	0.39	1.43	30
MOR2.5	180	5	20	0.7	1	0.4	817	148	170	384	0.55	3.20	13

Table E.3 Reaction results over Fe-MesoMORnew (300 ºC, 300 mg catalyst, 100 sccm, 20–40% CH_4, 10% N_2O, 11–15% H_2O (balance He))

CH_4	r_{CH3OH}	r_{DME}	r_{C2H4}	r_{C2H6}	r_{C3H6}	r_{C3H8}	r_{CO}	r_{CO2}	r_{Coke}	TOF CH_3OH	x_{CH4}	x_{N2O}	S_{CH3OH}
%	μmol/g/h									μmol/mmol/h	%		
20	62	1	0	0	1	1	37	0	79	307	0.11	0.18	34
30	270	14	7	0.4	1	0.1	335	10	8	1330	0.27	1.31	40
40	204	6	1	0.4	2	0.03	146	0	27	1004	0.12	0.65	51

Table E.4 Reaction results over Fe-MesoMORold (300 °C, 300 mg catalyst, 100 sccm, 30% CH_4, 10–30% N_2O, 8% H_2O (balance He))

N_2O	r_{CH3OH}	r_{DME}	r_{C2H4}	r_{C2H6}	r_{C3H6}	r_{C3H8}	r_{CO}	r_{CO2}	r_{Coke}	TOF CH_3OH	x_{CH4}	x_{N2O}	S_{CH3OH}
%	μmol/g/h									μmol/mmol/h	%		
10	184	9	6	0.3	2	0.2	313	30	31	1143	0.24	1.20	31
20	158	9	4	0.3	2	0.2	344	57	87	986	0.28	0.63	23
30	217	13	8	0.2	2	0.4	661	78	61	1347	0.44	0.72	20

Table E.5 Reaction results over Fe-MesoMORold (300 ºC, 300 mg catalyst, 100 sccm, 30% CH_4, 10% N_2O, 3–15% H_2O (balance He))

H_2O	r_{CH3OH}	r_{DME}	r_{C2H4}	r_{C2H6}	r_{C3H6}	r_{C3H8}	r_{CO}	r_{CO2}	r_{Coke}	TOF CH_3OH	x_{CH4}	x_{N2O}	S_{CH3OH}
%	μmol/g/h									μmol/mmol/h	%		
3	137	14	8	0.2	0.9	0.37	392	46	73	854	0.28	1.48	20
8	184	9	6	0.3	2	0.25	313	30	31	1143	0.24	1.22	31
12	145	6	3	0.3	2	0.09	214	11	17	900	0.17	0.87	35
15	137	3	1	0.2	5	0.05	83	11	20	851	0.11	0.61	50

Table E.6 Reaction results over Fe-MOR0.25 and Fe-MesoMORnew at different temperatures (300–340 ºC, 300 mg catalyst, 100 sccm, 30% CH_4, 10% N_2O, 21–23% H_2O (balance He))

Fe-zeolites	Temp.	r_{CH3OH}	r_{DME}	r_{C2H4}	r_{C2H6}	r_{C3H6}	r_{C3H8}	r_{CO}	r_{CO2}	r_{Coke}	TOF CH_3OH	x_{CH4}	x_{N2O}	S_{CH3OH}
	ºC	µmol/g/h									µmol/mmol/h	%		
MOR	300	325	5	11	0.5	0.9	0.2	442	14	15	1163	0.3	1.1	39
MesoMOR	300	330	6	2	0.4	2	0	343	3	2	1628	0.3	0.8	47
MOR	320	549	11	51	1	2	0.9	1401	111	137	1962	0.9	3.6	24
MesoMOR	320	796	21	19	0.7	1	0.5	735	20	27	3924	0.7	2.3	48
MOR	340	607	9	53	1	2	1.5	3305	291	165	2170	1.8	6.7	13
MesoMOR	340	958	27	50	0.8	0.2	2	28	170	171	4723	0.9	5.4	41
MOR*	300	241	5	33	3	0.6	2	23872	12316	306	863	15	68	0.7
MesoMOR*	300	270	14	7	0.4	1	0.1	335	10	8	1330	0.3	1.3	40

*: water vapor in feed is 11%

Table E.7 Reaction results over Fe-MOR0.25, Fe-MesoMORnew, Fe-FER and Fe-ZSM-5 (300 ºC, 300 mg catalyst, 100 sccm, 30% CH_4, 10% N_2O, 22–24% H_2O (balance He))

Fe-zeolites	Temp.	r_{CH3OH}	r_{DME}	r_{C2H4}	r_{C2H6}	r_{C3H6}	r_{C3H8}	r_{CO}	r_{CO2}	r_{Coke}	TOF CH_3OH	x_{CH4}	x_{N2O}	S_{CH3OH}
	ºC	µmol/g/h									µmol/mmol/h	%		
MOR0.25	300	325	5	11	0.5	0.9	0.2	442	14	15	1163	0.33	1.13	39
MesoMORnew	300	330	6	2	0.4	2	0	343	3	2	1628	0.28	0.77	47
FER	300	581	12	2	0.5	2	0.01	203	0	2	2187	0.33	0.84	71
ZSM-5	300	267	6	9	0	2	2	131	11	92	1953	0.22	0.84	49
MesoMORnew	320	796	21	19	0.7	1	0.5	735	20	27	3924	0.67	2.26	48
FER	320	1219	43	11	1	3	0.51	783	11	7	4590	0.85	2.30	57
MesoMORnew	340	958	27	50	0.8	0.2	2	28	170	171	4723	0.93	5.36	41
FER	340	1648	65	16	3	3	1	956	12	53	6208	1.14	2.78	58

Table E.8 Reaction results over Fe-MOR0.25 at different temperatures (300–340 ºC, 300 mg catalyst, 100 sccm, 30% CH_4, 10% N_2O, 22% H_2O (balance He))

Temp.	r_{CH3OH}	r_{DME}	r_{C2H4}	r_{C2H6}	r_{C3H6}	r_{C3H8}	r_{CO}	r_{CO2}	r_{Coke}	TOF CH_3OH	x_{CH4}	x_{N2O}	S_{CH3OH}
ºC	µmol/g/h									µmol/mmol/h	%		
300	325	5	11	0.5	0.9	0.2	442	14	15	1163	0.33	1.13	39
320	549	11	51	1	2	0.9	1401	111	137	1962	0.93	3.58	24
340	607	9	53	1	2	1.5	3305	291	165	2170	1.82	6.69	13

Table E.9 Reaction results over Fe-MesoMORnew at different temperatures (270–330 ºC, 300 mg catalyst, 100 sccm, 30% CH_4, 10% N_2O, 10–15% H_2O (balance He))

Temp.	r_{CH3OH}	r_{DME}	r_{C2H4}	r_{C2H6}	r_{C3H6}	r_{C3H8}	r_{CO}	r_{CO2}	r_{Coke}	TOF CH_3OH	x_{CH4}	x_{N2O}	S_{CH3OH}
ºC	µmol/g/h									µmol/mmol/h	%		
270	36	0.3	0	0.4	1	0.09	1	5	39	177	0.03	0.14	42
300	234	12	5	0.3	1	0.05	310	10	7	1151	0.24	1.00	39
330	503	22	54	1	1	2	1470	332	312	2475	1.13	7.71	18

Table E.10 Reaction results over Fe-MesoMORnew at different temperatures (280–340 ºC, 300 mg catalyst, 100 sccm, 30% CH_4, 10% N_2O, 20–24% H_2O (balance He))

Temp.	r_{CH3OH}	r_{DME}	r_{C2H4}	r_{C2H6}	r_{C3H6}	r_{C3H8}	r_{CO}	r_{CO2}	r_{Coke}	TOF CH_3OH	x_{CH4}	x_{N2O}	S_{CH3OH}
ºC	µmol/g/h									µmol/mmol/h	%		
300	330	6	2	0.4	2	0	343	3	2	1628	0.28	0.77	47
320	796	21	19	0.7	1	0.5	735	20	27	3924	0.67	2.26	48
340	958	27	50	0.8	0.2	2	848	170	171	4723	0.93	5.36	41

Table E.11 Reaction results over Fe-FER at different temperatures (280–340 ºC, 300 mg catalyst, 100 sccm, 30% CH_4, 10% N_2O, 20–24% H_2O (balance He))

Temp.	r_{CH3OH}	r_{DME}	r_{C2H4}	r_{C2H6}	r_{C3H6}	r_{C3H8}	r_{CO}	r_{CO2}	r_{Coke}	TOF CH_3OH	x_{CH4}	x_{N2O}	S_{CH3OH}
ºC	µmol/g/h									µmol/mmol/h	%		
280	35	0.5	0.3	0.2	1	0.06	3	0	22	131	0.03	0.08	53
300	581	12	2	0.5	2	0.01	203	0	2	2187	0.33	0.84	71
320	1219	43	11	1	3	0.51	783	11	7	4590	0.85	2.30	57
340	1648	65	16	3	3	1	956	12	53	6208	1.14	2.78	58